Abdulmaliq Abiodun ALAWODE

Experimental Analysis of Wrinkling of Sandwich Structures

Master Dissertation
European Master Advanced Structural Analysis and Design using Composite Materials

Work developed under the supervision of
Professor Bruno CASTANIÉ
Professor Samuel RIVALLANT

Funded by the European Union

September 2023

DECLARATION

Name: Abdulmaliq Abiodun ALAWODE

Email: alawodeabdulmaliq@gmail.com **Phone number:** +34 605 502 969

Citizen Card Number: B00198980

Title of the Thesis: Experimental Analysis of Wrinkling of Sandwich Structures

Supervisors

Professor Bruno CASTANIÉ

Professor Samuel RIVALLANT

Year of Conclusion: 2023

Master Course in Advanced Structural Analysis and Design using Composite Materials

University of Toulouse III Paul Sabatier, 04/09/2023

Signature:

ACKNOWLEDGEMENTS

I am immensely thankful for the support and funding provided by the Erasmus+ Programme of the European Union. This financial backing has been instrumental in enabling me to pursue my master's study. I wish to express my deep appreciation to the consortium responsible for curating the European Master in Advanced Structural Analysis and Design using Composite Materials [FRP++] program. This unique opportunity to be a part of such an innovative and futuristic initiative has not only broadened my academic horizons but has also empowered me with advanced insights into the realm of structural composites.

I would like to extend my warm gratitude to my esteemed supervisors, Professor Bruno CASTANIÉ and Professor Samuel RIVALLANT. Their unwavering support, invaluable guidance, timely feedback, insightful comments, and invaluable recommendations have been instrumental in shaping the course of this research journey.

I would also like to express my special thanks to Mr. Xavier FOULQUIER, Mr. Jean-Benoît ALIBERT, and Mr. Frederic BONTEMPS, the keen laboratory technicians at Institut Supérieur de l'Aéronautique et de l'Espace (ISAE SUPAERO) and Institut Clément Ader (ICA). Their expertise and assistance have been indispensable in providing technical guidance and facilitating the various procedures involved in sandwich specimen manufacturing, instrumentational measurements, and mechanical testing.

I would also like to extend my gratitude to my FRP++ colleagues, as well as the friends from Nigeria and the news pals I made in Girona and Toulouse, for their unwavering support, camaraderie, and for contributing significantly to the success of this journey. Special shout out to my friend Ayobami Victor Awoleye for recommending and encouraging me to apply for this program.

Lastly, I offer my heartfelt appreciation to Allah for His boundless mercy and blessings throughout this journey. I also want to extend my deepest appreciation to my family - my father, stepmother, and siblings - for their unwavering love, prayers, constant encouragement, and unwavering support that has been the cornerstone of my achievements over the years.

Etude expérimentale du flambement Local des structures sandwiches

RESUME

L’utilisation de structures sandwich s’est répandue dans divers secteurs, notamment dans le domaine de l’aviation légère. L’influence de défaillances localisées imprévues au sein de ces structures peut être gravement préjudiciable, conduisant potentiellement à une défaillance structurelle brutale. Parmi les principaux initiateurs de rupture en compression dans les structures sandwich se trouve le phénomène connu sous le nom de « flambement », une forme de flambage local. Au fil des années, de nombreux modèles analytiques formulés par différents chercheurs ont été adoptés par les ingénieurs industriels. Néanmoins, ces modèles analytiques se sont révélés non conservateurs. De plus, il existe peu d’études expérimentales approfondies sur le wrinkling dans la littérature existante.

Par conséquent, l’objectif principal de cette thèse est de mener une enquête expérimentale axée sur le mode de rupture par wrinkling au sein des structures sandwich. Pour y parvenir, un essai de flexion classique en trois points a été réalisé sur un ensemble de six éprouvettes spécialement conçues, fabriquées selon la technique de drapage manuel. L'objectif fondamental de l'essai était de déterminer la charge à rupture à laquelle se produit le premier flambement par wrinkling en cisaillement. Ce test a été surveillé à l'aide de caméras de corrélation d'images numériques (DIC), de capteurs de déplacement et de capteurs de force. Ces instruments ont été utilisés pour suivre des données essentielles telles que les paramètres de déformation, les déplacements et les forces appliquées. Les données résultantes du test ont ensuite été soumises à deux approches d'estimation des contraintes, et ces estimations ont ensuite été comparées aux modèles analytiques existants.

MOTS-CLES : Flambement; Structures sandwich; Expérience; Échec local; Fabrication; Composite.

Experimental Analysis of Wrinkling of Sandwich Structures

ABSTRACT

The use of sandwich structures has expanded across various sectors, particularly in the realm of light aviation. The influence of unpredicted localized failures within these structures can be severely detrimental, potentially leading to abrupt structural failure. Among the principal initiators of compressive failure in sandwich structures is the phenomenon known as "wrinkling", a form of local buckling. Over the years, numerous analytical models formulated by different researchers have been embraced by industrial engineers. Nevertheless, these analytical models have been proved to be nonconservative. Additionally, there is a scarcity of comprehensive experimental investigations regarding wrinkling in the existing literature.

Therefore, the main objective of this dissertation is to conduct an experimental investigation focused on the wrinkling failure mode within sandwich structures. To achieve this, a classical three-point bending test was conducted on a set of six specially designed specimens, which were manufactured using the hand lay-up technique. The fundamental purpose of the test was to determine the failure load at which the first shear wrinkling occurs. This test was monitored using Digital Image Correlation (DIC) cameras, displacement sensors, and force sensors. These instruments were employed to capture essential data such as strain parameters, displacements, and applied forces. The resulting data from the test were then subjected to two approaches for estimating stress, and these estimations were subsequently compared with existing analytical models.

KEYWORDS: Wrinkling; Sandwich structures; Experiment; Local failure; Manufacturing; Composite.

TABLE OF CONTENTS

LIST OF FIGURES

LIST OF TABLES

List of Abbreviations and Symbols

Abbreviations

EASA	European Union Aviation Safety Agency
VERTEX	Experimental modelling and validation of composite structures under complex loading (French acronym)
LVDT	Linear variable differential transformer
LDS	Laser Displacement Sensor
DIC	Digital Image Correlation
GFRP	Glass Fiber Reinforced Polymer

Symbols

E_f	Elastic modulus of the skin
G_c	Core transverse shear modulus
E_c	Core normal modulus

Notes: The terms skin, face and facesheet are used interchangeably.

THIS PAGE WAS INTENTIONALLY LEFT BLANK

1. CHAPTER 1: INTRODUCTION

1.1. Sandwich structure overview

The advance of fibre composite materials and the aim to diminish both the weight and the cost of structures has given rise to the latest concentration in the usage of sandwich construction for main structures. Strength and weight are essential ingredients to the operational properties of structures, especially in the aeronautics industries [1]. However, the cost per kilogram of composite materials is significant when evaluated [2]. Various design constraints that must satisfy the weight and mechanical performance criteria are considered during the design of composites [3]. Therefore, the aim to achieve desired economical and lightweight structures in the engineering field has led to the wide use of composite sandwich structures [4].

In most literatures, sandwich structures have been described as structures made up of two thin (upper and lower) skins with significantly high mechanical properties, that are separated by the core (either isotropic, anisotropic or orthotropic in nature) a lightweight material with relatively weak mechanical properties [2], [5]–[7]. Summarily, this definition logically describes sandwich as an I-beam which places materials far-off the neutral axis as illustrated in Figure 1.1. The nature of the structure makes the bending stiffness increase with a significant reduction in the total weight of the structure. This eliminates the need for additional stiffeners or stringers to stabilize and control buckling [8]–[10].

The skin, which are commonly carbon, glass fibres or aluminium, due to their great static properties resists the in-plane compressive and tensile loads while the core, most times Nomex honeycomb or foam, stabilizes the structures and takes care of the load transfer mechanism in the form of transverse shear and normal stresses, although lower when compared to the skin, and an adhesive layer between core and skin that transfers the loads between the two. Sandwich structures provide enhanced performances compared to conventional laminates as shown in Table 1.1 and some other material structures. Other exceptional performances include buckling load resistance increments, and impact resistance that are needed in resisting various load forms in structural members.

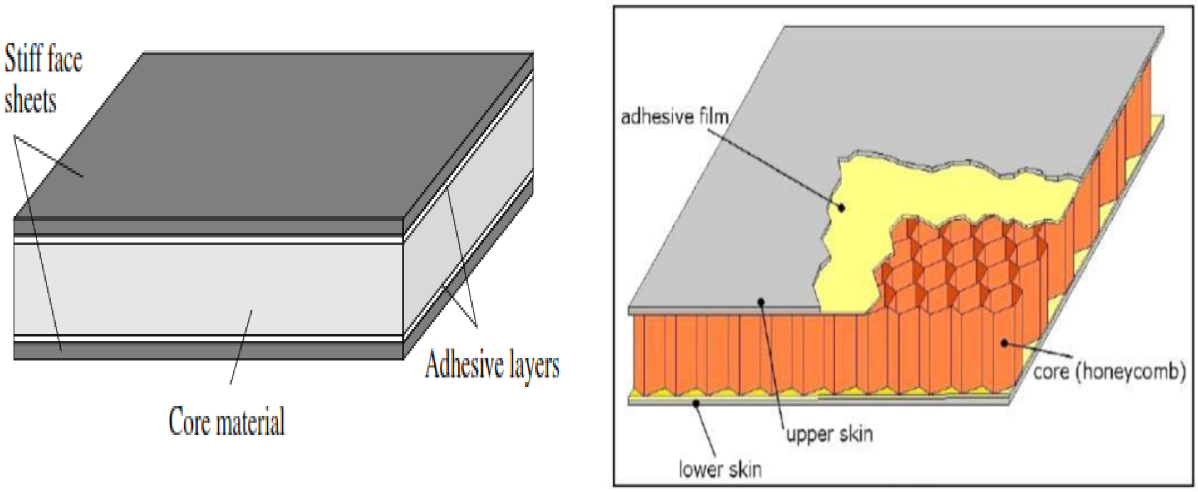

(a) (b)

Figure 1.1: Typical sandwich structure construction with (a) isotropic core [11] (b) orthotopic core [12]

Table 1.1: Sandwich flexural and stiffness comparison with conventional laminates [13]

	Solid material with thickness of *t*	Sandwich with core thickness of *t*	Sandwich with core thickness of 3*t*
Property	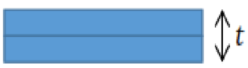	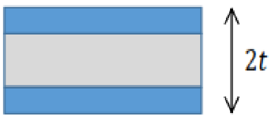	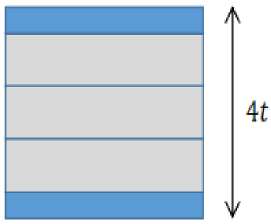
Flexural stiffness	1.0	7.0	37.0
Flexural strength	1.0	3.5	9.2
Weight	1.0	1.03	1.06

The application of sandwich structures can be linked with various fields. They are greatly explored in the aerospace, civil infrastructures, blade for wind power generation, automobile, and shipbuilding industries [14]. They are used largely for light aviation and non-pressurized structures such as the recently certified “Elixir” in Figure 1.2 manufactured by Elixir Aircraft. They are also used in the design of multi-functional structures as in Figure 1.3, as thermal insulators owing to their structural formations [14], complex shape structures such as facades, unique architectural views, and curved structures.

Figure 1.2: The Elixir, 2006 EASA certified two-seater light aircraft [5]

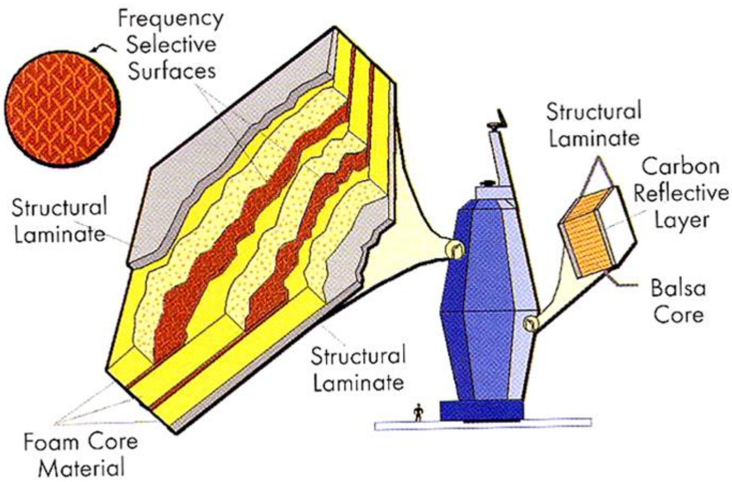

Figure 1.3: Cross-section of sandwich used to enclose the USS Radford mast [15]

1.2. Motivation

Like all structures, sandwich structures are prone to various types of failures, ranging from local to global failures. The behaviour and performance of sandwich structures concerning failure initiation, propagation, and interaction are influenced by multiple factors, including the properties of the constituent materials, the type and state of loading, and the geometrical configuration of the structure [8], [16]. These failure modes are interconnected, meaning that the initiation of one particular mode may lead to the development of other failure modes as the initial failure progresses. Understanding the interplay between these failure modes is crucial for ensuring the structural integrity and reliability of sandwich structures [17], [18].

One of the crucial local failures due to instability of sandwich structure is wrinkling. Wrinkling in sandwich construction refers to the localized face buckling of a compressed sandwich strut or panel, displaying short waves of buckling on the faces in the order of the core thickness [6]. However, wrinkling can also appear when sandwich structures are subjected to shear load as well. By resolution of forces at 45^0, the shear load results in compression and tension loads in opposite directions [19]. In a first approach, wrinkling can be envisioned as the buckling of thin columns (the faces) that are supported by a continuous elastic medium (the core) [8]. Wrinkling poses a significant challenge in sandwich structures, as it can lead to reduced load-carrying capacity and structural stiffness.

Over the years several approaches have been adopted by different researchers to understand wrinkling and consequentially develop simple formulations designers can find resourceful. Although, the core has been identified to play key role to the state-of-the-art determination of wrinkling loads [20]. Other factors such as manufacturing defects [21], initial surface imperfection [3], combined load effect, boundary conditions [22], [23], skin bending-twisting coupling, and the transverse shear flexibility of the skin [8] have pose threat to having good agreement between the approaches.

1.2.1. Analytical perspectives to wrinkling of sandwich

From analytical point of view, Gough et al [24], Hoff and Mautner [10] and Plantema [25] developed wrinkling formulation as in Equation 1.1 based on the theory of elastic foundation. A knockdown factor of 0.5 was proposed by Hoff and Mautner to account for the unknown complicating factors [19]. From another perspective, Allen [26] assumed the stress in the core complies with Airy's 2D stress equation and solved the buckling differential equation to develop the wrinkling stress formulation.

$$\sigma = k\sqrt[3]{E_f E_c G_c} \qquad \textbf{Equation 1.1}$$

Where k = 0.85 and 0.825 for plate and narrow beam for Plantema; 0.91 for Hoff and Mautner and 0.78 for Allen. The core normal modulus, the core transverse shear modulus, and the skin Young's modulus are represented as E_c, G_c, and E_f, respectively.

Yusuff [27] conducted research on the theory of wrinkling in skin separated by a core of finite and sufficient thickness, following a methodology similar to that of Hoff and Mautner. He identified the failure mode in skin with a thin core thickness as resembling the Euler-buckling mode, as the shear stresses in such cases could be disregarded. In his study, Birman [28] examined sandwich panels subjected to biaxial compression, employing the aforementioned models. He observed that the elastic foundation model was applicable when dealing with large wrinkles, where core shear stress was not considered. Additionally, Birman proposed that Hoff's and Plantema's models were more suitable for situations involving small wrinkles.

In a recent study, Su et al. [29] utilized a novel computational model known as the higher-order continuum theory to investigate the influence of foam core cell size on the wrinkling stress of sandwich panels. This advanced model incorporates the couple-stress continuum theory, where they introduced a characteristic length as a unique intrinsic scale parameter in the bending constitutive matrix of the core, allowing for the consideration of cell size effects. The research results demonstrate a promising trend, but further investigations are required to build upon these findings.

Furthermore, Ginot et al. [5] worked on evaluation of the industrial analytical formula; the Winkler formulation, Hoff & Mautner [10], Léotoing et al. [30], Niu & Talreja [31], and Douville & Le Grognec [32], to have a reasonable benchmark. They successfully identified the suitability of each of these models for different standard industrial design scenarios. They stressed the significance of conducting additional experimental work to tackle the nonconservative nature of the current analytical formulations and enhance their accuracy and reliability. This is particularly crucial as there is a scarcity of literature on experimental studies to fill the gap and provide more comprehensive insights.

1.2.2. Experimental perspectives to wrinkling of sandwich

Coming up with an experimental test to assess a highly localized instability failure, such as skin wrinkling, presents a tough and complicated task. To achieve consistent results with analytical formulations, the experimental setup must adhere to the critical assumptions made in those formulations.

In their study, Stiftinger and Rammerstorfer [33] conducted experimental tests on a few anisotropic sandwich specimens, subjecting them to both uniaxial and biaxial compression loading. The research employed a specialized testing facility capable of applying pure bending, pure compression, and combined loading to the sandwich specimens. The study results highlighted that a sudden drop in load during testing was linked to the formation of wrinkling, indicating the presence of nonlinearities in the structure.

In 2002, Daniel et al [17] conducted an experimental investigation on various failure modes in sandwich structures using three different loading configurations: three-point, four-point, and end-loaded cantilever beams. These loading setups imposed bending moments and shear forces on the specimens. The wrinkling load measured for each load condition exhibited variations. For the three-point bending case, a core stiffness reduction factor was adopted to account for the loss of core stiffness. The experiment also revealed that a sharp change in strain parameters corresponded to the formation of wrinkling [33]. The study's conclusion emphasized that wrinkling is largely dependent on the core moduli, as specimens with foam core developed wrinkles, whereas those with honeycomb cores showed no wrinkling.

The experimental study conducted by Tuwair et al. [34] focused on a sandwich panel comprised of GFRP bridge deck panels filled with Polyurethane foam. In contrast to Fagerberg and Zenkert's [3] findings that Allen's mode was more consistent, Tuwair et al.'s results showed that the Hoff and Mautner analytical formula provided the closest prediction to the outcome of the four-point bending tests performed on the specimens to estimate outward skin wrinkling. This observation was attributed to the influence of the core's transverse shear modulus.

Recently, Ginot et al. [6] conducted experiments using the VERTEX testing bench, developed by Castanié [35], to examine wrinkling due to shear and compressive loads in antisymmetric sandwich specimens commonly used in light aviation. The test was conducted in the technological framework of the test pyramid. The results highlighted the dependence of wrinkling on the mechanical properties and geometrical configuration of the sandwich structure [18]. They observed a linear relationship between compressive strain and load increase before wrinkling occurred. Furthermore, the study found that honeycomb materials exhibited better resistance to wrinkling compared to foam core materials. The researchers suggested the need for more experiments at this scale to further enhance the understanding of wrinkling behaviour in such sandwich structures used in light aviation.

1.3. Research aim and objectives

As indicated in section 1.2 above, it is evident that there are limited experimental studies on wrinkling of sandwich structures available in the literature. Moreover, the existing experimental works show a lack of correlation with the analytical formulations. This highlights the critical need for further research and more comprehensive experimental investigations on wrinkling behaviour in sandwich structures.

Therefore, the aim or goal of this experimental research work is to analyse the behaviour of sandwich structures under combined shear and bending loads, with a specific focus on understanding the onset and propagation of wrinkles. The study aims to track the failure load and wavelength of wrinkling to gain insights into the mechanisms and characteristics of this phenomenon. By conducting systematic experimental tests, this research aims to bridge the gap between analytical predictions and real-world behaviour, providing valuable data to enhance the understanding and design of sandwich structures.

The objective can then be summarised therein as follows:

1. To test specialized sandwich specimens to fail by compression or shear wrinkling using a simple classical three-point bending test.
2. To study wrinkling failure scenario and mechanisms using laser displacement sensor, Linear variable differential transformer (LVDT) displacement sensors, force sensor and Digital Image Correlation (DIC) cameras.
3. To analysis the wrinkling failure load, wavelength development, the skin failure strain parameters and the wrinkling stress.

1.4. Structure of the dissertation

Chapter 1 serves as an introduction to the study, encompassing an explanation of the research's motivation, aim, and objectives. Chapter 2 delves into the literature review, providing a comprehensive exploration of the existing body of knowledge on the subject. Chapter 3 outlines the test methodologies adopted throughout the course of the study, detailing the experimental procedures and setups used to investigate the behaviour of sandwich structures under combined shear and bending loads. In Chapter 4, the results of the experimental tests are elaborated upon, along with a thorough discussion of the analysis of the obtained data. Finally, Chapter 5 draws together the conclusions derived from the research and valuable recommendations for future research directions, paving the way for further advancements in the field.

THIS PAGE WAS INTENTIONALLY LEFT BLANK

2. CHAPTER 2. LITERATURE REVIEW

In this section, a comprehensive discussion is presented, focussing on various aspects of sandwich structures related to wrinkling. It gives an overview of sandwich structures, the materials constituents are explored, various manufacturing techniques employed for sandwich structures construction, failure modes attributed to sandwich structures, and classical and novel approaches available in estimating wrinkling failure in sandwich structures.

2.1. Sandwich structures

Several definitions have been proposed to illustrate what and how sandwich structure looks like. ASTM [4] defines sandwich structure as a "special form of a laminated composite comprising of a combination of different materials that are bonded to each other so as to utilise the properties of each separate component to the structural advantage of the whole assembly". Hoff and Mautner in 1944 [10] suggested a definition for sandwich structures as thus - "The characteristics feature of the sandwich construction is the use of a multilayer skin consisting of one or more high-strength outer layers (faces) and one or more low-density inner layers (core)". In most literatures, sandwich structures have been described as structures made up of two thin (upper and lower) skin with significantly high mechanical properties, that are separated by a lightweight material with relatively weak mechanical properties [2], [5]–[7]. Summarily, these definitions logically describe sandwich as an I-beam which places materials far-off the neutral axis or from the centre of bending.

Section 1.1 highlights numerous applications of sandwich structures across various industries. Although due to long time taking certification process, they are limited in use where material standardization is mandatory. However, the presence of multiple constituents has posed a significant challenge to the industrial design of such structures. This complexity makes the design process rigorous and demanding to execute effectively. One of the strategies employed in sandwich structures especially in light aviation to optimize their performances and functions [12] is to tailor their form to suit their intended applications [36]. As a result, two main types of sandwich structures have been developed: conventional symmetric and asymmetric sandwich structures [12].

Symmetric sandwich structures are the popular/conventional sandwich structures in which bottom top and bottom faces are exactly the same as in Figure 1.1. Due to the similarity in both faces, the stiffness of the skin is the same [15]. As a result of their excellent bending performance, they are mostly used when equal or approximately same loads are applied to both faces [37].

Asymmetric sandwich structures, as depicted in Figure 2.1, are specially designed with unidentical bottom and top skins thicknesses. The exterior skin, also referred to as the "Working skin," serves the purpose of restraining membrane stresses or providing impact resistance, depending on the specific application. On the other hand, the inner skin, known as the "Stabilizing skin," works in conjunction with the core to offer buckling resistance and enhance the overall structural stability [12], [37]. Several works have conducted to understand the behaviour of this special structure [6], [35], [37]–[39]

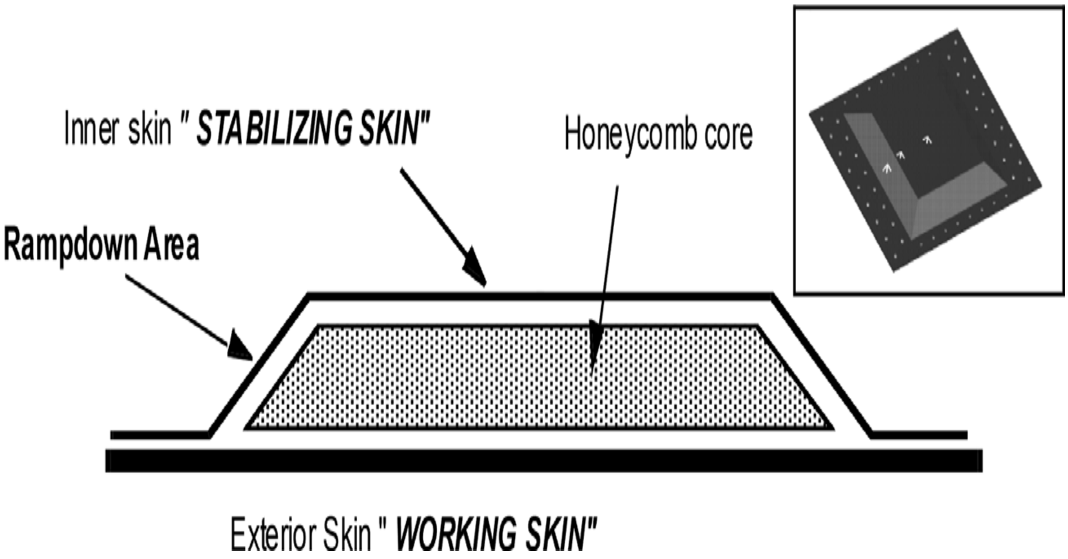

Figure 2.1: Asymmetric sandwich structures [12]

2.2. Material constituents of sandwich structures

For sandwich structures, the skin or facesheet or face needs to be stiff and strong to handle in-plane stresses effectively. The core must possess sufficient stiffness and strength to withstand shear forces and provide necessary lateral stability. Meanwhile, the adhesive layer plays a crucial role in bonding the core with the skin, ensuring proper load transfer between the constituents. Hence, it is of utmost importance for engineers to meticulously choose the right materials for each constituent to achieve the desired performance and functionality of the sandwich structure. Proper material selection ensures that the structure can efficiently bear the loads and stresses it is subjected to during its application.

2.2.1. The skin material

The skins are made up of composite laminates or isotropic metals. For the case of composite laminates, they comprise of certain oriented fibres stacked in the designed orientation as shown in Figure 2.2 to give the desired mechanical properties. The fibres are bonded together and protected by the matrices. For simplicity, symmetric and balanced composite laminates are mostly employed in sandwich structures. The most commonly fibres are carbon, glass, and aramid (Kevlar). Table 2.1 shows properties of the major fibres in use. These values are proposition as the actual fibre mechanical properties are to be determined using appropriate testing methods. Carbon fibres are widely used for aeronautical applications due to their better mechanical properties although they are quite expensive. Steel, aluminium, and titanium alloy are isotropic metal mostly adopted depending on application.

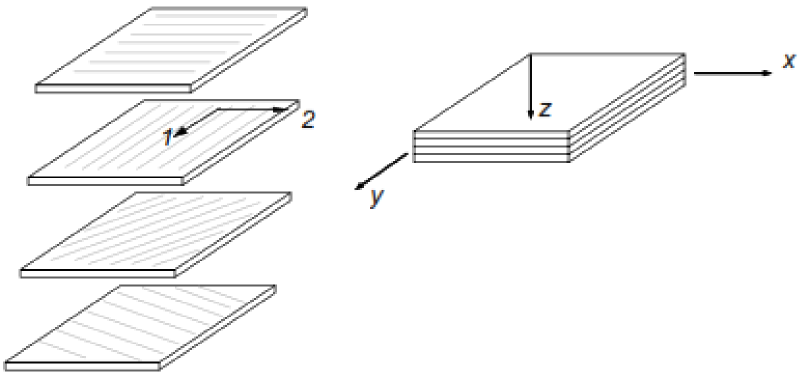

Figure 2.2: Composite laminate stacking structure [4]

Table 2.1: Mechanical properties of major composite fibers used as skin material [2]

Type of fibre	Density (Mg/m^3)	Tensile modulus (E) (GPa)	Tensile strength (σ) (MPa)	Specific modulus (E/ρ) (GPa m^3/Mg)	Specific strength (σ/ρ) (MPa m^3/Mg)	Melting point (°C)	Relative cost
E-glass	2.54	70	3450	27.6	1385	≥1540	Low
S-glass	2.50	86	4500	34.4	1800	≥1540	Moderate
HM-carbon (high modulus)	1.90	400	1800	210.5	947	≥3500	High
HS-carbon (high strength)	1.70	240	2600	141.2	1529	≥3500	High
Boron	2.6	400	3500	153.8	1346	2300	High
Aramid (Kevlar® 29)	1.45	80	2800	55.2	1931	500	Moderate
Aramid (Kevlar® 49)	1.45	130	2800	89.7	1931	500	Moderate

2.2.2. The core material

The core is an integral component of sandwich structures, responsible for transverse shear and compressive loads, lateral stability, and crash resistance. These critical roles make the out-of-plane mechanical properties of the core particularly significant compared to other properties. Various types of core materials utilized in sandwich structures are illustrated in the Figure 2.3. Other forms include X-cor or K-cor, in this case there is no need for adhesive application [19]. Foam such as Polymethacrylimide (PMI) as in Table 2.2 used in this study are closed cells which make them isotropic and water resistant while honeycombs are anisotropic.

The core density has significant contributions to the strength and stiffness of the sandwich structure; also increasing the core density results in increase in the overall weight of the structure. In order to strike a balance between mechanical performance and weight, core of different densities is strategically bonded together to suit the anticipated application [6]. Recently, research is being intensified on the contributions of soft-core materials [40] to wrinkling failure in sandwich structures as in Figure 2.4.

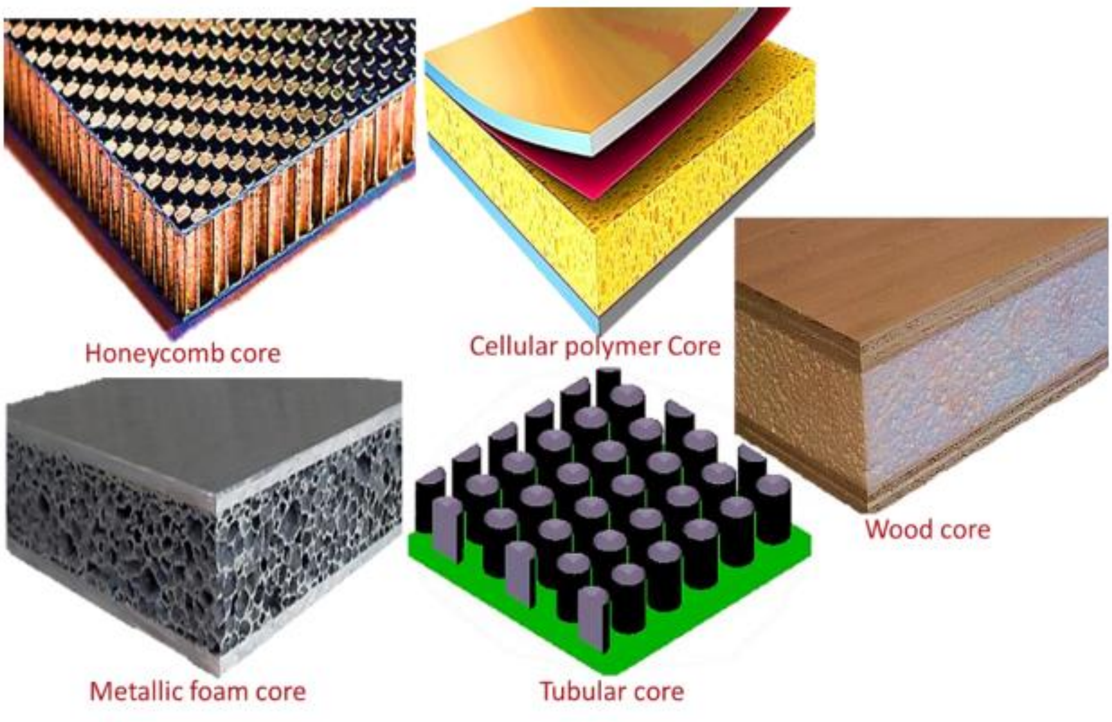

Figure 2.3 Different core materials used in sandwich structures [7]

Table 2.2: Properties of Rohacell PMI foams [41]

Properties	Unit	ROHACELL® 51 WF	ROHACELL® 71 WF	ROHACELL® 110 WF	ROHACELL® 200 WF	Standard
Density	kg/m³	52	75	110	205	ISO 845
	lbs./cu.ft.	3,25	4,68	6,87	12,81	ASTM D 1622
Compressive strength	MPa	0,8	1,7	3,6	9,0	ISO 844
	psi	116	246	522	1,305	ASTM D 1621
Tensile strength	MPa	1,6	2,2	3,7	6,8	ISO 527-2
	psi	232	319	536	986	ASTM D 638
Shear strength	MPa	0,8	1,3	2,4	5,0	DIN 53294
	psi	116	188	348	725	ASTM C 273
Elastic modulus	MPa	75	105	180	350	ISO 527-2
	psi	10,875	15,225	26,100	50,750	ASTM D 638
Shear modulus	MPa	24	42	70	150	DIN 53294
	psi	3,480	6,090	10,170	21,750	ASTM C 273
Elongation at break	%	3,0	3,0	3,0	3,5	ISO 527-2
						ASTM D 638
Heat distortion temperature	°C	205	205	205	205	DIN 53424
	°F	401	392	392	392	

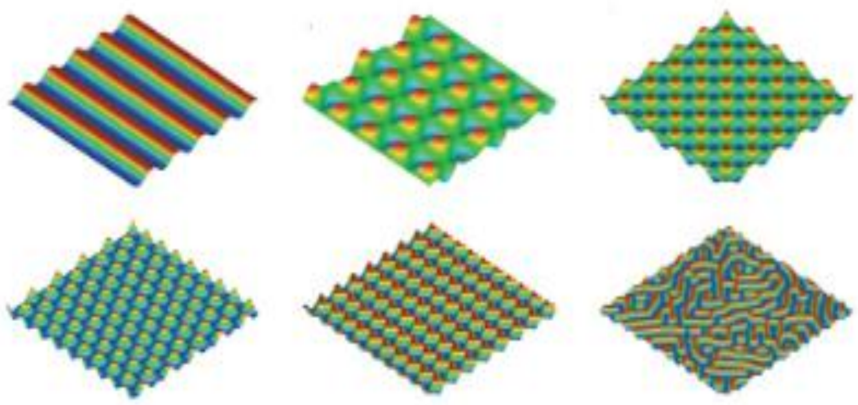

Figure 2.4: Wrinkling in soft-core materials [40]

2.2.3. The sandwich adhesive material

Adhesives in sandwich act as binder for either skin-core joining or core-core joining [6]. They help in ensuring proper load transfer between parts. In 2002 Mazumdar [42] classified adhesives used for composite sandwiches into three categories based on their mixing techniques. They are two-component, no-mix adhesives such as Acrylic and Urethane Methacrylate Ester adhesives; two-component with mix adhesives such as Epoxy and Polyurethane adhesives and the one-component, no-mix adhesives such as epoxies, polyurethanes, cyanoacrylates, hot-melt, and solvent or water-based adhesives.

Sena-Cruz and Renart [43] also mentioned pastes and prefabricated films as types of adhesives. The former allows bonding of variable thickness and it is highly recommended for foam core sandwich and detrimental to honeycomb sandwich structures. The latter is used widely used in aerospace/aircraft industry for secondary parts. Films are prepared like pre-pregs that allow uniform thickness bond-line but poor gap fillers which makes it suitable for honeycomb core sandwich structures.

2.3. Manufacturing techniques in sandwich structures

The suitable manufacturing technique for a sandwich structure is determined by considering factors such as the type of skin and core materials to be used, the structure's shape and geometrical configuration, and the performance level requirements of the final structure. These considerations collectively guide the decision-making process for selecting the most appropriate manufacturing method [44].

Castanié et al. [12] identified co-curing or single shot, co-bonding and secondary or multiphase process as illustrated in Figure 2.5 as the three main sandwich manufacturing methods employed in the aeronautical industry to certify top final sandwich quality. Co-curing or single shot refer to the method in which the skin and the core are both cured together. In order to reduce cost of materials, it is advisable to use single-shot manufacturing where mass production is supposed [44]. This process is achieved traditional by wet hand-layup or recently using vacuum-assisted resin infusion (VARI) with autoclave curing process. VARI method gives better quality, lessens resin outlay and decrease in volatile discharge than wet hand-layup. Both causes absorption of resin by the core, foam, which invariably increases the weight of the structure. The other two methods require the use of adhesive bonds discussed in section 2.2.3.

Additionally, Kausar et al. [7] conducted extensive research work on the successful cutting-edge sandwich manufacturing strategies utilized in the construction of sandwich structures. He explained manual process, simply known as hand layup, Prepreg methods, injection processes, compression-based process, pultrusion also known as continuous process, and 3D printing. The key areas of application, influence on structural mechanical behaviour, factor affecting their performance and peculiar challenges and deficiencies of each method were revealed. The work also extends to other manufacturing phases such as machining, drilling, cutting or milling operations. These aspects are not addressed in this review as they fall outside the scope of the study.

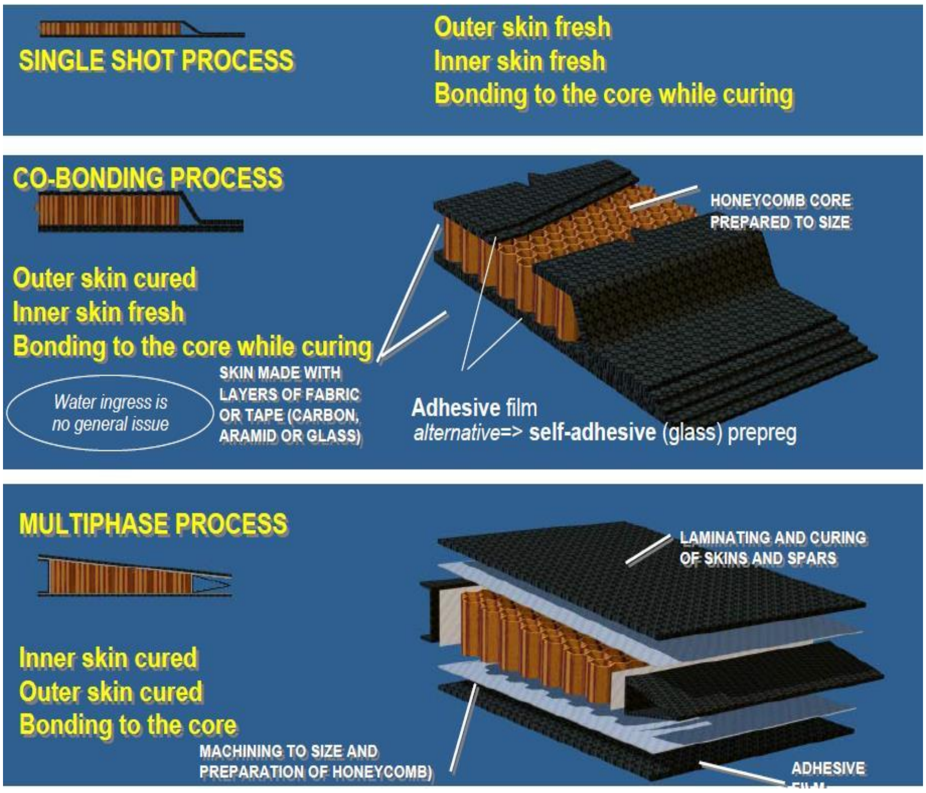

Figure 2.5: Schematic of sandwich manufacturing techniques [45]

Kryzak et al [14] concluded that manufacturing techniques with even and more intense pressure result in better mechanical properties. However, this pressure is should be limited to avoid core crushing. Also, unlike hand lay-up and pressing methods, manufacturing of composites using an autoclave produces specimens or structures with smooth, homogenous surfaces, and is deficient in structural discontinuity. Although autoclave appears to produce structures with better performance, the pressing method can be seen as a relatively close and cheap method that is being used in the aeronautics sector.

Scientists of recent are switching to the usage of additive manufacturing or 3D printing in sandwich manufacturing. Several techniques such as Fused deposition modelling (FDM), fused filament fabrication (FFF), direct ink writing (DIW), stereolithography (SLA) [46], material extrusion (MEX) [47] and Digital light processing (DLP) [48]. Additive manufacturing of sandwich structures is the modern method of sandwich construction that gives no limit to the geometrical configuration that can realized with sandwich. It is also known as a technique that saves time, materials, has insignificant impact on the environment and relatively simple to accomplish. However, Four-dimensional (4D) printing technique is another modern technique used in the production of sandwich structures with four-dimensions. It gives more robustness in terms of time and degree of freedom compered to 3D printing. Research [7] proves that recovery ratio and shape fixity of 4D printing are 99% and 98% respectively.

2.4. Failure modes in sandwich structures

Despite sandwich structures exhibit remarkable usefulness and find wide range of applications, their global effectiveness can be remarkably compromised when specific failure modes come into play. This is due to the inherent complexity arising from the diverse constituents present within the sandwich, as discussed in section 2.2. The interaction of these components gives rise to a range of possibilities for failure. Hence, from design point of view, composite designers are to ensure failure effects are within tolerance at the loading service conditions as in Figure 2.6.

To ensure optimal performance in practical applications, it is imperative to exercise caution by considering the significant factors that contribute to the failure of sandwich structures. These factors encompass the manufacturing techniques adopted, the design philosophy (maybe post buckling is allowed), geometrical sizing, the nature of applied loads, and the suitability of the mechanical properties of the materials used [16]. To avert the possibilities of failure it must be confirmed that the face and core have necessary properties, and in the same vein the skin-to-core adhesive bond is capable of transferring stresses between them. Otherwise, the overall stiffness and strength of sandwich structure will decrease below the anticipated magnitude.

Based on the submission above sandwich beams subjected to combined bending and shear loads can undergo diverse failure modes. These include wrinkling, face tension and compression, core shear failure, skin-core debonding, localized indentation, and global buckling. The recognition of these potential failure scenarios emphasizes the importance of a thorough comprehension of these aspects when dealing with the design and evaluation of sandwich structures. In this section wrinkling failure will be discussed in-depth while others will be briefly elaborated.

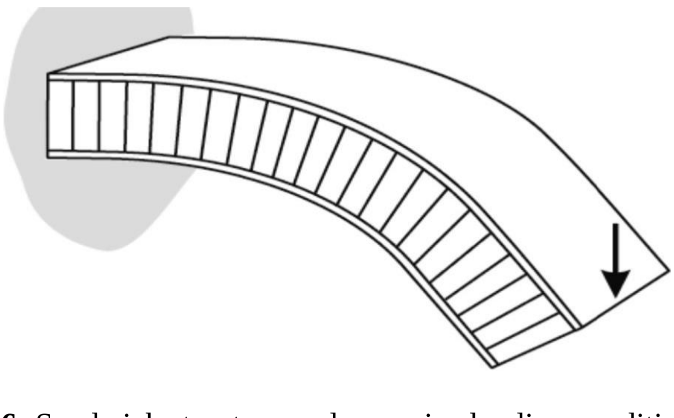

Figure 2.6: Sandwich structure under service loading condition [2]

2.4.1. Sandwich wrinkling

Wrinkling is a local buckling phenomenon where the skin of the sandwich structure buckles generating wrinkles as illustrated in Figure 2.7 over a characteristics half-wavelength, which is unconnected to the overall length or width of the panel [19]. This failure scenario is unrestricted to the direct or indirect compressive loading of the skin alone, but as well occurs under applied shear and combined or multiaxial loading cases which make its study more relevant to wide fields. However, in the case of sandwiches with corrugated or honeycomb cores, the core does not provide continuous support. As a result, the buckling wavelength must match the distance between supports, such as the cell size of the honeycomb [4], [18], [49].

Furthermore, the modes of wrinkling present are three namely; one-sided wrinkling or the “Rigid base”, antisymmetric wrinkling (in phase) or the “Snake” mode, and symmetric wrinkling (out of phase) or “Hourglass” as illustrated in Figure 2.8. The mode depends on the elasticity and thickness of the core whether isotropic or anisotropic. Provided that the core thickness is enough, antisymmetric wrinkling does not occur [26], [50].

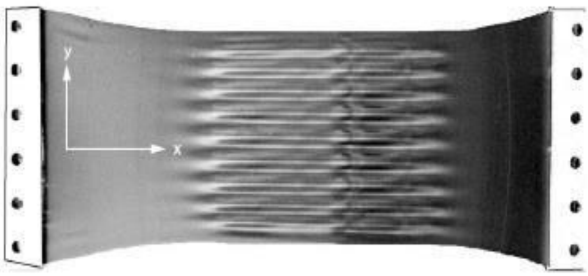

Figure 2.7: Typical wrinkling form [51]

Figure 2.8: Wrinkling failure modes [3]

Some of the notable factors that trigger wrinkling failure are manufacturing technique adopted, as in section 2.3, as some method have impact on the structural integrity, presence of initial surface imperfection [3], mechanical properties of the core [20], the type of boundary condition the sandwich is subjected to [23], and general load application system [8]. These factors also contribute to the difference between experimental and analytical because they are in fact strenuous to control.

The general assumption used in wrinkling assumes the skin and the core as isotropic, elastic materials in the form of cylindrical or plate bending under compressive load. Since wrinkling is a form of buckling, it can be said to be governed by the 4th-order bending theory differential in Equation 2.1.

$$D_s \frac{d^4 w_s}{dx^4} + P_s \frac{d^2 w_s}{dx^2} - b\sigma_z + \frac{dm}{dx} = 0 \qquad \textbf{Equation 2.1}$$

Where D_s is the bending rigidity of the face sheet alone, P_s is the axial compressive load per unit width acting on the facesheet, σ_z is the normal support pressure between the core (elastic foundation) and the facesheet, and m is the acting bending moment not considered most times due to the tinny depth of the skin [26].

In the industry engineers design aeronautical parts using the global finite elements model (GFEM) which fails to capture local failures like wrinkling. This demands for highly refined meshes to accurately identify local failures, a process that requires a considerable amount of time and the utilization of advanced processors [5]. It is therefore necessary and economical to implement conservative analytical methods to quantify this phenomenon. The first approach to solving skin wrinkling was proposed in 1940 by Gough et al. [24] using the concept called Winkler's elastic foundation. Other analytical and experimental works are discussed in section 1.2.1 and section 1.2.2 respectively. Table 2.3 gives summary of some of the analytical formulae for wrinkling stress and half-wavelength available in the literature. The mathematical proves for these can be found in references [2], [8], [10], [15], [19], [24], [27], [33].

Aside the classical method, higher order panel theory (HSPAT) and an its improved form, extended high-order sandwich panel theory (EHSPAT), are explicitly elucidated by Carlsson and Kardomateas [15]. Su et al. [29] in their work adopted the concept of higher-order couple-stress continuum theory as in Figure 2.9 to investigate wrinkling by altering the core bending stiffness matrix with an initialized characteristic length, l_c to come up with a formulation as in Equation 2.2. The derivation was compared with the classical formula of Hoff and Mautner [10], Allen [26], Heath, Carlsson and Kardomateas [15], and experimental works. The result showed an improved level of conservativeness.

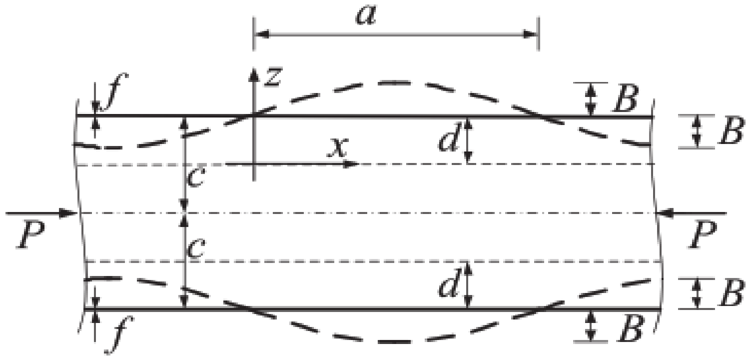

Figure 2.9: Wrinkling model for sandwich panel with couple-stress continuum core [29].

$$\sigma^f = \frac{G_c d}{3f} + \frac{E_c a^2}{\pi^2 f d} + \left(\frac{\pi^2 d}{3a^2 f} + \frac{1}{fd}\right) G_c l_c^2 + \frac{E_f \pi^2 f^2}{12a^2} \qquad \textbf{Equation 2.2}$$

Table 2.3: Summary of wrinkling analytical formulae

Reference [Classical]	**Wrinkling stress, σ_{wr} [MPa]**	**Half-wavelength, *a* [mm]**
Hoff and Mautner [10]	$0.91\sqrt[3]{E_f E_c G_c}$ With knockdown factor; $0.5\sqrt[3]{E_f E_c G_c}$	$1.648\ t_f \sqrt[6]{\frac{E_f^2}{E_c G_c}}$
Plantema [25]	$0.85\sqrt[3]{E_f E_c G_c}$	$1.9\ t_f \sqrt[6]{\frac{E_f^2}{E_c G_c}}$
Allen [26]	$\frac{3}{\sqrt[3]{12(3-v_c)^2(1+v_c)^2}} \sqrt[3]{E_f E_c^2}$	$2.09\ t_f \sqrt[3]{\frac{E_f}{E_c}}$
Heath [16]	$\left[\frac{2}{3}\frac{t_f}{t_c}\frac{E_c E_f}{(1-v_c^2)}\right]^{\frac{1}{2}}$	-
Gough et al. [24]	$0.79\sqrt[3]{E_f E_c G_c}$	-
Yusuff [27]	$0.961\sqrt[3]{E_f E_c G_c}$	$1.307\ t_f \sqrt[6]{\frac{E_f^2}{E_c G_c}}$

where the core normal modulus, the core transverse shear modulus, the skin Young's modulus, skin thickness, Poisson's ratio of the core and wrinkling stress are represented as E_c, G_c, E_f, t_f, v_c and σ^f respectively.

The study of wrinkling using computational approach have been explored by many researchers. In 2007 Ji and Waas [52] presented a computational two-dimensional linear elastic isotropic continua mechanical model using the classical elasticity to capture global and local buckling of sandwich beams. The method was also implemented for wrinkling and edge buckling in orthotopic beams subjected to uniaxial compressive loading [53]. The results showed that anti-symmetrical wrinkling mode occurs at lower stress compare to symmetric when the beam is short. Their predictions were supported by finite element analysis.

In addition, the linear stability, Sub-laminate Generalized Unified Formulation (SGUF) and Ritz approach, was implemented by Vesconini et al [54] to address global buckling and winkling behaviour of sandwich plates when the skin is anisotropic. It is an upgraded work to Carrera Unified Formulation (C.U.F) [55]. This work is convenient and efficient for cases where the cost and time of running finite element simulations becomes too demanding due to mesh refinement. It is important to consider the multiaxial loading conditions, effect of skin anisotropy and the precise boundary conditions. They concluded that sandwich structures with quasi-isotropic cores require high-order core models for antisymmetric wrinkling cases. On the other hand, low-core models accurately predict symmetric wrinkling scenarios since the shear term can be neglected. Although, the method is not efficient for multiaxial loading,

In conclusion, Zenkert [4] presented additional criteria and guidelines to some key design parameters that contribute to addressing and avoiding the potential occurrence of wrinkling failure in sandwich structures during their operational service. The work of Hadi and Mattew [56] reviewed that the presence of adhesive layer increases the result accuracy and brings experimental results close to analytical propositions.

2.4.2. Tensile or compressive skin failure

The skins may fail when subjected to tension and compression uniaxial stresses. The compressive failure is mostly common in composite skin due to their higher resistance to tensile forces than compressive forces. Since the out-of-plane failure is assumed to be harnessed by the core, the out-of-plane properties are neglected in this case. This is apparent in pure bending loading conditions. For metallic skin emergence of plastic deformation that depicts failure (depending on the design philosophy) can be captured using the Von Mises or Tresca criterion. The maximum strain or stress failure criteria is suitable for both cases [9].

2.4.3. Core shear failure

The primary assignment of the core is to cater for the shear loading; consequently, it is anticipated to carry almost all the whole transverse forces. Majorly in isotropic cores such as foam shear stresses cause shear cracks that appear inclined at 45^o to the x-direction when the shear carrying capacity of the core has been exceeded. On the other hand, the failure analytical method depends on the length of the beam. For short beams maximum stress failure criterion works reliably while for long beams where the core is subjected to biaxial state of stress failure analysis such as Tsai-Wu failure criterion is apt [16].

2.4.4. Skin-core debonding

Skin-core debonding can lead to catastrophic failure since the essential structural interaction required for the structure parts to withstand external loads is compromised. The skin-core debonding can arise either during the manufacturing phase, as a consequence of machining and fabrication procedures involving the sandwich, or due to the application of external loads [4]. Debonding can result to damages such as buckling under in-plane compression, loss of stiffness, and reduced impact resistance. When designing a sandwich structure, engineers meticulously consider the mechanical properties of the matrix or adhesive layer. This is essential to guarantee that the fracture loads are within acceptable limits, while also ensuring that the structure remains within its defined resistance and tolerance thresholds in the presence of debonding [16].

2.4.5. Other failure modes

Generally, failure modes in sandwich are mainly controlled by the core. Failures such as sandwich crimping [19], global buckling [6], [30], [52], [54], and sandwich indentation [13], [16] can be found as summarized in Table 2.4. A significant challenge in designing sandwich structures lies in the complexity of accounting for all potential failure modes in the post-buckling phase. Consequently, failures like global buckling are often deemed to coincide with the ultimate failure, as it becomes intricate to anticipate and counteract all possible failure scenarios [19].

Table 2.4 Summary of possible failure modes in sandwich structure [2]

Facing failure 	Insufficient panel thickness, facing thickness or facing strength may result in failure occurring in either the compression or tensile face.
Transverse shear failure 	Transverse shear failure is caused when either the shear strength of the core or panel thickness is insufficient.
Local crushing of core 	Local crushing of core is caused when compressive strength of the core material is too low.
Panel buckling 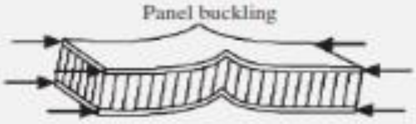	Panel (or general) bucking is caused when either the panel thickness or core shear stiffness is too low.
Shear crimping 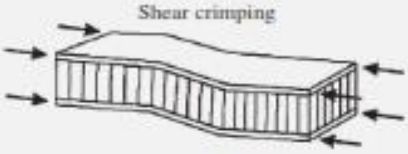	Shear crimping, which can occur as a consequence of general buckling, is caused when either the shear modulus of the core material or the shear strength of the adhesive is low.
Face wrinkling 	Core compression failure (buckling inwards) or adhesive bond failure (buckling outwards) may occur depending on the relative strength of the core in compression and adhesive in flatwise tension.
Intracell buckling (dimpling) 	Intracell buckling (applicable to cellular cores only) occurs where the skins or faces are very thin and the cell size is large. This effect may cause failure by propagating across adjacent cells, thereby inducing face wrinkling.

3. CHAPTER 3. RESEARCH METHODOLOGY

In this section the materials and test methodologies employed throughout the course of the dissertation and details of the experimental procedures and setups used to accomplish the objectives of this research are discussed.

3.1. Sandwich samples description and materials

The specimens used for this research are similar to the standard samples used for courses for industrial engineers at ISAE SUPAERO which makes it original. The general dimensions of the geometry are 50mm by 50 by 500 mm [W x H x L] as shown in Figure 3.2. The partitions demarcate the positions of the woods installed to prevent the sandwich foam core from crushing due to load concentration when subjected to three-point bending. The skin comprises of the combination of EC68 bi-directional [fabrics] and unidirectional [UD] glass fibre-epoxy plies and the core is made up of isotropic PMI Rohacell 51 WF foam core. Mechanical properties of the skins and the cores are as shown in Table 3.1 while the stacking sequence is as illustrated in Figure 3.3.

From earlier studies [57], the geometry and the stacking sequence have been carefully studied and selected to ensure localized failure of the specimen at the expected face, shear face. The top and bottom laminates comprise of five unidirectional plies stacked at 0^o with two extra 45^o bidirectional plies at the bottom and one extra 45^o bidirectional ply at the top. The two sides are stacked with one 45^o bidirectional plies. Better put, the entire beam was enveloped using the 45^o fabric, thereby establishing continuity at the edges, the configuration is illustrated in Figure 3.3. In other words, the stacking is: top $[O_5/\pm45]$, bottom $[O_5/\pm45_2]$ and the two sides $[\pm45]$. With these configurations, the six specimens are envisaged to develop wrinkling due to shear forces induced from the three-point bending test.

3.2. Manufacturing of sandwich samples

The specimens were prepared through the utilization of hand lay-up techniques, which represent the most used method in composite manufacturing. First of all, non-crimp dry preform E-glass fibres were precisely cut to the appropriate dimensions using cutting tools. In addition, the PMI ROHACELL 51 WF foam core was cautiously cut in accordance with the specified geometry, ensuring utmost care to prevent any initial dents in the foam that could lead to failure. The wooden components were affixed to the cores using epoxy adhesive. For the resin, a combination of Araldite LY 5052, a low viscosity epoxy resin, and its corresponding hardener, Aradur 5052 – a mixture of polyamines, both manufactured by HUNTSMAN, was employed. These components, epoxy and hardener, were thoroughly mixed at room temperature, maintaining a ratio of 50:19 by weight. Furthermore, to prevent the final specimens from adhering to the mould surface, a release antiadhesive agent was applied to the mould surface.

Table 3.1: Mechanical properties of the sandwich materials

A. Skin material	E_l **[MPa]**	E_t **[MPa]**	G_{lt} **[MPa]**	v_{lt}	**Thickness,** t_s **[mm]**
UD	38000	10000	4000	0.250	0.30
Bidirectional [Fabrics]	23000	23000	2900	0.098	0.16

B. Core material	**E [MPa]**	**G [MPa]**	**Density** $[kg/m^3]$	**Shear Strength** [MPa]	**Thickness,** t_c **[mm]**
Rohacell 51 WF	75	24	52	0.8	50

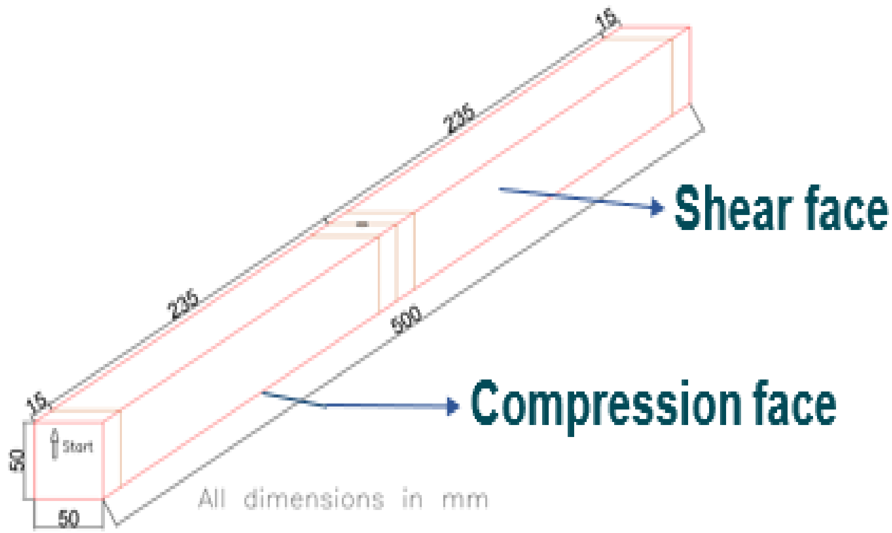

(a)

Figure 3.1: Typical specimen overall geometrical scheme.

(b)

Figure 3.2: Typical specimen overall geometrical scheme.

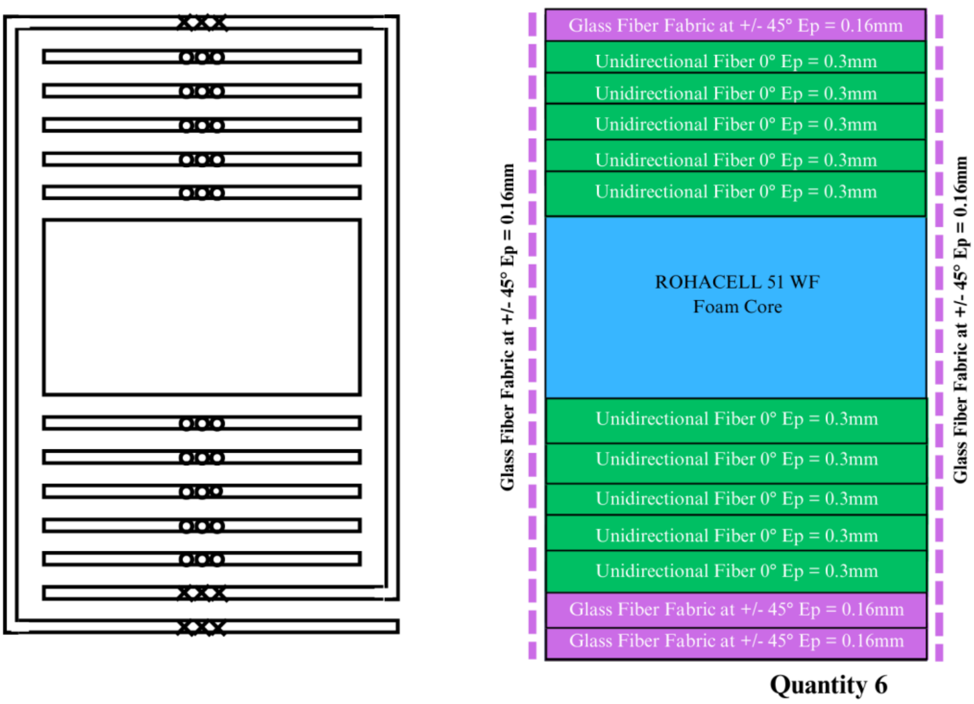

Figure 3.3: Specimen stacking sequence.

A single-shot sandwich specimens was used in this research, that is, the fibres and the core were cured together at once [12]. The top fibres were placed in the male mould and the resin was impregnated into the fibres expelling air bubbles using the brush [14]. The fibres were allowed for few minutes to properly soak-in the resin before placing the core part. Moreover, the bottom plies were then placed and impregnated with resin. Note that the fabric oriented at

$\pm 45^o$, was applied as a complete wrap around the core to achieve the stacking arrangement described in Figure 3.3. Having completed that, the female mould was clamped with the male mould using bolts and G-clamps allowing out-flow of excess resin. The specimens were cleaned and then transferred into an autoclave system for a 24-hour curing process at $42^o C$ to achieve properly curing of the specimen.

The polymerization process of the resin and the spring-back effect were not studied in this research. Furthermore, the specimens were withdrawn from the autoclave, demoulded and any remaining sticky resin was carefully removed through grinding, with scrupulous attention to prevent any damage or removal of the fibres. The comprehensive overview of the entire manufacturing process is as illustrated in Figure 3.4.

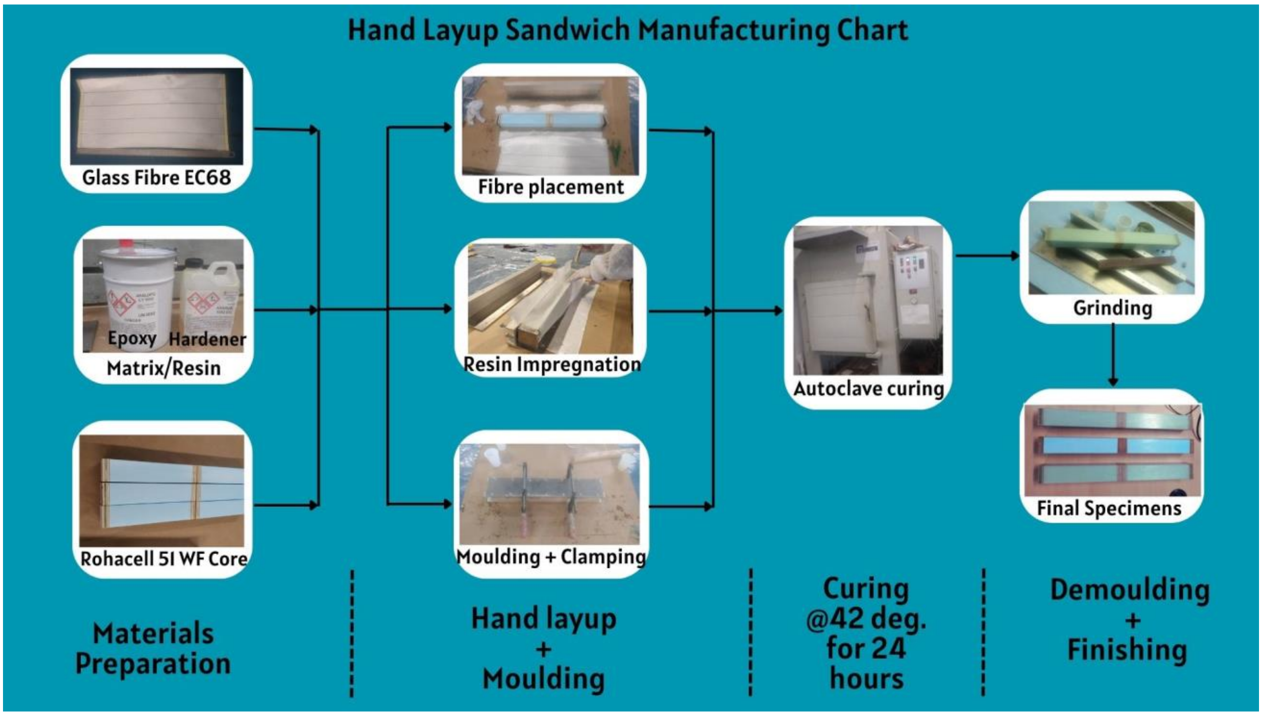

Figure 3.4: Sandwich sample manufacturing technique chart.

3.3. Initial out-of-plane deformation detection by laser displacement sensor

The effect of surface imperfection on the behaviour of sandwich structures is indeed significant especially when it is subject to compressive stresses [3]. This phenomenon results in the reduction of the mechanical properties; hence materials behave less than expectations. Also, the anomalous experienced when comparing analytical results in wrinkling failure estimation with its experimental studies has been established and linked with the initial imperfection on the skin of a sandwich structure [6]. Therefore, having a glimpse of the facial status of the skin is paramount to understanding the sequence of wrinkling, and it can be described as a viable path in achieving a close correlation between experimental results and analytical formulations. Hence, the main objective of this part is to capture the initial out-of-plane deformation present on the shear faces of the sandwich specimens prepared before subsequent classical wrinkling test. Also, a laser displacement sensor (LDS) will provide valuable insights into the out-of-plane condition of the specimens and aid in predicting the location on the sandwich specimen where the first wave could be observed. To achieve this, an LDS was employed.

This test was carried out on sandwich samples tagged A1, A2, and A3 only. Firstly, different points of interest were marked with the aid of a permanent marker on the two shear faces similar to mesh with dimensions 20mm by 10mm while a 5mm offset was maintained to cater for edge defect due to grinding as shown in Figure 3.5. These points were tracked using a Keyence LK-G512 24-volt laser sensor head with Keyence LK-GD500 distance reader, bench vise, and a semi-automated milling machine flat platform as shown in Figure 3.6 to determine the out-of-plane level of each point.

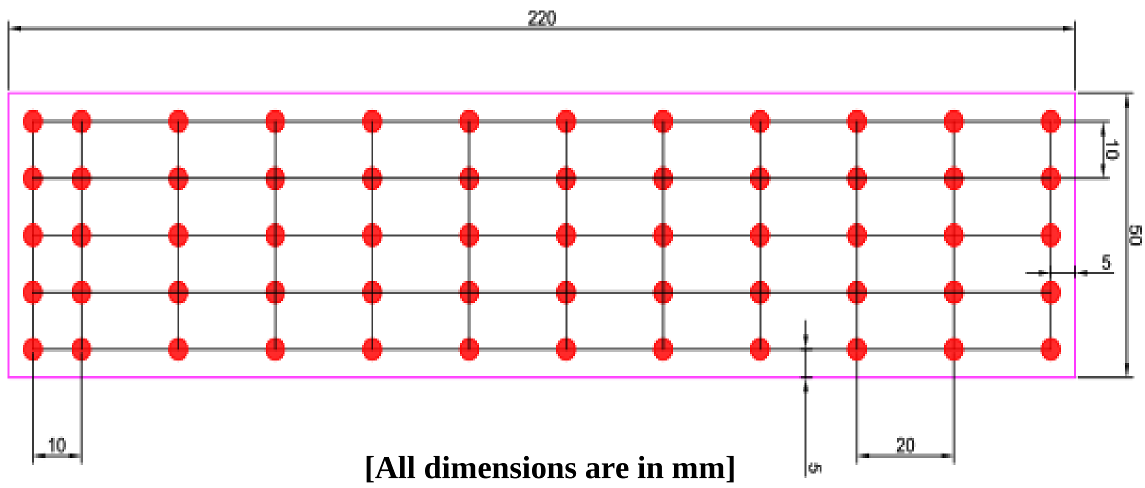

Figure 3.5: Typical mark points per shear face half.

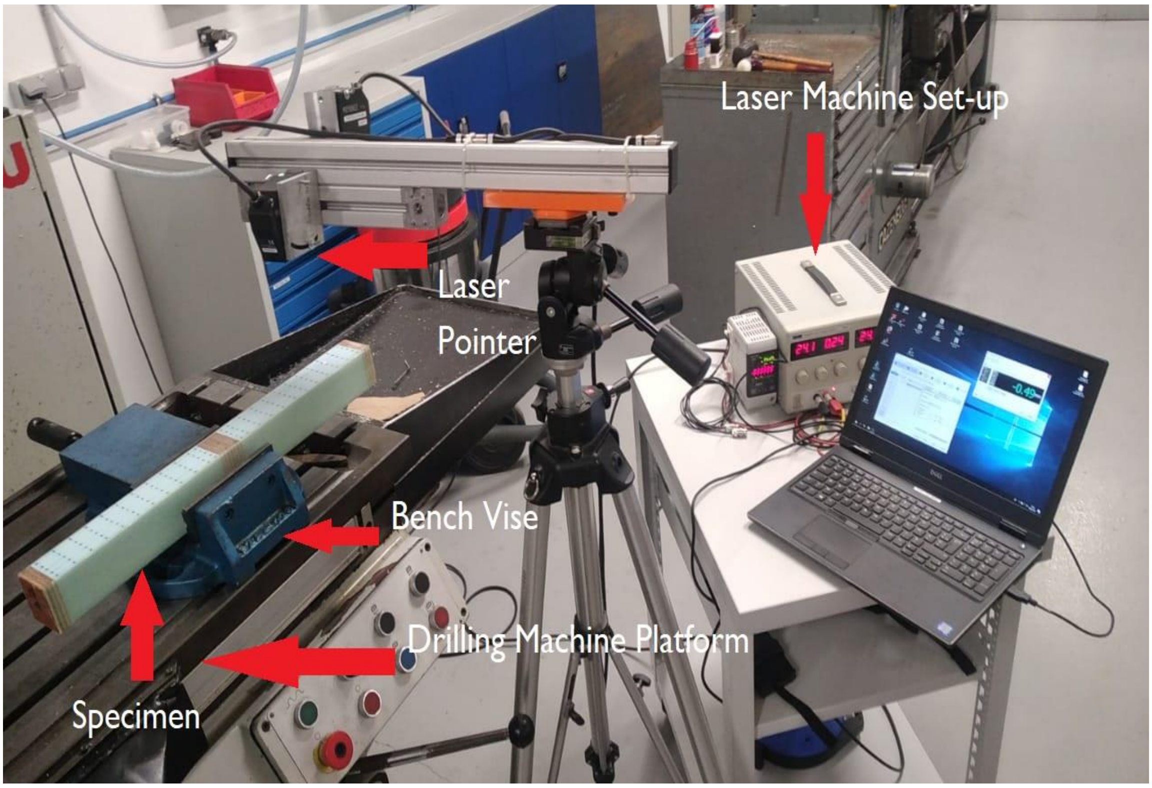

Figure 3.6: Laser displacement sensor measurement set-up.

The bench vise was carefully positioned on the milling machine platform and its horizontal balance was ascertained using a spirit level. After which the specimen was placed and balanced in the bench Vise clamp opening as in Figure 3.7. The laser pointer was positioned to light on the right bottom edge mark and the reading on the laser transducer was tarred to zero. This makes the right bottom edge mark the reference point for all other points measured on the skin. The level for each point was recorded from the screen of Keyence LK-GD500 distance reader software. The LK-G512 laser sensor exhibits a linear accuracy of ±0.02mm. The specimen was moved carefully in X and Y directions using the milling machine and the bench vise respectively with movement restricted in directions not in consideration. This procedure was repeated for all the specimens and their levels were recorded for further analysis.

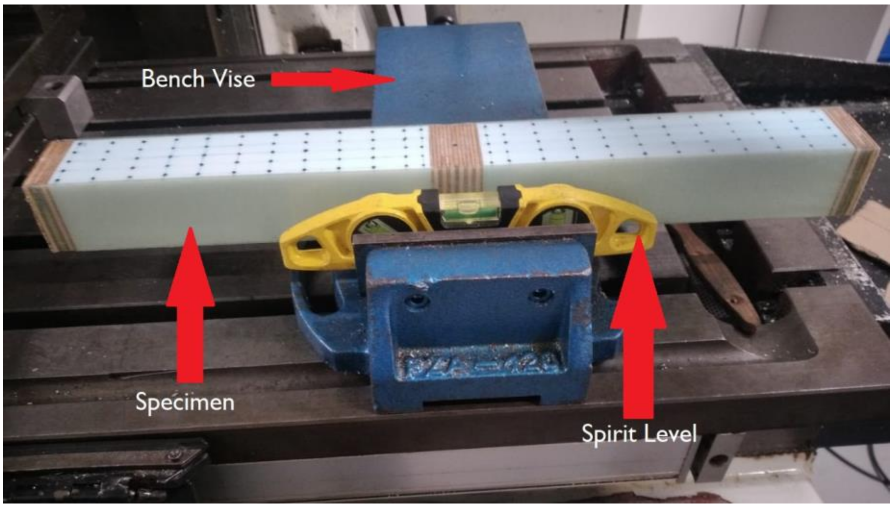

Figure 3.7: LDS set-up for horizontal balance setting.

3.4. Classical three-point bending test

Understanding the behaviour of sandwich structures subjected to combined loading conditions is essential for the design and analysis of various engineering applications as discussed in section 1.1. In order to accurately simulate real-time loading conditions experienced by structures experimentally, it is paramount to develop a testing configuration that closely resembles these conditions. For this research, the classical three-point testing method, in an inverse setup to Daniel's approach [17], was chosen due to its reliability and ease of setup. This inverse approach allows for the evaluation of the critical wrinkling stress under combined shear and compressive loads while allowing the set-up of other devices required to attain the objectives of this research.

The primary aim of this test is to subject the specimens into bending, generating axial or indirect compression forces, and shear forces. This is planned in-conjunction with some devices to study the behaviour such as LVDT displacement-control sensor, force sensor and digital image correlations (DIC). To use the DIC it is therefore vital to prepare speckle patterns on the sandwich specimens.

3.4.1. Sandwich sample preparation

Digital Image Correlation (DIC) is a highly useful and widely adopted non-contact measurement technique in the field of mechanical testing. It serves as a valuable tool for accurately determining strain and displacement parameters. The core principle of Digital Image

Correlation (DIC) involves comparing two images of the specimen, one taken before deformation and the other after deformation [58]. These images can be captured using one or multiple cameras, and the analysis is conducted by the software by examining the intensity variations of the speckle dot patterns applied on the surface of the specimens.

Furthermore, in order to prepare the specimens for the DIC, speckle pattern were randomly applied on the specimens. In a vacuum regulated chamber, two layers of white colour paint were first applied as in Figure 3.8a and after allowing to dry for about 1 hour, the black speckle dot patterns of average diameter of 0.2mm to 0.3mm were applied on the white paint as in Figure 3.8[b-d] to achieve almost 50:50 variation of black to white dots. This diameter can be graded to be good because a 5000 pixels camera over an area of interest (AOI) of 50mm by 470mm will require 0.376mm diameter at minimum of speckle dot patterns as shown in the calculation below.

$$pixel\ height = \frac{AOI}{Camera\ Resolution} = \frac{470}{5000} = 0.094\ mm$$

$$1\ t\hat{a}dre\ \geq\ 4\ pixel\ \approx 0.376\ mm$$

The speckle dots were applied only on the shear faces where initial out-of-plane imperfections were observed to be maximum for specimens A1 to A3 as in Figure 3.8b while the dots were applied on both sides of specimens A4 to A6 as shown in Figure 3.8[c-d].

3.4.2. Wrinkling failure test by three-point bending

The sandwich specimen was placed onto the base of the manually controlled three-point bending machine, and it was loosely clamped to prevent pre-loading in form of tension or compression on the specimen. The two extreme arms served as supports, while the middle arm acted as the point of load application as shown in Figure 3.9. To capture the vertical displacement during loading, a 25mm LVDT displacement sensor was installed on the middle arm. Additionally, a 2mVN HBM S9M/10kN force sensor was installed on the middle arm to measure the applied force. The LVDT displacement sensor and the force sensor were connected to an acquisition system for data storage.

For this particular study, two DIC cameras with a resolution of 5 Megapixels [image size of 2462 (H) x 2052 (V)] were utilized for specimens A1 to A3 to capture a single shear face, while four DIC cameras were used for A4 to A6, two per each shear face. These cameras were used to capture images at a rate of one frame per second (1fps). The cameras were focused on the areas of interest, that is the entire shear faces on the specimens, and the illumination sources were adjusted to this region accordingly.

[a]

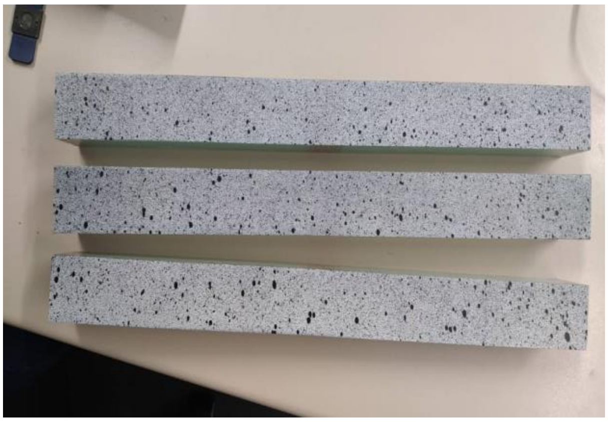

[b]

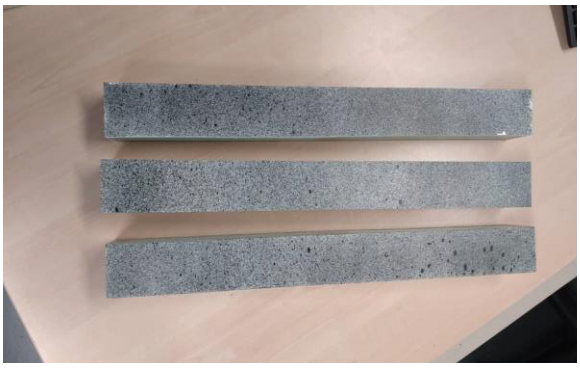

[c]

[d]

Figure 3.8: Sandwich specimens with [a] white colour paint; [b] speckle dot pattern [A1-A3]; [c] 1st face speckle dot pattern [A4 – A6]; and [d] 2nd face speckle dot pattern [A4 – A6].

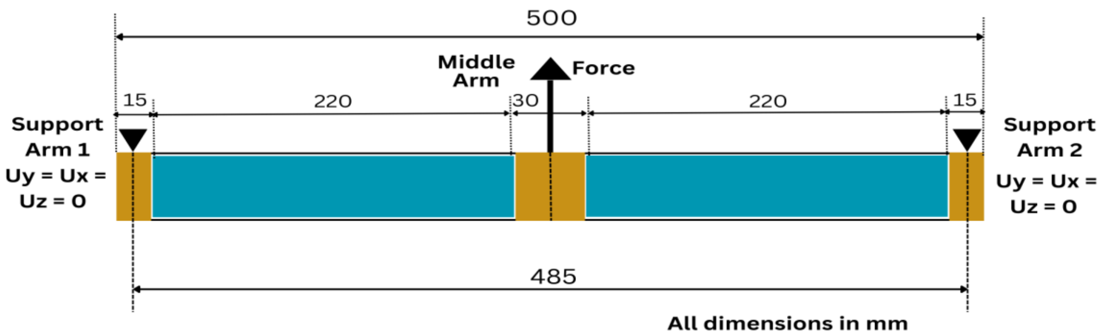

Figure 3.9: Classical three-point bending test loading scheme.

To ensure accurate measurements, the DIC cameras were calibrated using a 120 mm by 120 mm standard calibrator/speckle kit which featured 81 holes from Correlated Solutions as shown in Figure 3.10. The cameras were connected to the DIC data acquisition system, which includes VIC snap and VIC 3D software. An acquisition system was employed when two cameras were adopted and two acquisition systems when four cameras were used. VIC snap was employed to review image quality and capture calibration and specimen speckle images. More than 30 pictures were taken from different locations and angles to calibrate the cameras before capturing the speckle images. VIC 3D software was later used for the deformation analysis.

The experimental setup, as depicted in Figure 3.11, involved gradually application of force using manual control until wrinkles are developed. The middle arm exerted an upward force at the centre of the specimens, inducing tension at the top and compression at the bottom of the specimen, which is contrary to the three-point bending setup as employed by Daniel et. al. [17]. In addition, transverse shear forces were generated on the side faces of the specimen. Prior to testing, careful measures were taken to ensure that the middle arm acted precisely at the specimen's midpoint. This was achieved by balancing it with a standard rod on both faces of the arm, thus curtailing any additional bending effect stemming from eccentric loading.

To validate the precision and dependability of the outcomes, the displacement measurements captured by the LVDT displacement sensor were synchronized with the VIC 3D displacement records, revealing a flawless correspondence between the two as later discussed in section 4.2.1. Additionally, other important parameters such as the initial out-of-plane imperfection, out-of-plane displacement, the skin plane strain parameters (e_{xx}, e_{yy}, and e_{xy}), wavelength (λ), and the vertical displacement were obtained from the VIC 3D software.

Furthermore, using the above parameters, the wrinkling stresses of the specimens were calculated and subsequently compared using three distinct stress deriving approaches as discussed in section 4.4. The first approach involved employing the referenced theoretical models as outlined in Table 2.3. Secondly, the shear force distribution between the skins and the core, with the assumption that the shear strain within the core equates to that within the skin. The stresses were then computed from the load at first wrinkle as discussed in section 4.2.2. And lastly, plane stress theory implemented using MATLAB was utilized in conjunction with the strain parameters at the position of the first wrinkle extracted from the DIC measurements just before wrinkling to obtain the wrinkling stress as illustrated in Case A. On the other hand, Case B which involves wrinkling stress determination using DIC shear strain results and the elastic modulus of the fabric.

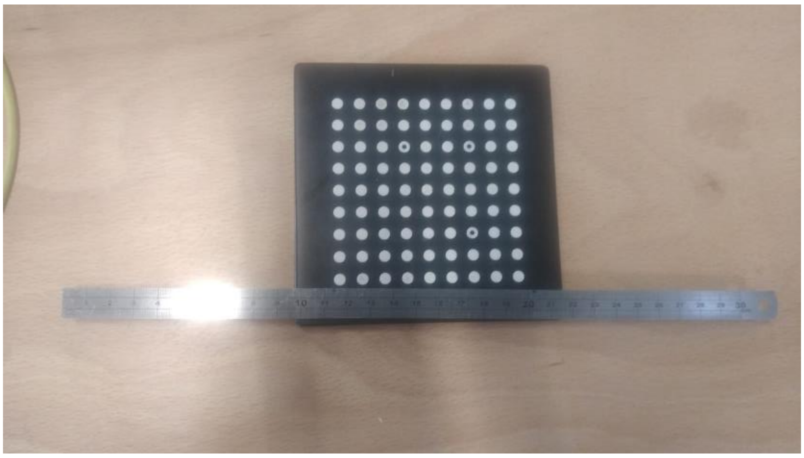

Figure 3.10: DIC camera standard speckle dot calibrator.

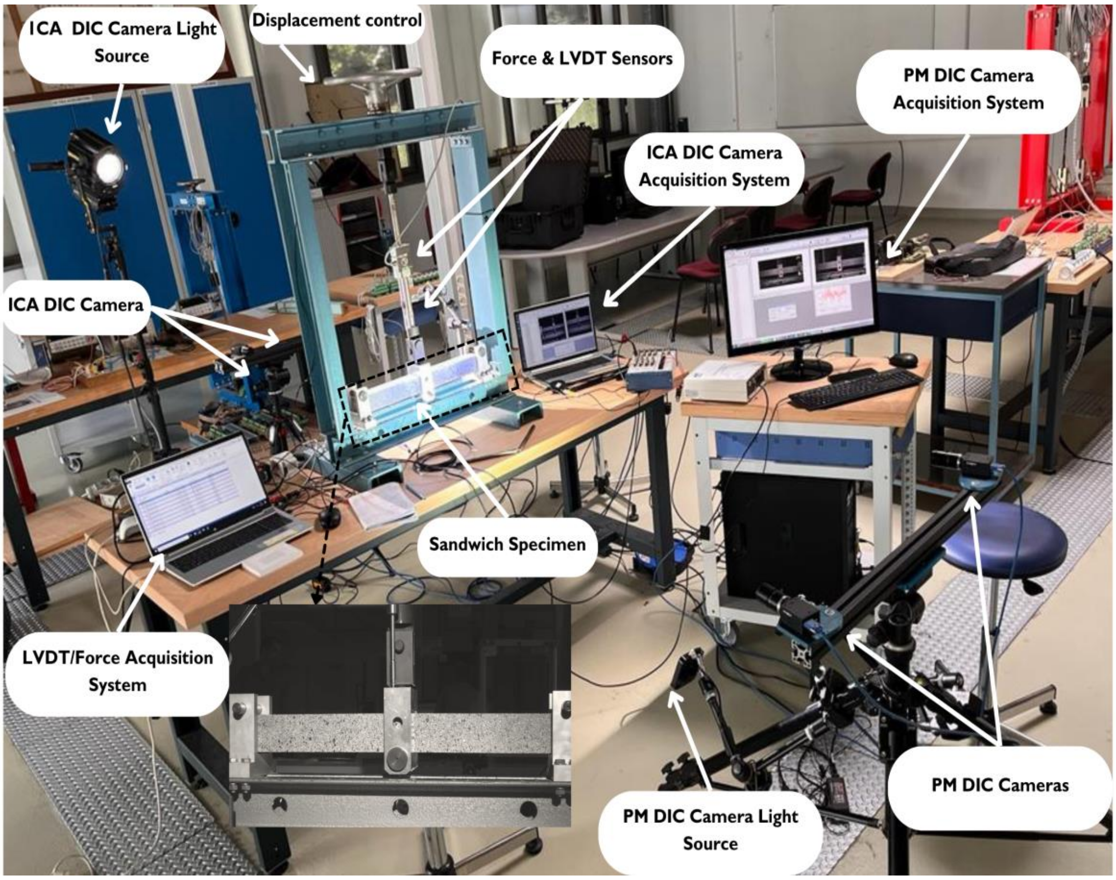

Figure 3.11: Classical three-point bending experimental set-up for wrinkling failure test.

THIS PAGE WAS INTENTIONALLY LEFT BLANK

4. CHAPTER 4. RESULTS AND DISCUSSION

This chapter of this dissertation elaborates upon the results of the experimental tests, along with discussion of the observations during the tests and the analysis of the obtained data. This section unveils the findings and draw meaningful insights from the experimental outcomes.

4.1. Initial out-of-plane displacement results and analysis

The initial out-of-plane displacement of the specimens A1 to A3 were measured using LDS and the DIC. Specimens A4 to A6 were exclusively subjected to DIC analysis.

4.1.1. Laser displacement sensor initial out-of-plane displacement results

The results of the LDS test give clear information about the level of imperfections on the facesheet better than mere visual inspection prediction [59]. The shape and magnitude vary for different specimens. This inconsistency can be linked to the method of manufacturing adopted, hand lay-up. Spatial portions of the specimens were observed to be resin-rich compared to other sections [12]. The resin-rich areas create humps on the facesheet surface. Futhermore, the plots of the out-of-plane deformations with the length of the specimen for each shear face of considered for specimens A1 to A3 are as illustrated in Figure 4.1 to Figure 4.3. The broken horizontal lines represent the level of the middle arm where the force would be applied during the 3-point bending test. Generally, a sudden increment was observed at point 360 ± 20mm in all the specimens, this may be due to a fabrication error in the mould used in preparing the specimens.

The measurement of the shear face 1 of specimen A1 follows a uniform gradient with the measured deformation range of 0.49mm to -0.09mm at the starting point and 460mm distance mark. Shear face 2 of specimen A1 has displacement range of 0.61mm. This amount to a range of 0.58mm as illustrated in Figure 4.1. The first wrinkle is predicted develop in the second part of the specimen, between 250 and 460mm. This is also applicable to specimens A2 and A3 in Figure 4.2 and Figure 4.3. In the initial segment of the specimens, a relatively consistent level is observed, while in the subsequent segment, there is a notable increase in the observed disparities among the point levels. For A2 specimens, shear face 1 and 2 exhibited an initial displacement range of 0.62mm and 0.68mm respectively. Similarly, in A3 specimens, shear face 1 and 2 displayed an initial displacement range of 0.70mm and 0.83mm respectively.

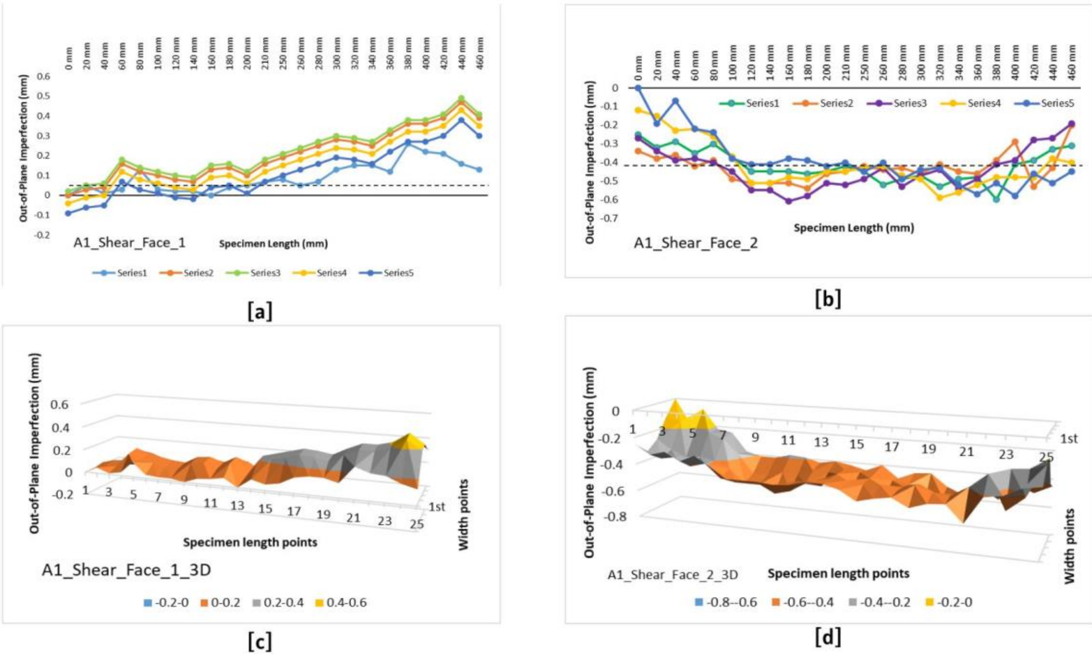

Figure 4.1: Specimen A1 LDS initial out-of-plane displacement results; [a] and [b] shear faces 1 and 2 2D-plots; [c] and [d] shear faces 1 and 2 3D-plots.

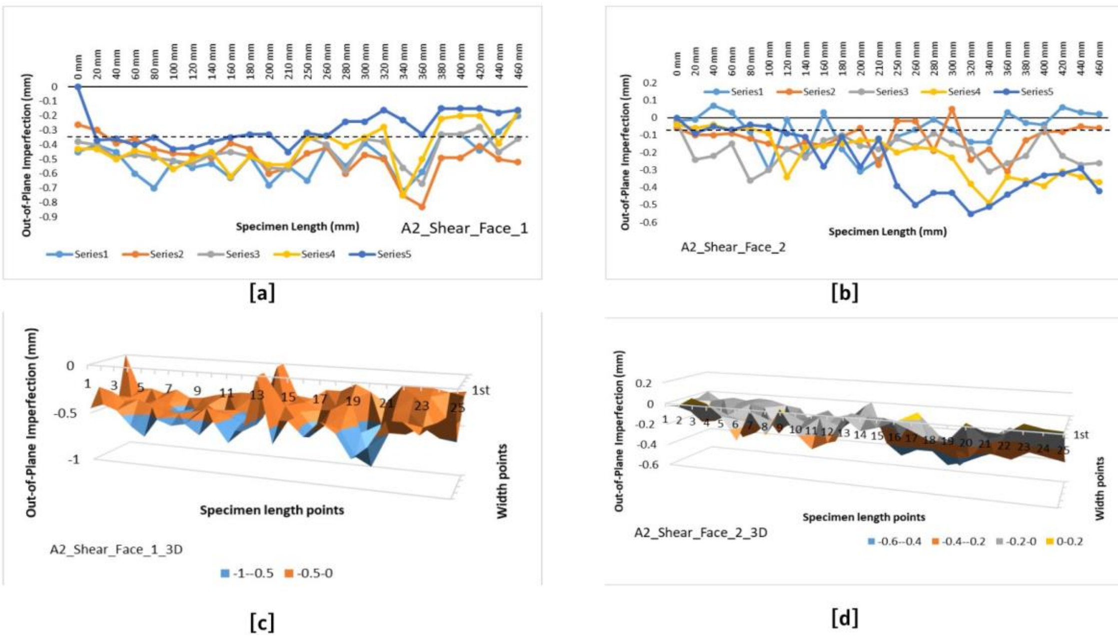

Figure 4.2: Specimen A2 LDS initial out-of-plane displacement results; [a] and [b] shear faces 1 and 2 2D-plots; [c] and [d] shear faces 1 and 2 3D-plots.

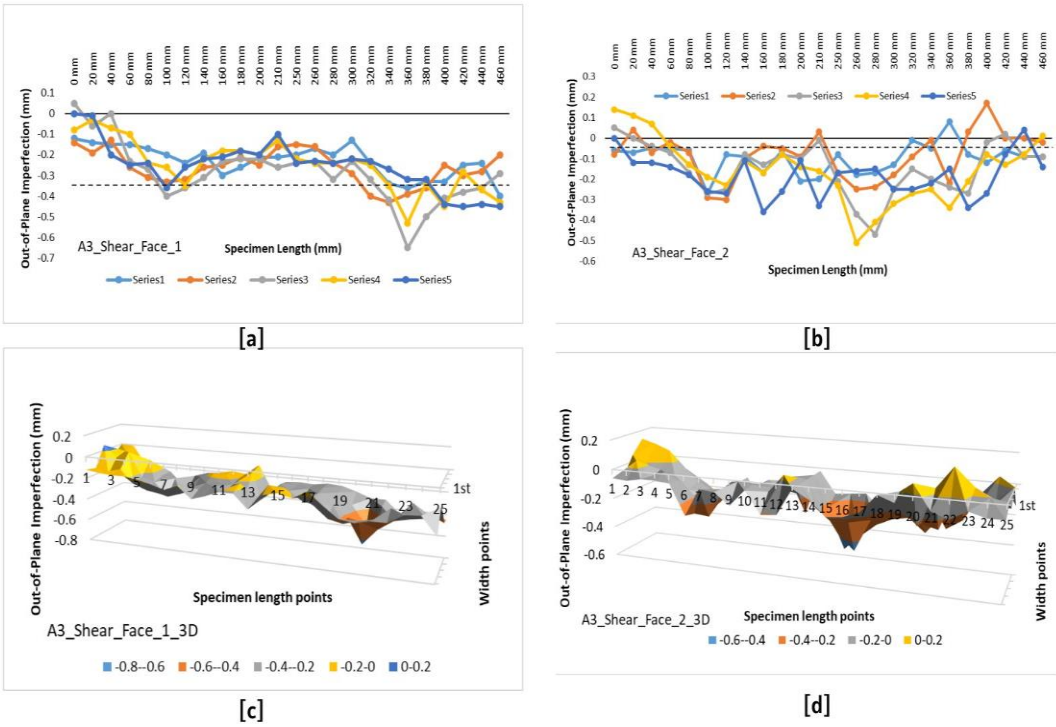

Figure 4.3: Specimen A3 LDS initial out-of-plane displacement results; [a] and [b] shear faces 1 and 2 2D-plots; [c] and [d] shear faces 1 and 2 3D-plots.

4.1.2. Digital image correlation initial out-of-plane displacement results

The DIC cameras were used to capture the initial state of the speckle-patterned faces of the sandwich specimens A1 to A6 before applying the load. These captured images were then analysed using the VIC-3D software [60]. By utilizing the software, 2D and 3D processed images were obtained, along with XZ-plane plots as illustrated in Figure 4.4 to Figure 4.9 that displayed colour dispersion in the Z-direction. This allowed for the examination of the initial out-of-plane displacement variation. The test results intensely depict the influence of contour and waviness present on the specimens, as evidenced by the dispersion pattern of the speckle dots. Generally, the specimens displace varieties of out-of-plane displacement. Specimens A1 to A3 demonstrated a fairly consistent pattern. The right faces exhibited an upward convex shape towards the middle arm, while the left faces displayed a relatively straight path at the centre. On the other hand, specimens A4 to A6 showed an upward convex shape for both faces. This observation can be attributed to the fact that these specimens were manufactured in distinct batches and moulds. This indicates that the initial imperfections were primarily concentrated around the central region for all the specimens.

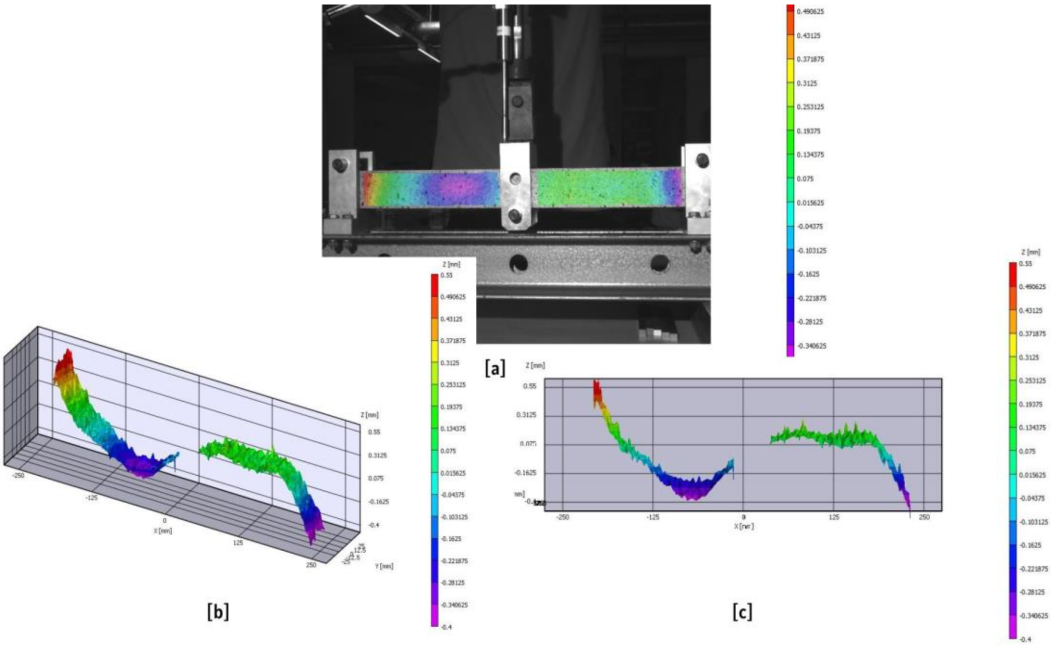

Figure 4.4: Specimen A1 DIC initial out-of-plane displacement result in [a] 2D-plot; [b] 3D-plot; and [c] XZ-plane plot.

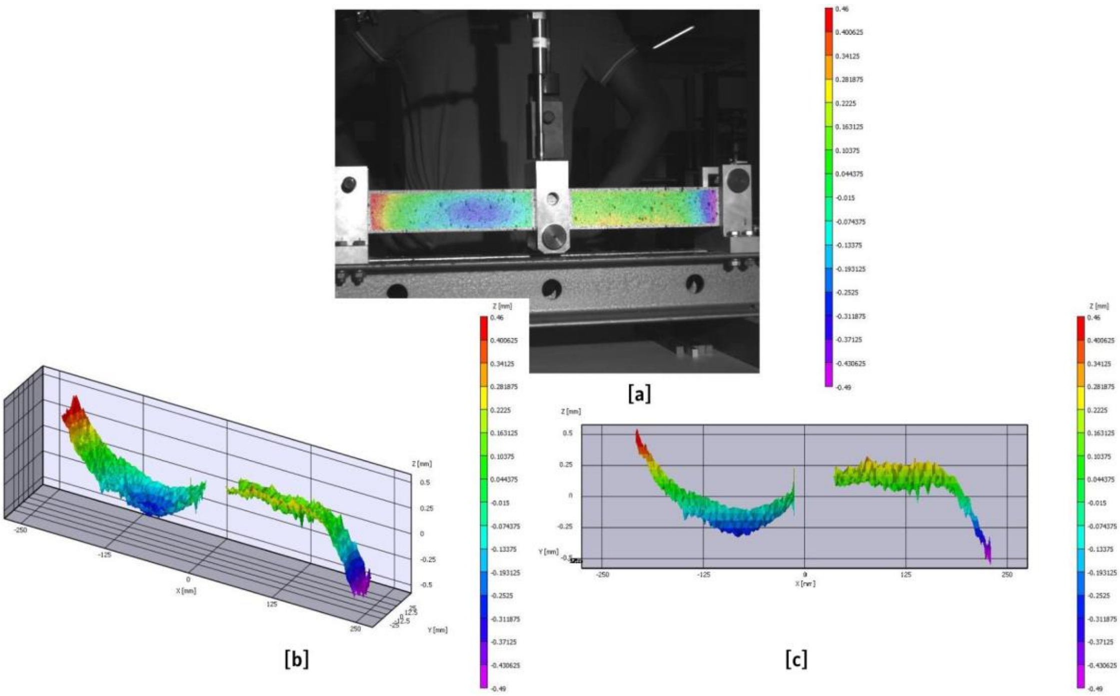

Figure 4.5: Specimen A2 DIC initial out-of-plane displacement result in [a] 2D-plot; [b] 3D-plot; and [c] XZ-plane plot.

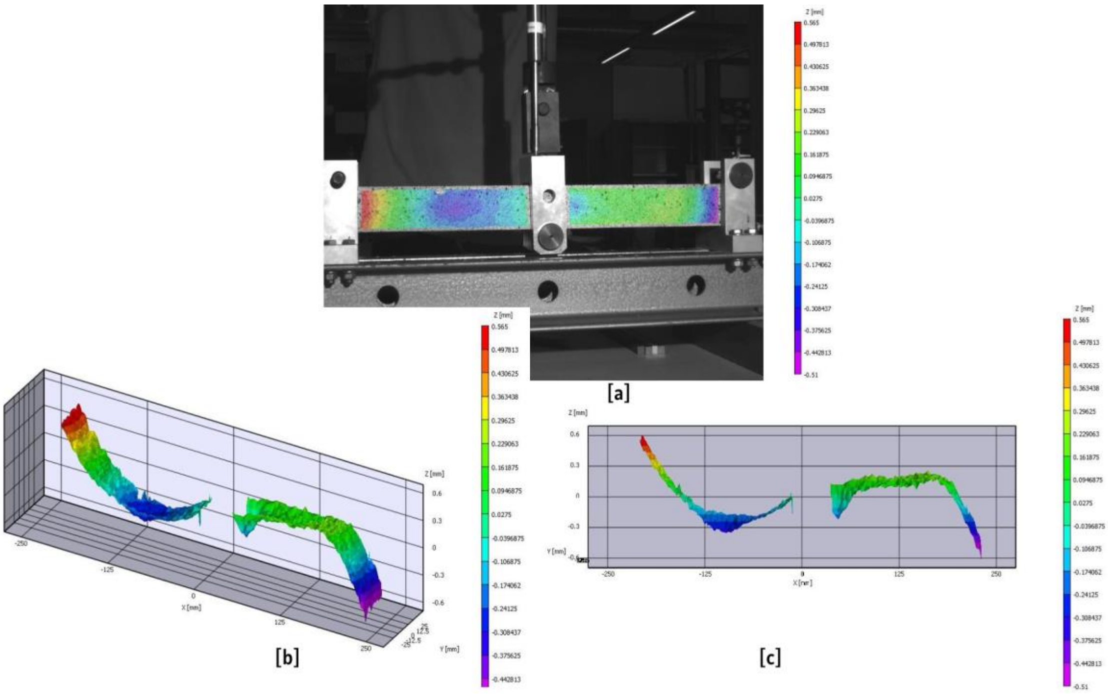

Figure 4.6: Specimen A3 DIC initial out-of-plane displacement result in [a] 2D-plot; [b] 3D-plot; and [c] XZ-plane plot.

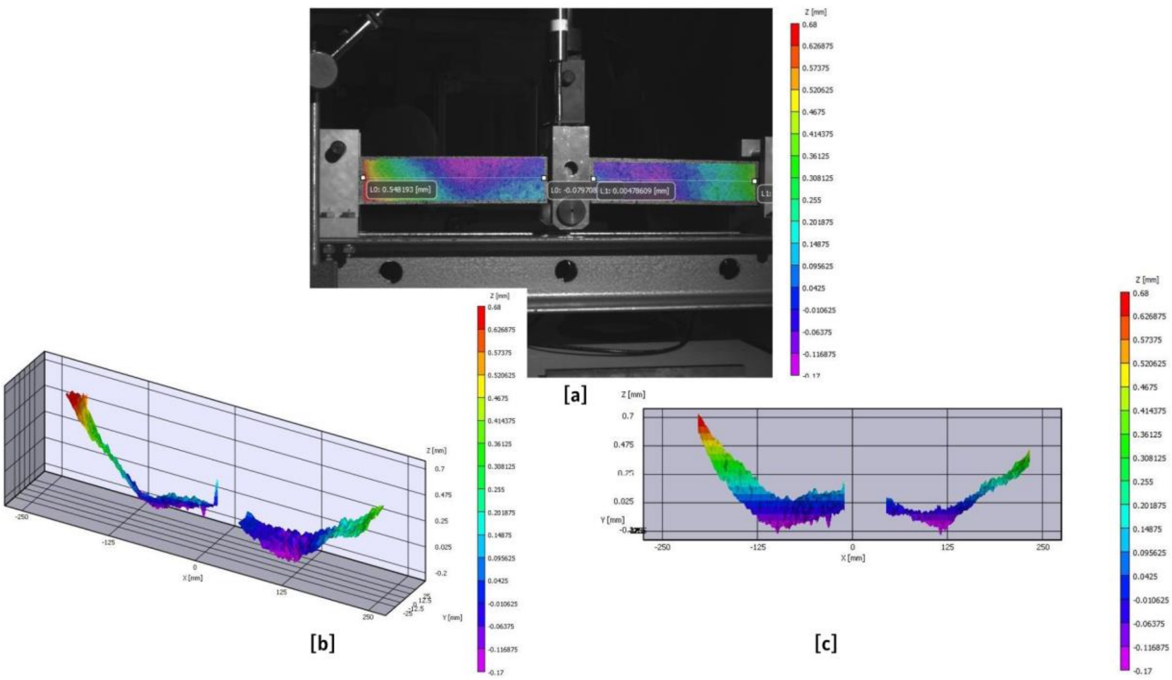

Figure 4.7: Specimen A4 DIC initial out-of-plane displacement result in [a] 2D-plot; [b] 3D-plot; and [c] XZ-plane plot.

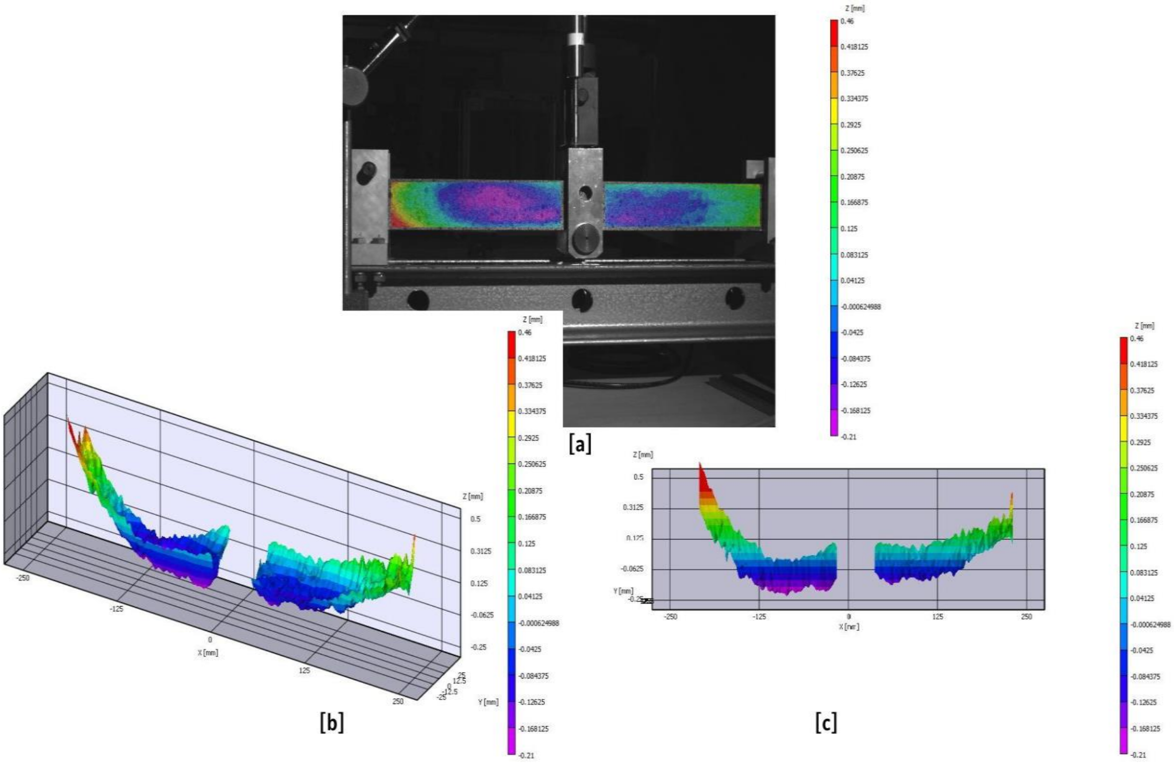

Figure 4.8: Specimen A5 DIC initial out-of-plane displacement result in [a] 2D-plot; [b] 3D-plot; and [c] XZ-plane plot.

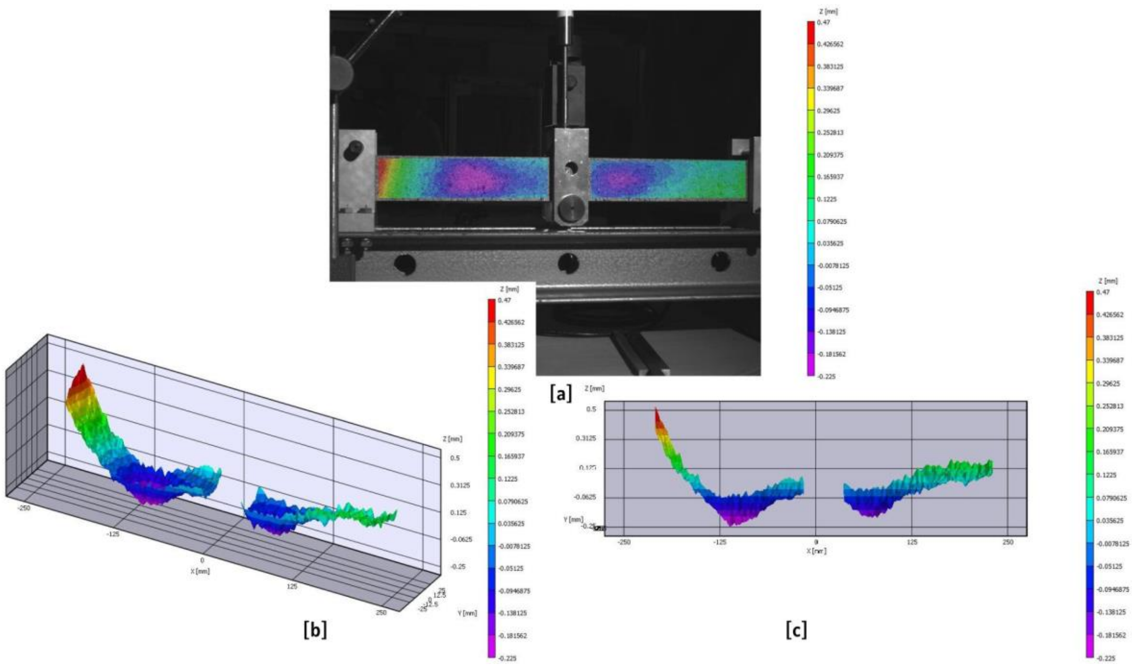

Figure 4.9: Specimen A6 DIC initial out-of-plane displacement result in [a] 2D-plot; [b] 3D-plot; and [c] XZ-plane plot.

4.1.3. DIC and LDS results comparison

The results of the two approaches were compared. The range of the global initial out-of-plane displacement for the methods were presented as Figure 4.10. On average, the measured range was less than 1.00mm. The results from specimens A4 to A6 using the LDS were non-existent, as these tests were not executed. It is worth noting that the results obtained from the LDS may be considered less accurate compared to the DIC results. This is because the LDS results were obtained from discrete points along the face, while information about other points was excluded. Nevertheless, the results obtained from the DIC technique can be reasonably correlated with the data obtained from the LDS in Figure 4.4 to Figure 4.6 and Figure 4.1 to Figure 4.3 respectively.

In conclusion, the results from the DIC and the LDS reviewed specimens A1 to A3 has maximum downward depression between 120mm and 200mm distance mark and maximum upward depression between 340mm and 420 mm as in Figure 4.4 to Figure 4.6. In contrast specimens A4 to A6 showed a downward depression in this region. Therefore, it can be inferred that the development of wrinkles can be predicted to occur around the central area of the specimens since the initial global imperfections are localized intensively there [3].

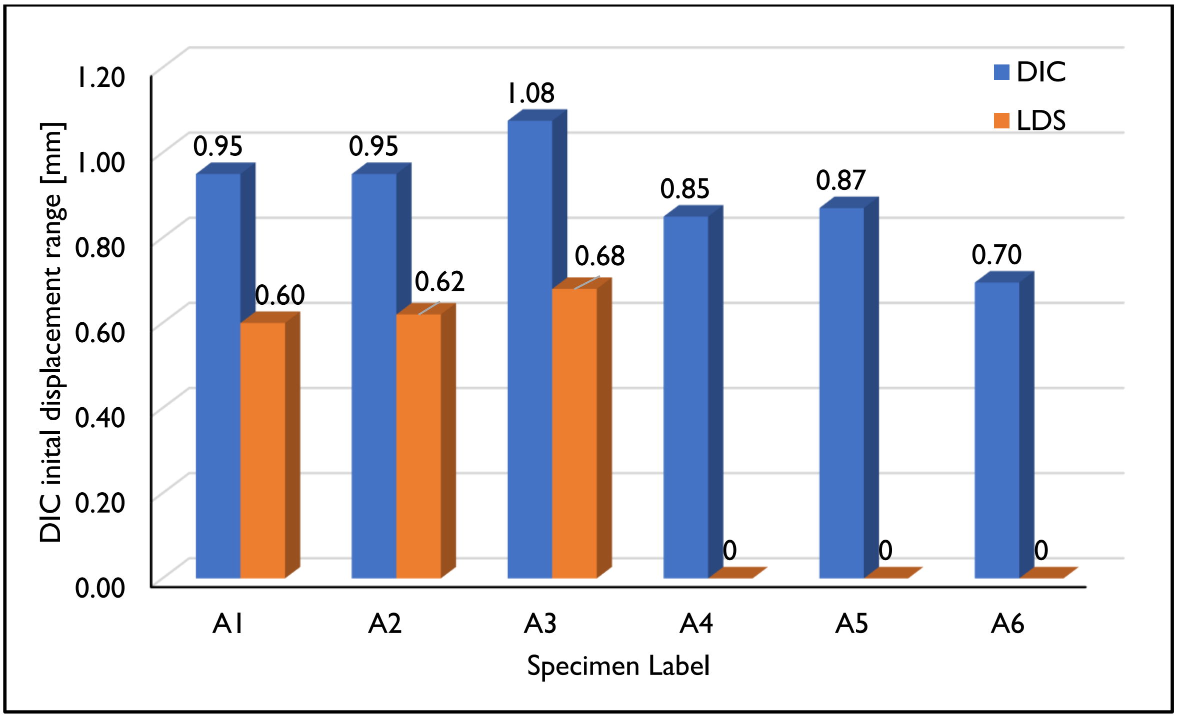

0 – means no LDS test result is available for the specimen.

Figure 4.10: DIC and LDS global initial out-of-plane displacement range summary.

4.2. Wrinkling test by simple classical three-point bending

The outcomes of the classical three-point bending tests at ISAE SUPAERO, conducted to induce wrinkling failure in the specimens, were documented, and relevant observations were made throughout the testing process.

4.2.1. Data synchronization with displacement-time results

The displacement data obtained from both the LVDT displacement sensor and the VIC snap software for the DIC cameras were carefully synchronized. This measure was adopted to guarantee precise synchronization and alignment of the displacement output parameter. This is necessary due to the inherent delayed launch time of the acquisition systems. This alignment was established before proceeding with the plotting of the displacement output against the force output and other subsequent analyses. The corresponding plots for specimens A1 to A3 and A4 to A6 are presented in Figure 4.11 and Figure 4.12 as a, b and c respectively.

These results provide detailed insights into the test history, illustrating the progression of the applied compressive force trajectory over the testing period. The flat sections observed in the curves (O-P) indicate the moments when the specimens were carefully examined for the development of wrinkling wave and a brief stop in the specimen loading. Additionally, the downward slope (L-P) represents the loading phase of the test, while the upward slope corresponds to the unloading phase (U-P) of the experiment as shown in the Figures. The abrupt drop observed in Figure 4.12b appears because the 25mm limit of the LVDT was reached. Generally, the results show a good correlation as the pattern of the LVDT displacement and the DIC data appears to be in good agreement for all cases.

4.2.2. Classical three-point bending test results analysis and wave evolution

For the sake of this analysis Figure 4.13 would be used as reference for all the specimens. It is important to recall that in section 3.4.2, it was emphasized that only sides A and B were observed by the DIC for specimens A1 to A3 while all the sides were monitored by the DIC for specimens A4 to A6. The force to local shear strain, e_{xy} at the initial wrinkling location, and force-displacement relationship as wrinkles evolve on the sides and wavelength of the wrinkles formed for each of the specimens were discussed in this section.

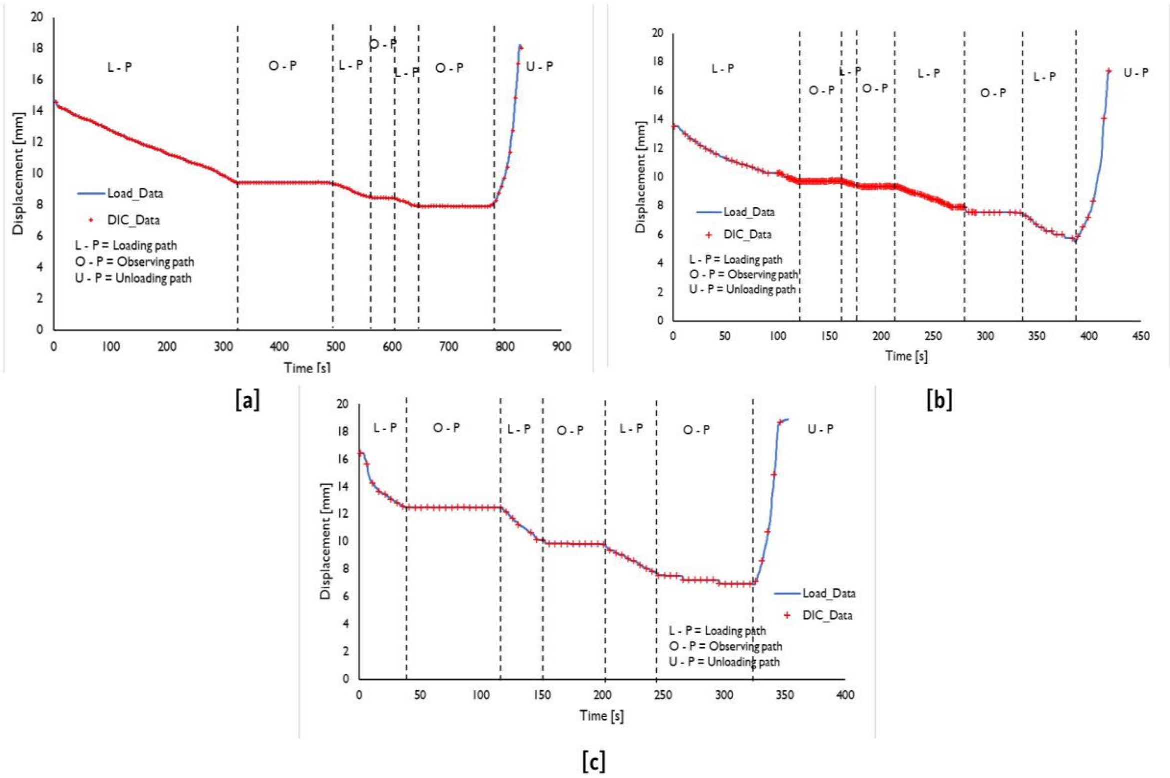

Figure 4.11: Displacement-time synchronization: [a] A1; [b] A2; and [c] A3.

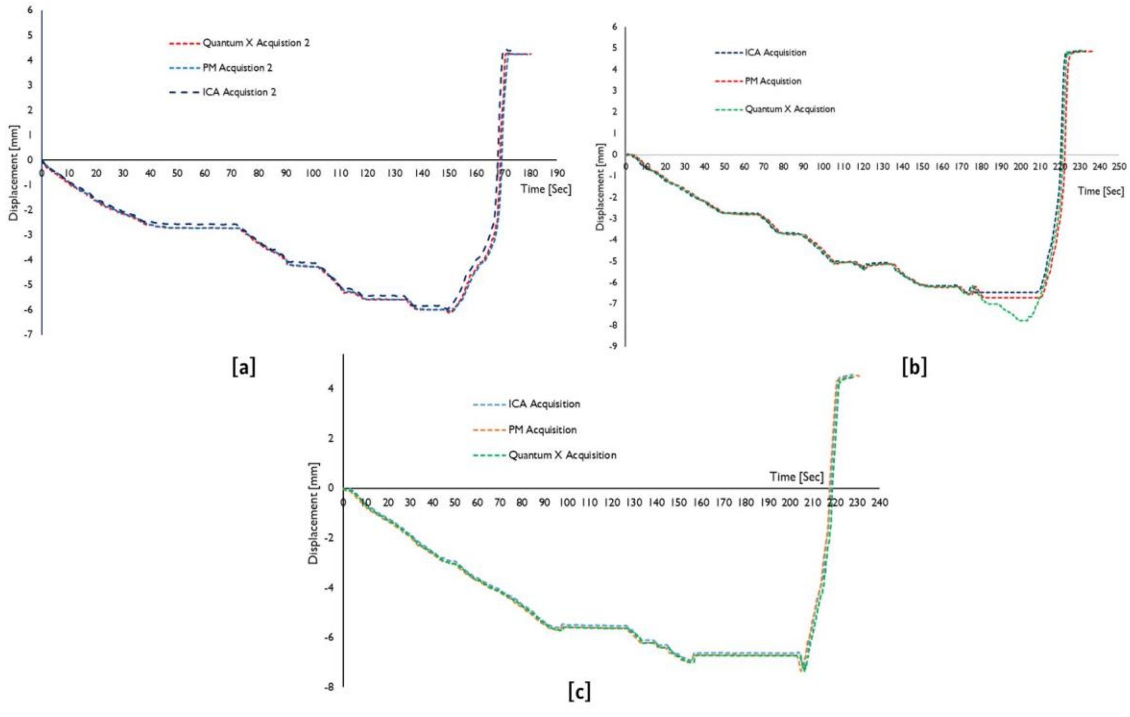

Figure 4.12: Displacement-time synchronization: [a] A4; [b] A5; and [c] A6.

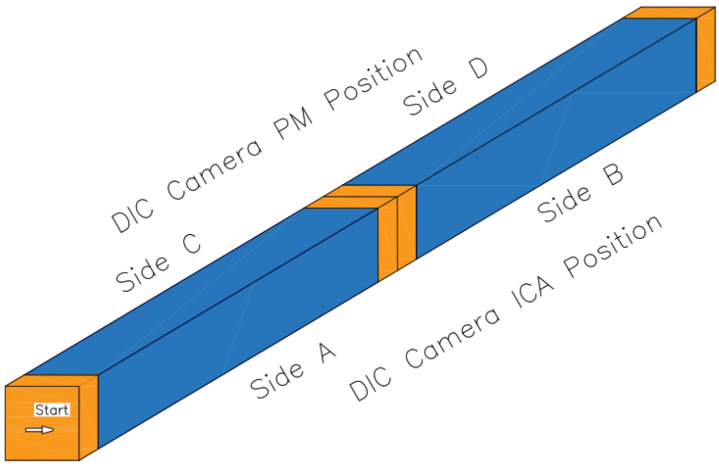

Figure 4.13: Schematic representation of specimen parts.

a. Specimen A1

At a load of 3258N as shown in Figure 4.14 the wrinkle appeared suddenly and explosively on the sides B and D. Other sides showed no wrinkling formation. The strain shows a quasi-linear path as the load increases, then turns non-linear due the wrinkle development because the strain is calculated at the wrinkling location. Moreover, wrinkle waves were observed to develop as the unloading process progresses from 2300N to 2100N. This infers that the appearance of the first wave instigates other short waves as the load reduces.

However, Figure 4.15 gives information on the applied force against the local shear strain at the point where the wrinkle first developed on face B. The shear strain at this point just before the wrinkling wave appeared was -5107με on Side B while on side A it was averagely 4421με. The occurrence of the wrinkling mode led to the disappearance of the speckle patterns for the DIC readings, resulting in a strain value of zero. Notably, the strain on side A was observed to decrease to 3631με, even in the absence of wrinkling development. This reduction in strain can be attributed to a change in the overall structural stiffness. This particular region in side B, ranging from 320mm to 400mm, exhibited a high degree of waviness on both sides [12], as revealed in the LDS and DIC results in section 4.1 [3].

Furthermore, the wavelength of the wrinkles was estimated from the out-of-plane displacement in the z-direction, w, to the length along the x-direction as Figure 4.16. This value was divided with $\sqrt{2}$ to obtain the equivalent wavelength required. The half-wavelength, a, was estimated experimentally to be $0.09t_{core}$. The first wrinkle exhibited an inward shape on side B, indicating a localization of compressive force on the elastic core.

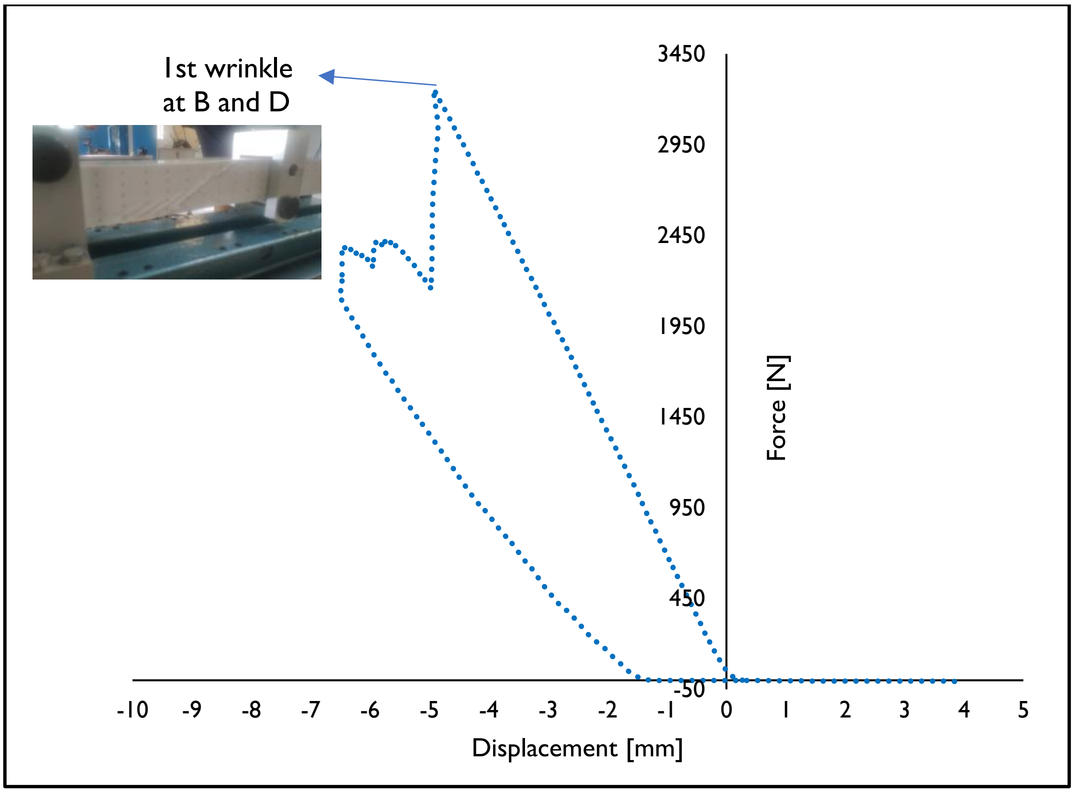

Figure 4.14: Specimen A1 load-displacement relationship plot.

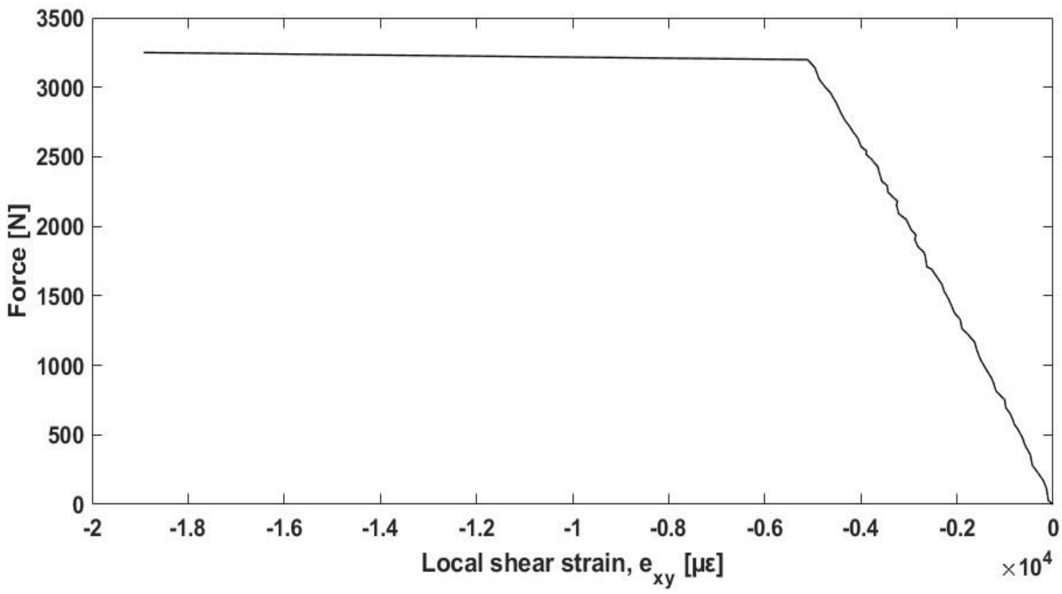

Figure 4.15: A1 side B force-local shear strain relationship curve.

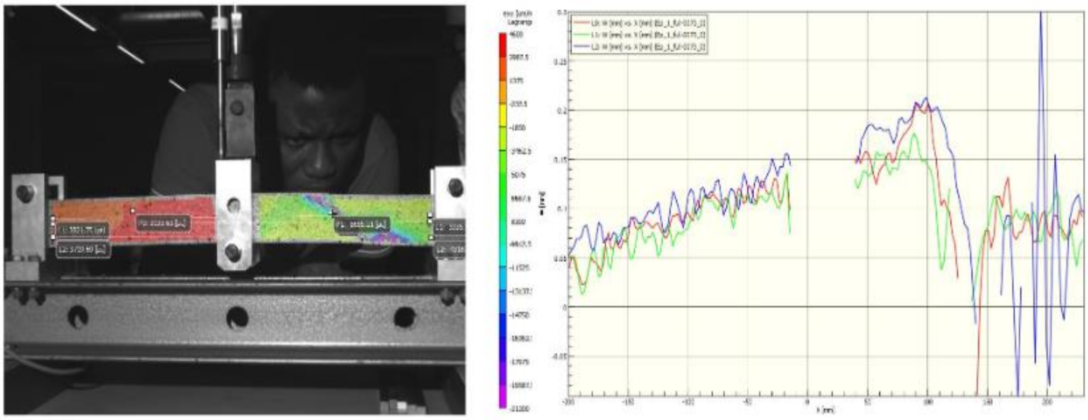

Figure 4.16: A1 out-of-plane deformation vs x-direction relationship with wave plot.

b. Specimen A2

For this sample the first local wrinkle was observed on side C at a load of 2654N which led to a drop in force as illustrated in Figure 4.17. This was captured by mere visual observation as there was absence of DIC on this side. The shear failure became apparent with possibility of a core shear failure as the load increased to 3669N as in Figure 4.17 which resulted into a large drop in the force applied to about 2095N. Subsequently, wrinkle emerged on side A when the load drop was further increased to 2172N, whereas sides B and D did not exhibit the development of any wrinkle wave.

Moreover, Figure 4.18 shows the relationship between the applied force and the local shear strain at the point where the wrinkle appeared on side A. The effect of the first wrinkle can be seen on the shear strain trajectory. The slope of the curve was distorted and later deviated. Before the load reached 2172N, that is before wrinkle finally appeared on side A, the strain was obtained to be 7734με. At this point the average shear strain on side B was -4650με which dropped to -3294με after wrinkling developed. The position on side C links to a notable depression of -0.8mm between the 300mm and 400mm marks [3], as apparent in the LDS result presented in section 4.1.1. Later, the wave appeared at side A within the region spanning from 250mm to 360mm, where a significant number of disparities were also observed [12].

Furthermore, the wavelength of the wrinkles was estimated from the out-of-plane displacement in the z-direction, w, to the length along the x-direction as Figure 4.19. This value was divided with $\sqrt{2}$ to obtain the equivalent wavelength required. The half-wavelength, a, estimated experimentally to be $0.177t_{core}$. This value is high due to the outburst of the wave that led to widened wavelength. The first wrinkle exhibited an outward shape at Side A, indicating a localization of tensile force on the elastic core.

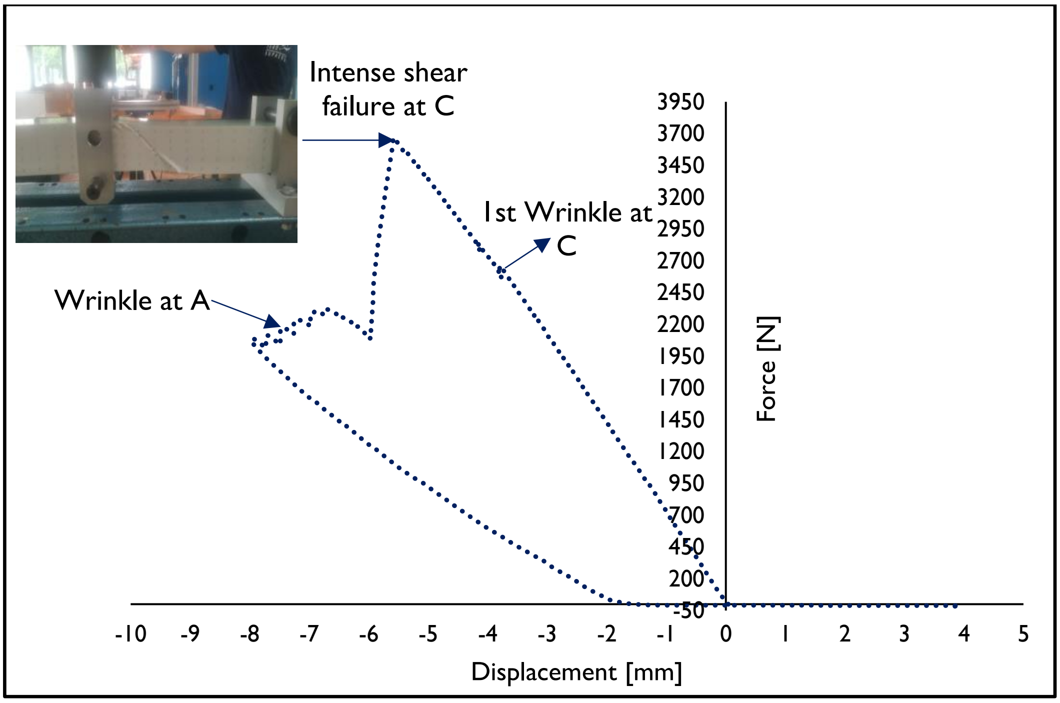

Figure 4.17: Specimen A2 load-displacement relationship plot.

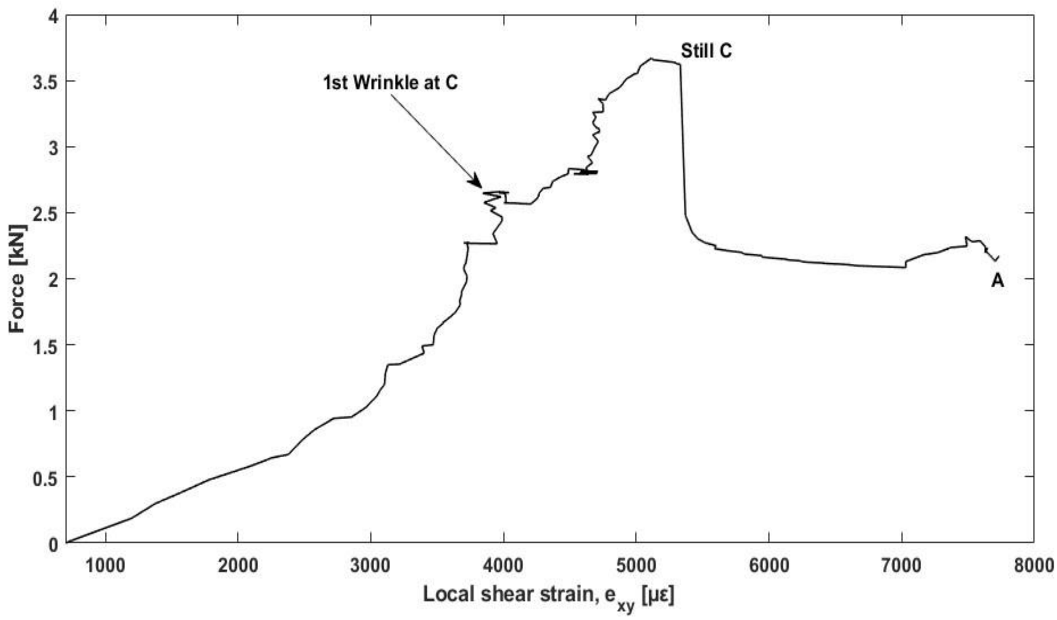

Figure 4.18: A2 side A force-local shear strain relationship curve.

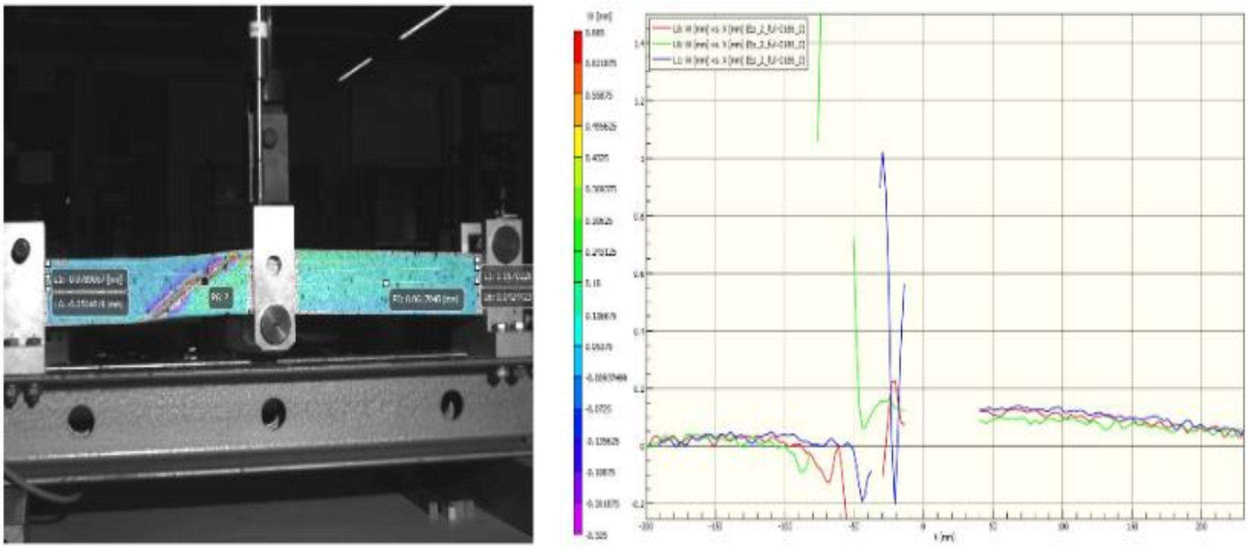

Figure 4.19: A2 out-of-plane deformation vs x-direction relationship with wave plot.

c. Specimen A3

This sample manifested wrinkling at an earlier stage compared to A1 and A2. The initial wrinkling was observed on side D when the load reached 1438N, as illustrated in Figure 4.20. Subsequently, the applied load was progressively increased until reaching 2441N, resulting in the appearance of wrinkles on side B. It is important to note that the specimen experienced debonding between the skin and the core during testing [17], led to the wrinkling failure occurring earlier than anticipated. Sides A and C did not exhibit the development of any wrinkle wave.

Moreso, as illustrated in Figure 4.21 a linear relationship was recorded until when the first wrinkle developed on side D. Just before the failure appeared, the shear strain parameter on sides A and B were 2009με and -2204με respectively. Side B increased to -2350με but A decreased to 1968με after the wrinkling on side D had been developed. The shear strain level on side B was recorded by the DIC as -9138με just prior to the occurrence of wrinkling on this side. This phenomenon can be attributed to the influence of debonding [12] within the structure, which prompts an extension of shear strain levels.

Additionally, the wavelength of the wrinkles was estimated from the out-of-plane displacement in the z-direction, w, to the length along the x-direction as in Figure 4.22. This value was divided with $\sqrt{2}$ to obtain the equivalent wavelength required. The half-wavelength, a, was estimated experimentally to be $0.11t_{core}$. The first wrinkle exhibited an inward shape at Side B, indicating a localization of compressive force on the elastic core.

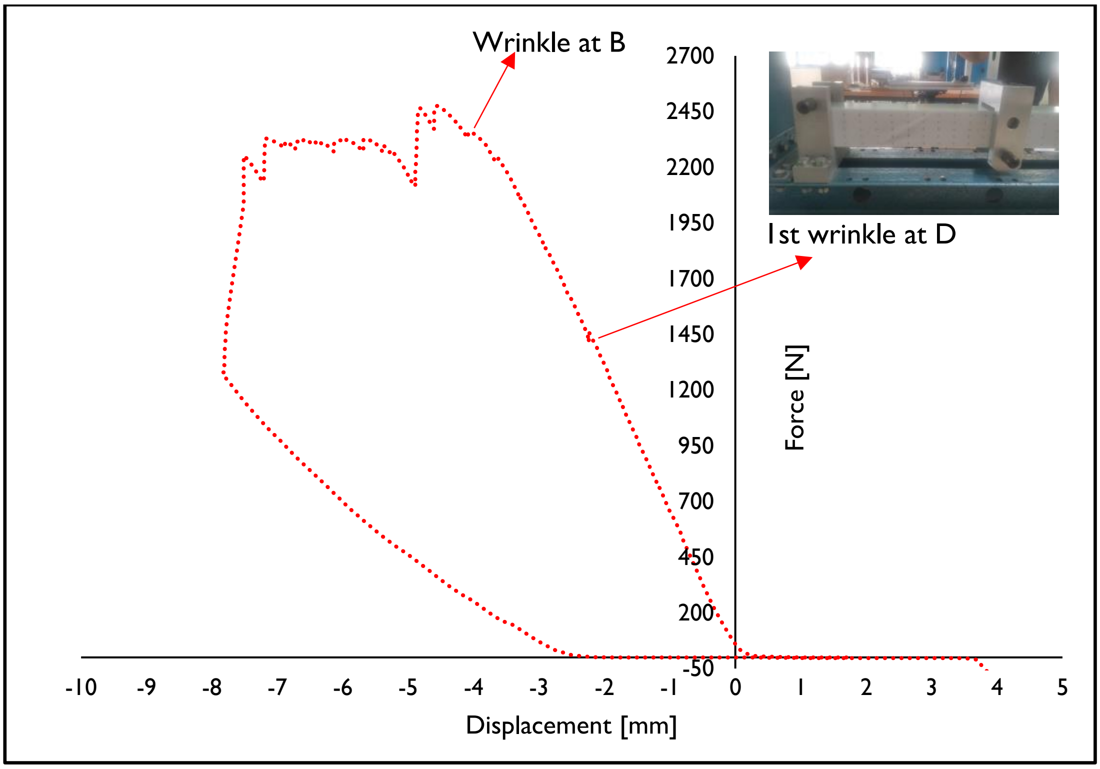

Figure 4.20: Specimen A3 load-displacement relationship plot.

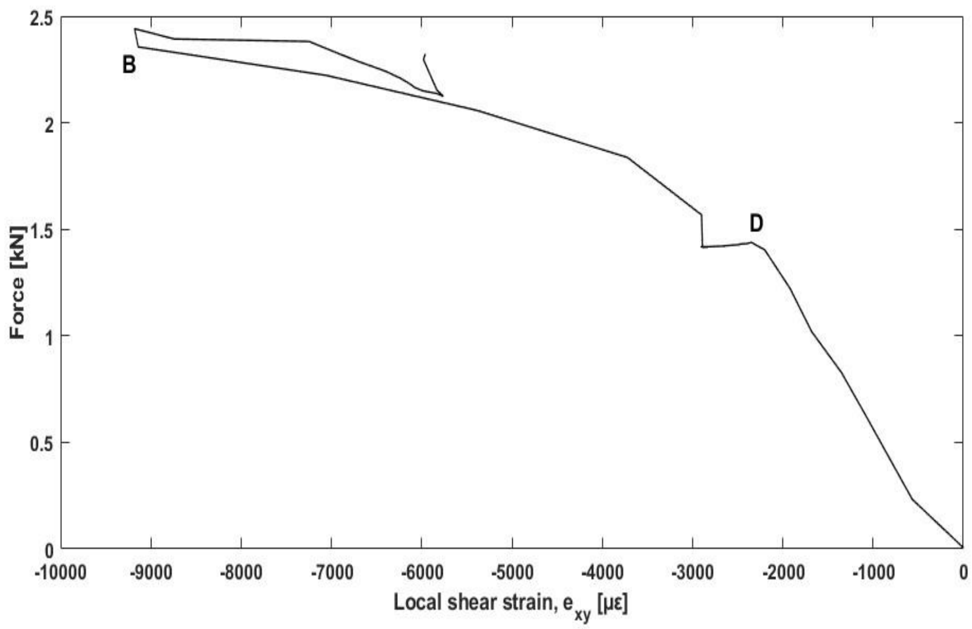

Figure 4.21: A3 side B force-local shear strain relationship curve.

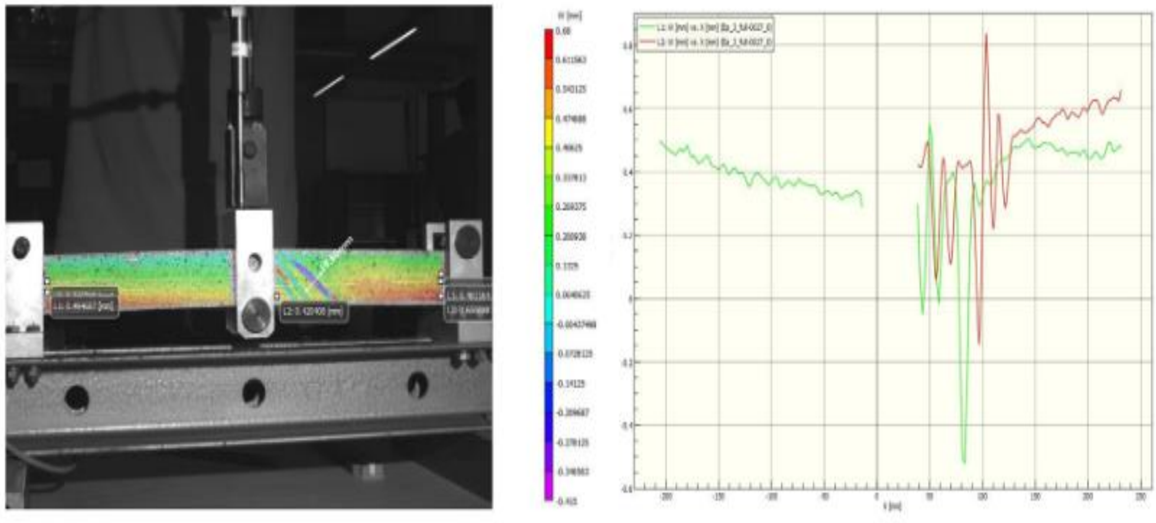

Figure 4.22: A3 out-of-plane deformation vs x-direction relationship with wave plot.

d. Specimen A4

Sample A1 demonstrated wrinkles on sides A, B, and D. The first wrinkle emerged on side B when the applied load reached 1486N. The localized impact of this wrinkle exhibited relatively minor effects on the load-displacement curve, as depicted in Figure 4.23. The load continued to increase to 1928N, at which point the wrinkle became apparent on side A, and around 2661N, it materialized on side D. From the curve, it is obvious that the occurrence of wrinkles on sides B and A precipitated a change in the overall stiffness of the structure. No wrinkle was noted on side C throughout the test progress.

Additionally, Figure 4.24 illustrates the quasi-linear relationship between the global applied force and the shear strain at the point of the first wrinkle occurrence on side B. This transitioned into a wrinkle formation at a strain level of -2749με on side B. It's worth noting that the presence of the wrinkle led to a force plateau, subsequently transitioning into a non-linear trajectory for the shear strain [3]. At the point where the wrinkle emerged on side A, the shear strain was 3769με. However, the shear strain on side B exhibited noise afterward, prior to the occurrence of the wrinkle on side D. Consequently, this information was omitted from the plot.

Furthermore, the wavelength of the wrinkles was estimated from the out-of-plane displacement in the z-direction, w, to the length along the x-direction as in Figure 4.25. This value was divided with $\sqrt{2}$ to obtain the equivalent wavelength required. The half-wavelength, a, was estimated experimentally to be $0.105t_{core}$. The first wrinkle exhibited an inward shape at Side B, indicating a localization of compressive force on the elastic core.

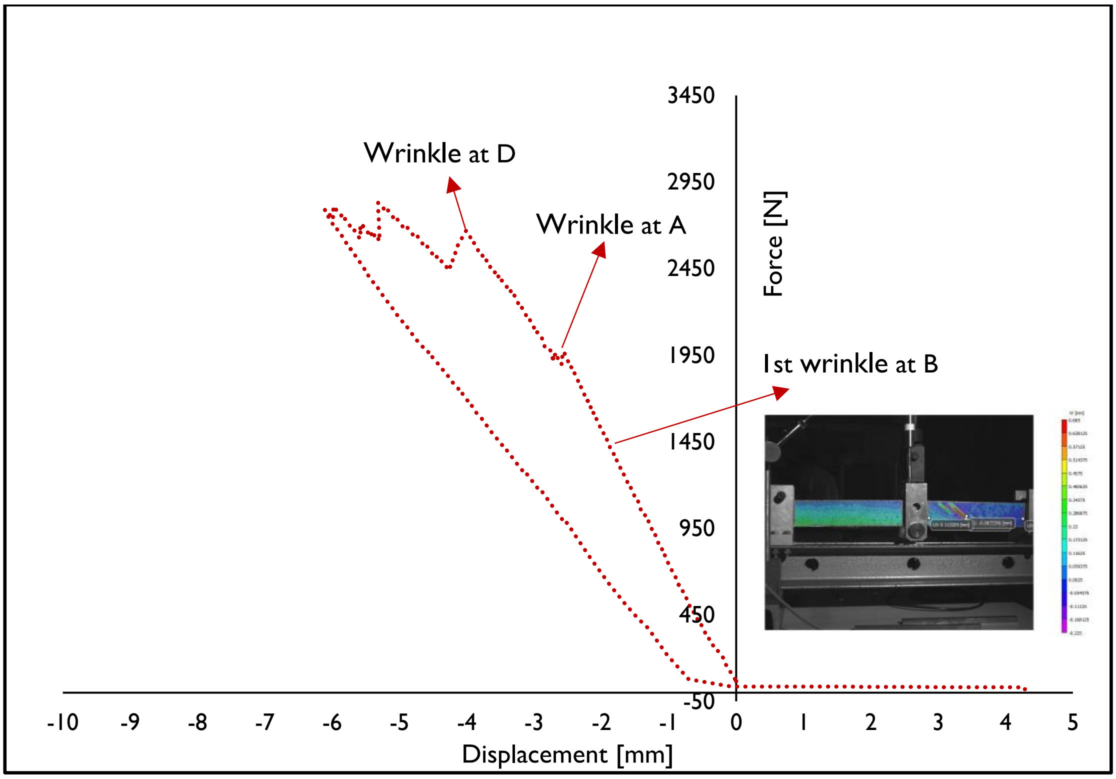

Figure 4.23: Specimen A4 load-displacement relationship plot.

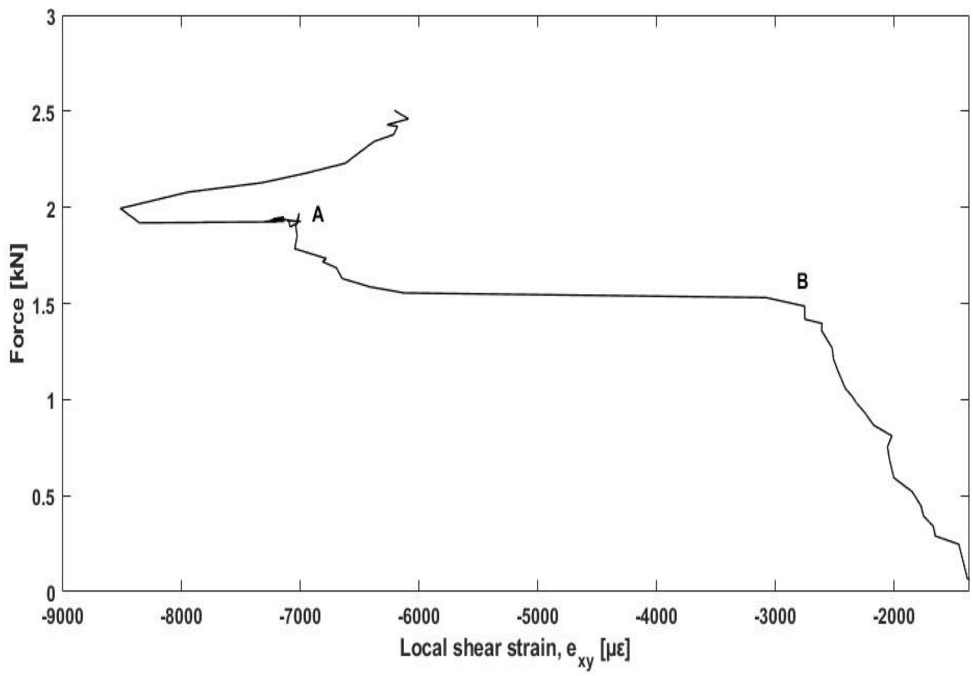

Figure 4.24: A4 side B force-local shear strain relationship curve.

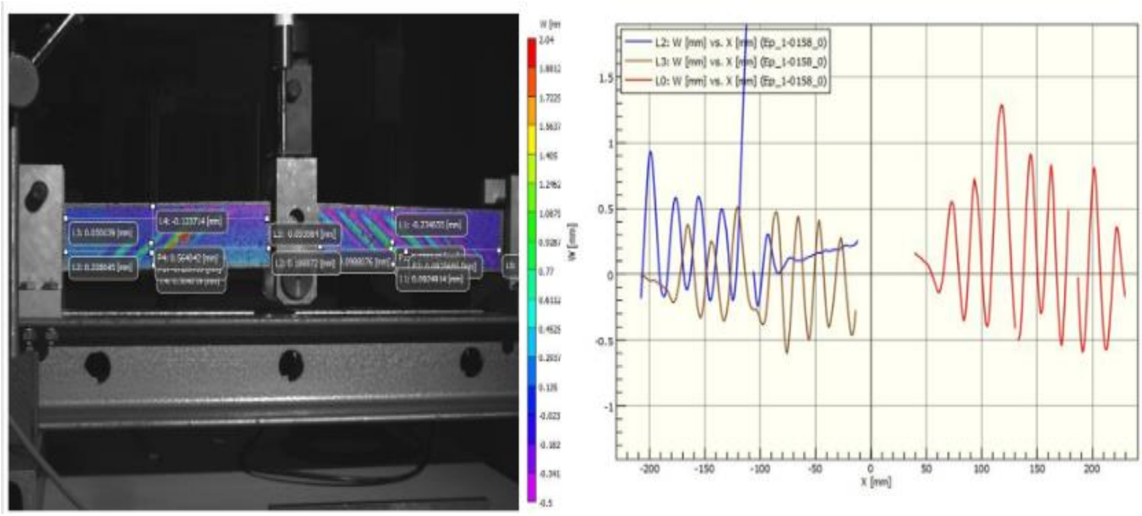

Figure 4.25: A4 out-of-plane deformation vs x-direction relationship with wave plot.

e. Specimen A5

Specimen A5 exhibited a slightly distinct behaviour in comparison to other specimens, as wrinkles developed on all sides. The load-displacement curve illustrated in Figure 4.26 elucidates the load points at which wrinkles emerged on each side. Specifically, wrinkle formation occurred on side A at 1487N, followed by side B at 1843N, side C at 2038N, and finally side D at 2769N. The influence of the initial instances of wrinkling on the overall structural stability was relatively minimal.

In addition, Figure 4.27 illustrates the temporal progression of force alongside shear strain on side A, within the region where the first wrinkle emerged. The graph also delineates a quasi-linear trajectory, persisting until the appearance of the wrinkle on side B [61]. Thereafter, a notable alteration in the slope of the shear strain parameter occurred across all four sides subsequent to the initial wrinkle formation. The shear strain right before the emergence of the first wrinkle on side A was measured at 2190με, while on side B it registered at -1960με. Notably, the shear strain on side B surged to -2103με shortly afterward. Following a modest increment in load, a wrinkle developed on side B at a shear strain of -2203με. Side C and D exhibited wrinkles at shear strain levels of 3159με and -3748με, respectively.

Furthermore, the wavelength of the wrinkles was estimated from the out-of-plane displacement in the z-direction, w, to the length along the x-direction as in Figure 4.28. This value was divided with $\sqrt{2}$ to obtain the equivalent wavelength required. The half-wavelength, a, was estimated experimentally to be $0.112t_{core}$. The first wrinkle exhibited an inward depression at Side A, indicating a localization of compressive force on the elastic core.

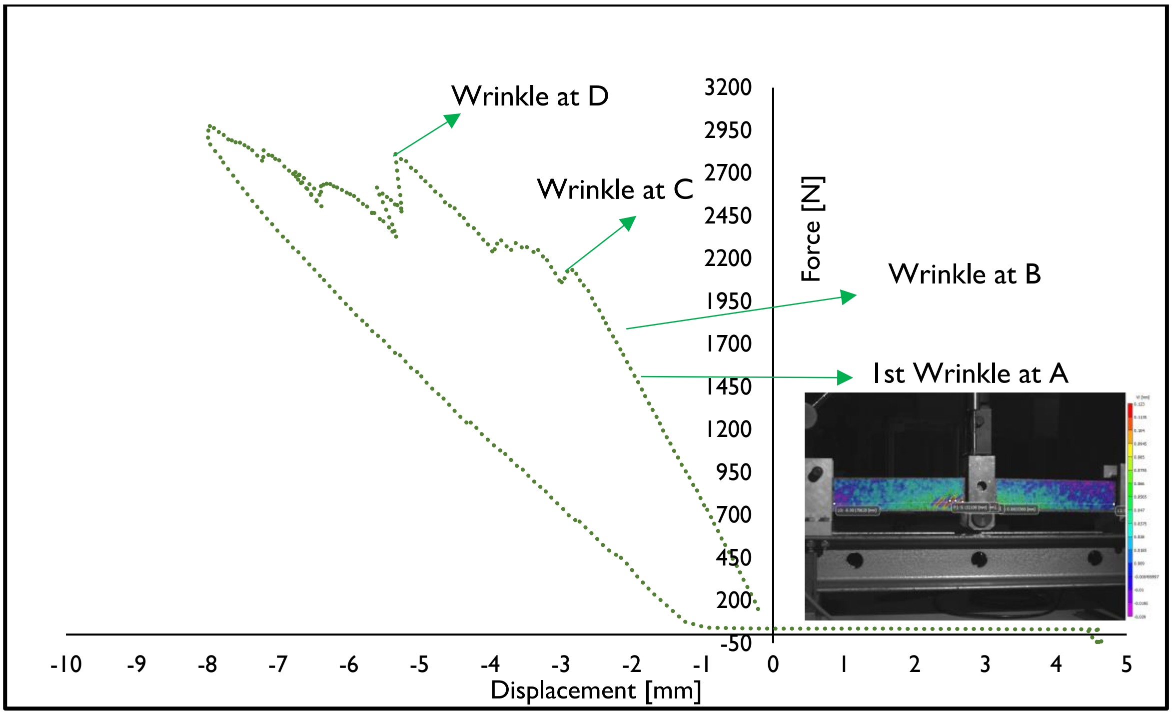

Figure 4.26: Specimen A5 load-displacement relationship plot.

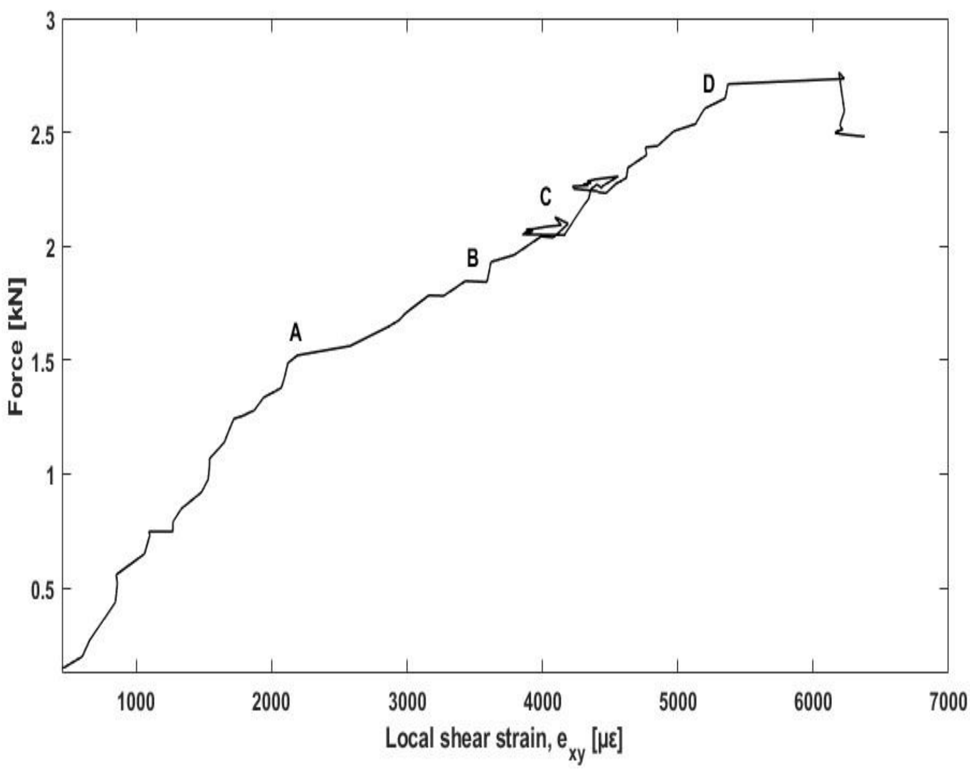

Figure 4.27: A5 side A force-local shear strain relationship curve.

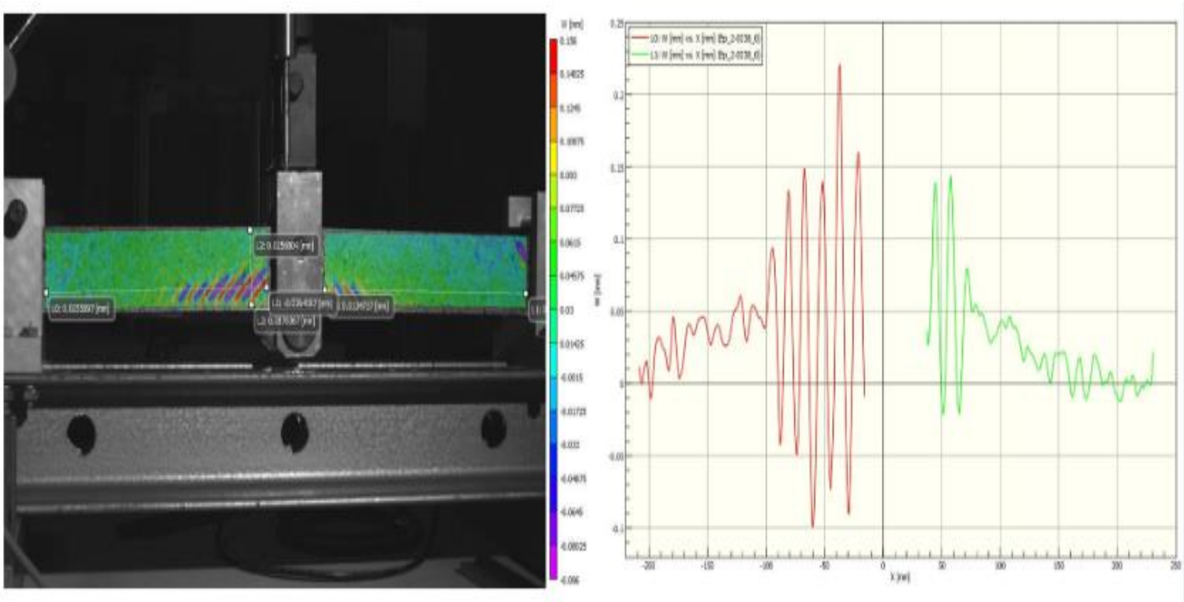

Figure 4.28: A5 out-of-plane deformation vs x-direction relationship with wave plot.

f. Specimen A6

This particular sample exhibited a wrinkling pattern akin to specimen A1, where wrinkles materialized on sides B and D concurrently. The wrinkles emerged at a load point of 3995N. Figure 4.29 visually presents the load-displacement curve, pinpointing the load at which wrinkling transpired. It can be inferred that the skin-to-core bond displayed enhanced adherence [15], which deterred debonding that could potentially lead to premature failure. Notably, no wrinkles were observed on sides A and C.

Furthermore, Figure 4.30 outlines the relationship between force and shear strain on side B, precisely at the juncture where the initial wrinkle formed [61]. The graph also delineates a quasi-linear trajectory, up until just prior to wrinkle development. The shear strain just preceding the occurrence of wrinkling at this location measured at -5688με on side B and -5489με on side D. Post-wrinkling, the strain level persisted at a plateau of -9300με on side B and surged to -20,341με on side D.

Furthermore, the wavelength of the wrinkles was estimated from the out-of-plane displacement in the z-direction, w, to the length along the x-direction as in Figure 4.31. This value was divided with $\sqrt{2}$ to obtain the equivalent wavelength required. The half-wavelength, a, was estimated experimentally to be $0.11t_{core}$. The first wrinkle exhibited an inward depression at side B, indicating a localization of compressive force on the elastic core.

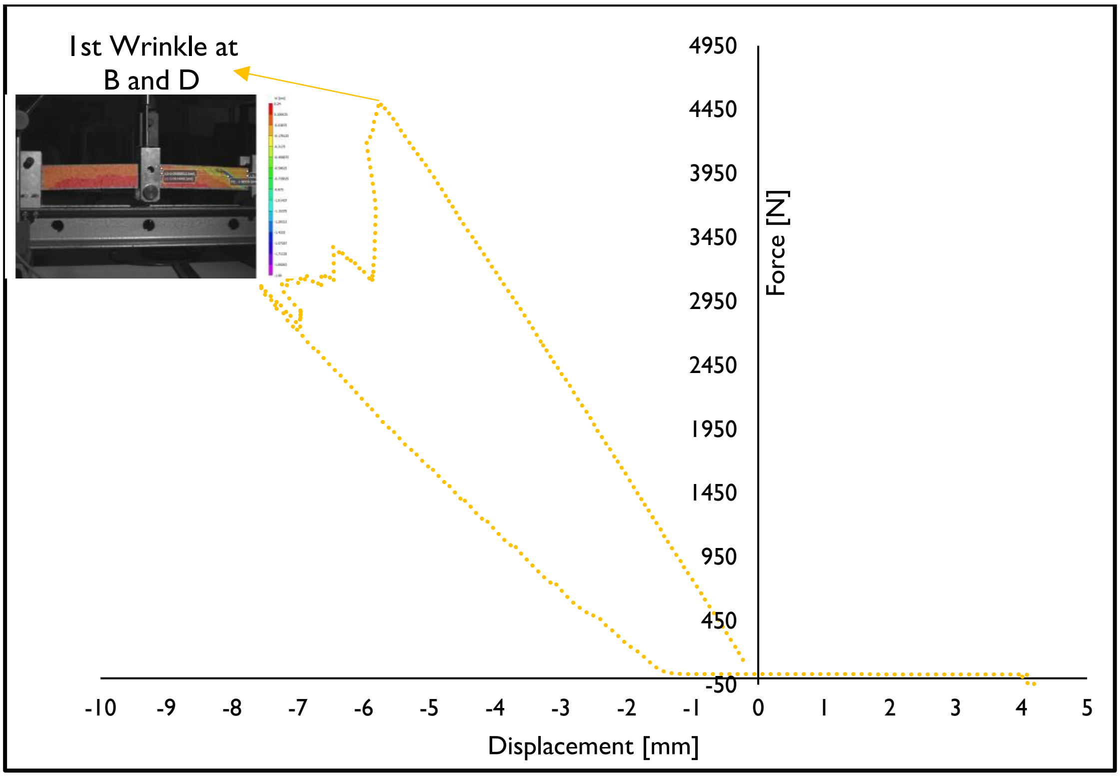

Figure 4.29: Specimen A6 load-displacement relationship plot.

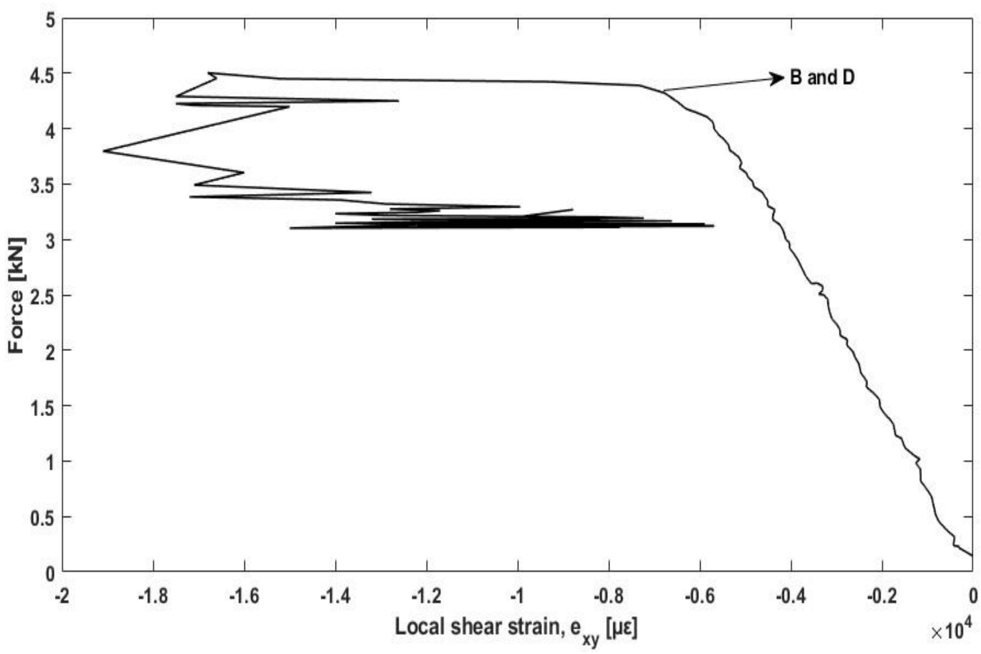

Figure 4.30: A6 side B force-local shear strain relationship curve.

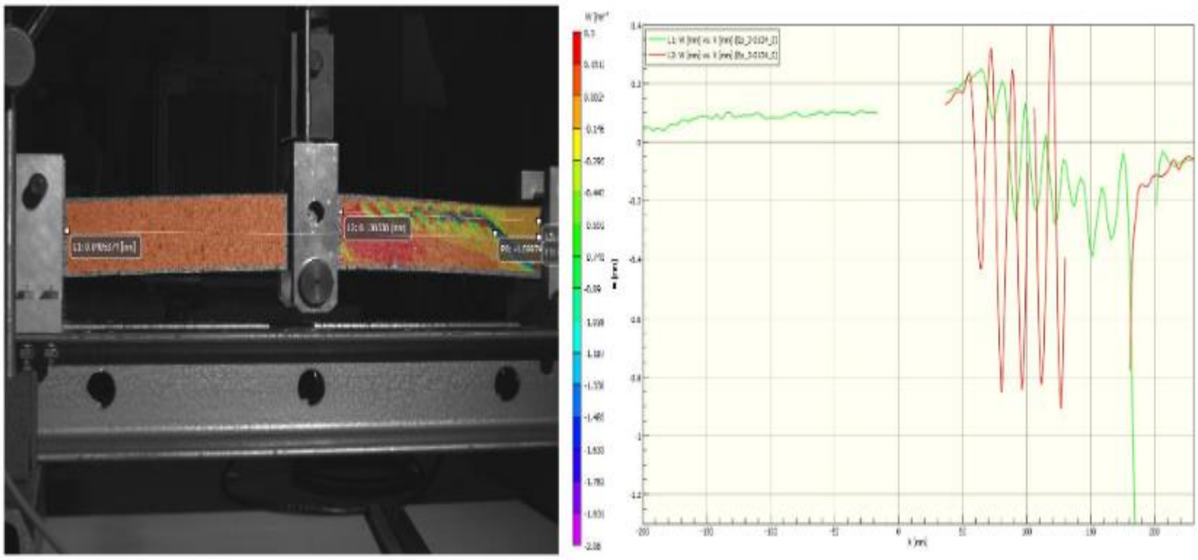

Figure 4.31: A6 out-of-plane deformation vs x-direction relationship plot.

Summarily, the results of the classical three-point bending tests and the wave evolution can be seen in the Table 4.1 below: The results of the strains in x and y directions were ignored because it is expected that their influence on the final wrinkling stress of interest is negligible.

Table 4.1: Summary of three-point bending test results and wave evolution.

Specimen ID	Shear strain before wrinkle appears (με)				1st Wrinkle side	Shear load at first wave (N)	Half wavelength, a (value*t_{core})
	Side A	Side B	Side C	Side D			
A1	N/W	-5107	N/W	N/A	B and D	3258	0.09
A2	7734	N/W	N/A	N/W	C	2654	0.18
A3	N/W	-9138	N/W	N/A	D	1438	0.11
A4	3769	-2749	N/W	N/A	B	1486	0.11
A5	2190	-2203	3159	-3748	A	1487	0.11
A6	N/W	-5688	N/W	-5489	B and D	4390	0.11

N/W – No wrinkle developed; N/A – Wrinkles appear but no DIC data; t_{core} = 50mm

The shear strain, shear loads and wave pattern in Table 4.1 provide a clear history of the test progression. The initial appearance of wrinkles in specimens A1 and A6, concurrently on sides B and D with subtle sound indications possibly pointing to core shear failure, validates the proximity of their elevated shear load at first wrinkle wave and shear strain values in the skin. Likewise, the comparatively higher skin shear strain in specimens A2 and A3 can be attributed to force redistribution following the first wrinkle formation on the side not monitored by DIC. In contrast, specimens A4 and A5, thoroughly captured by DIC, exhibit a closer trend in shear loads at first wrinkle and shear strain of the skin as shown in Table 4.1.

4.3. Mechanical performance evaluation

4.3.1. Failure loads

Figure 4.32 illustrates the combined load-displacement curve derived from the three-point bending tests for all the tested specimens. This graph also describes the specific loads at which the initiation of the first wrinkle was recognized. The specimens were all observed to exhibit elastic behaviour prior to the first wrinkling. Among the specimens, A6 demonstrated the highest stiffness prior to the first wrinkle formation. This could be attributed to the extra resin impregnation on the specimen, which was administered to address areas where certain fibres were observed to be inadequately saturated with resin post-curing. The sample underwent a secondary curing process to ensure complete polymerization. The supplementary resin strengthened the resistance and the bond between the skin and core in specimen A6, ultimately contributing to its superior performance. Specimens A4 and A5, both of which were fabricated in the same batch as A6, exhibited the emergence of the first wrinkles at closely similar force magnitude.

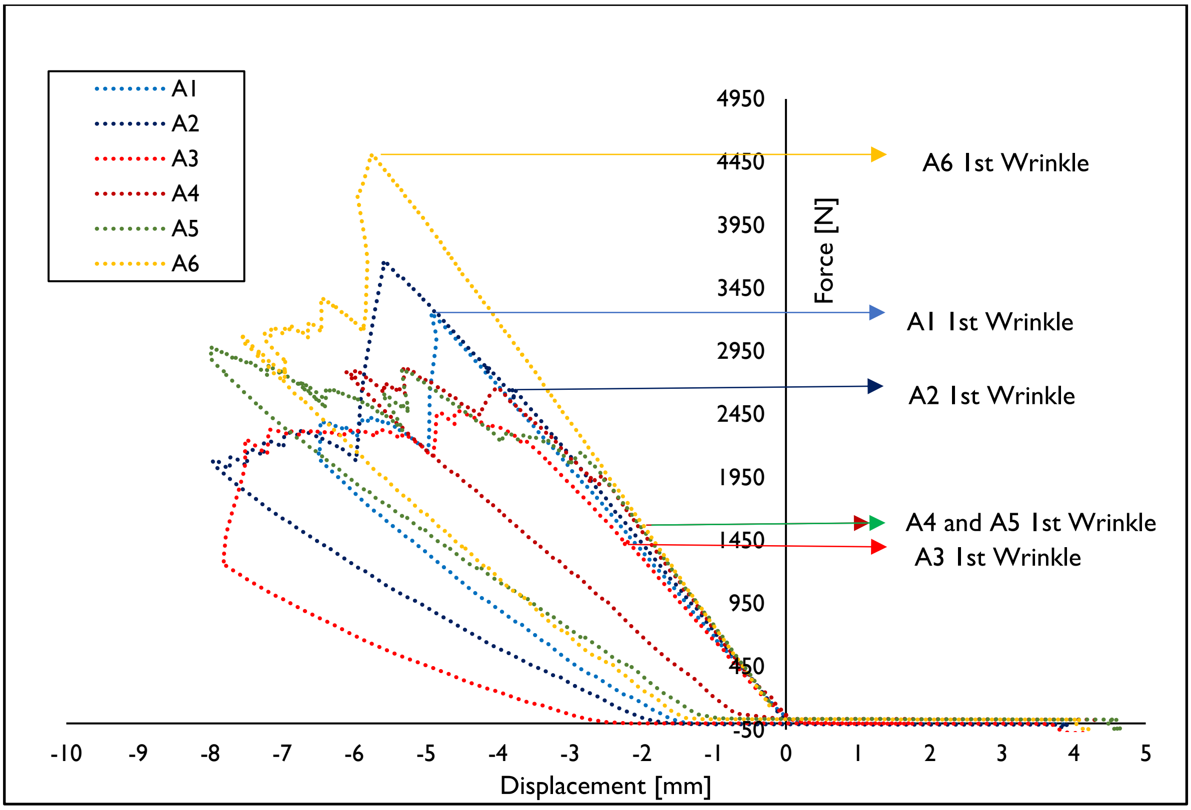

Figure 4.32: Specimen A combined load-displacement relationship curve.

Moreover, specimens A1, A2, and A3, although originating from the same production batch but fabricated by different individuals, showed variations. Specifically, A1 and A2 displayed close difference in wrinkling force compared to A3. The reduction observed in A3 wrinkling force was associated with debonding failure, as elucidated in section 4.2.2, leading to the earlier emergence of wrinkles. However, the investigation into the post-wrinkling behaviour of these specimens falls outside the purview of this study and, consequently, will be ignored here.

4.3.2. Bending stiffness of the specimens

Figure 4.33 provides insights into the bending stiffness of the six specimens. This stiffness was calculated by determining the slope of each specimen's plot in Figure 4.32 within the displacement range of 0 to -2mm. This range was chosen to avoid the non-linear effects caused by wrinkling or other unforeseen local failures. The calculated average stiffness across all specimens was 735.02N/mm.

As previously discussed, the impact of the additional resin was noticeable in specimen A6, as its stiffness was 13.8% above the calculated average. Similarly, specimens A4 and A5 maintained stiffness values 2.3% and 4.9% above the average, respectively. On the other hand, the debonding effect was evident in specimen A3, which displayed a stiffness 10.8% below the average. Specimens A1 and A2 also exhibited reduced stiffness, with values 8.7% and 1.6% below the average, respectively.

Generally, these results align closely with the findings of Kausar et. al. [7] and Castanié et al. [12] indicating that the sequence of manufacturing, variation in fibre/matrix volume, and core-skin debonding significantly impacts the structural behaviour of sandwich structures.

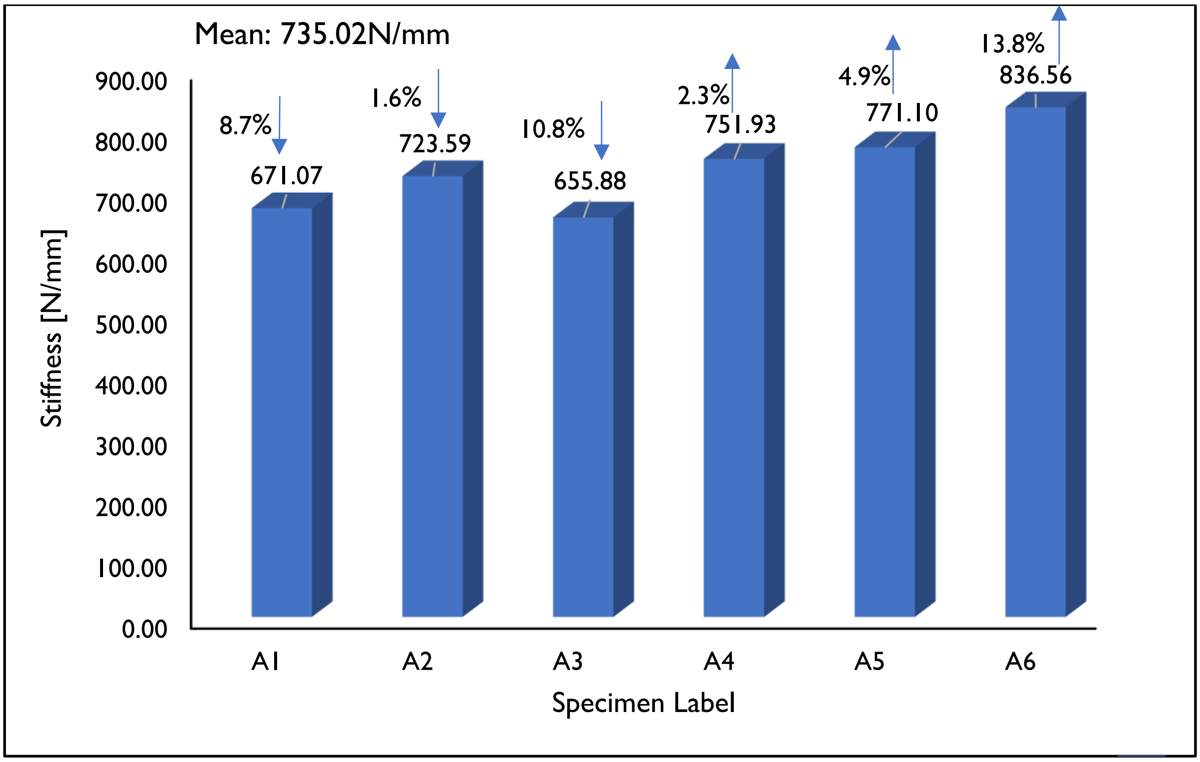

Figure 4.33: Specimen A bending stiffness comparison chat.

4.4. Wrinkling stress analysis

The wrinkling stress was estimated using three varieties of approaches as follows:

4.4.1. Approach I: Using analytical formulae

In this case the wrinkling stresses were computed using the theoretical models' equations stated in Table 2.3 while considering the mechanical properties of the materials specified in Table 3.1. Recall that the equations are primary derived for wrinkling failure due to axial compressive stress whereas shear stress is the case for this study. To conform with this situation, the properties of the fabrics were transformed at an angle of 45^o for the calculations. Given that the fabrics were installed at 45^o and the core is isotropic, hence it is convenient to adopt the mechanical properties directly without further transformation. The results are presented in Table 4.2.

Recall that the material properties for bidirectional fibre [Fabrics] and the foam core given in Table 3.1 are:

E_l = E_t = 23000MPa; G_{lt} = 2900MPa; v_{lt} = 0.098; t_s = 0.16mm.

E_c = 75MPa; G_c = 24MPa; t_{core} = 50mm

Also, from Table 2.4 Hoff and Mautner derivation for wrinkling stress are:

σ_{wr} = $0.91\sqrt[3]{E_f E_c G_c}$ without knockdown factor and;

σ_{wr} = $0.5\sqrt[3]{E_f E_c G_c}$ with knockdown factor.

Therefore, the wrinkling stress can be computed as follows:

σ_{wr} = $0.91 * \sqrt[3]{23000 * 75 * 24}$ = 314.8MPa, **without knockdown factor;**

σ_{wr} = $0.5 * \sqrt[3]{23000 * 75 * 24}$ = 173.0MPa, **with knockdown factor.**

The results of other theoretical models stated in Table 2.4 are computed and highlighted in Table 4.2 below.

Table 4.2: Wrinkling stress from analytical model formulae.

	Analytical wrinkling stress models						
	Hoff & Mautner		**Plantema**	**Allen**	**Heath**	**Gough et. al.**	**Yusuff**
	NK	**WK**					
σ_{wr} [MPa]	314.8	173.0	294.0	286.9	63.6	273.3	332.4
Half wavelength, a, (value*t_{core})	0.043		0.050	0.045	-	-	0.034

NK - No knockdown factor; WK - With knockdown factor, t_{core} = 50mm

4.4.2. Approach II: Using test force distribution analysis between the skins and the core

The approach is the estimation of shear stress in the lateral skins from the analytical calculation of forces (and stresses) distribution between skins and core. This approach involves analysis of the test setup shown in Figure 3.9 taking the mechanical properties in Table 3.1 into account. Coupled with an assumption that the shear strain, e_{xy} in the skins is the same as in the core and the shear stress is uniform and constant in the height of the specimen. It should be noted that this approach can only analyse the first wrinkling, as after, the estimation of the distribution of stress in the opposite face is no more possible. With these assumptions the following derivations were obtained;

Given that; $T_Y = \frac{F}{2}$; where F is the wrinkling failure load. **Equation 4.1**

Distribution of shear force between the foam core and the skins

$$T_Y = 2.S_{skin}.\tau_{skin} + S_{core}.\tau_{core}$$ **Equation 4.2**

where S_{skin}, τ_{skin}, S_{core}, and τ_{core} are the skin surface area and shear stress, and the core surface area and shear stress respectively. The multiplied 2 denotes the two skins' shear force.

Note that the shear stresses in the skin and the core can be expressed as;

$$\tau_{skin} = 2.G_{skin}.\varepsilon_{xy}$$
$$\tau_{core} = 2.G_{core}.\varepsilon_{xy}$$ **Equation 4.3**

Therefore;

$$\varepsilon_{xy} = \frac{F}{4[2.S_{skin}.G_{skin} + S_{core}.G_{core}]}$$ **Equation 4.4**

G_{skin} = G_{12} = shear modulus of the skin laminate derived from transformed stiffness matrix.

Where, G_{skin} = 10474 MPa; S_{skin} = $t_{skin} * h_{skin}$; and S_{core} = $t_{core} * h_{core}$

With these parameters the wrinkling stresses are estimated for each of the specimens as shown in Table 4.3. These stresses are equivalent to the wrinkling stress at the first wrinkle for all the specimens.

The resultant shear forces on the skins and the core at the onset of the first wrinkle are presented in Table 4.3, as stated in the Equation 4.2. These results reveal that the two skins can withstand more than twice the shear force experienced by the core. Consequently, based on this analysis, it would be hypothetically inadequate to disregard the core's contribution to shear force resistance. Moreover, it is important to acknowledge the doubt in the reliability of this approach, which is rooted in the assumption that the shear strain in the core and skin are equal. This assumption may not hold true for all scenarios, as it could be influenced by the specific ratio of skin and core stiffnesses.

Table 4.3: Wrinkling stress using approximate test analysis.

Specimen ID	Shear force at first wrinkle, F [N]	Shear strain, ε_{xy} [με]	Skin shear stress, τ_{skin} [MPa]	Core shear stress, τ_{core} [MPa]	Skins shear force [N]	Core shear force [N]
A1	3258	3579	74.97	0.17	1199.53	429.47
A2	2654	2915	61.07	0.14	977.15	349.85
A3	1438	1580	33.09	0.08	529.44	189.56
A4	1486	1632	34.19	0.08	547.00	195.84
A5	1487	1634	34.23	0.08	547.64	196.07
A6	4390	4822	101.01	0.23	1616.13	578.62

4.4.3. Approach III: Using DIC strain results

This methodology encompasses the computation of the wrinkling stress by utilizing the measured strain data from the tests and considering the properties of the skin to determine the "experimental" stress. The Digital Image Correlation (DIC) technique played a pivotal role in this experiment. It was instrumental in providing precise strain parameters at any instance, which, when combined with the precise material mechanical properties, simplified the calculation of the stress of interest.

The shear strain, ε_{xy} just before the first wrinkle at the position of the first wrinkling were considered. The shear strains after the occurrence of the first wrinkle are inconsistent due to the wrinkle, hence they were neglected. The strains in x and y directions, ε_{xx} and ε_{yy} were also neglected since they vary across the height of the specimens and their contributions to the wrinkling stress in study is apparently insignificant.

Case A

In this case, the stress constitutive Equation 4.5 was implemented by calculating the plane stress stiffness matrix $[Q]$ using the mechanical properties in Table 3.1 on MATLAB in the plane coordinates 1 and 2 as shown in Figure 4.34. Meanwhile, the shear strain parameters, $[\varepsilon_{xyz}]$ were extracted from the VIC 3D software associated with the DIC technique just before the first wrinkle developed as in Table 4.1. For the plane strain parameters, ε_{123}, it is logical to assume the shear strain ε_{xy} measured directly from the DIC corresponds to the strain in direction 1, ε_{11}, which is responsible for the compressive stress leading to wrinkling formation. Similarly, the strain in direction 2, ε_{22}, can be resolved as a tensile strain and is equivalent to the negative of the shear strain, ε_{xy} directly measure from the DIC. The shear strain parameter, ε_{12} in 1-2 direction which can be taken as either ε_{xx} or ε_{yy} is neglected because it has no effect on the stress being considered. The equivalent stresses were computed and presented in Table 4.4.

Plane stress constitutive equation:

$$[\sigma_{123}] = [Q][\varepsilon_{123}]$$ **Equation 4.5**

Plane stress stiffness matrix in directions 1 and 2; $[Q]$ =

$$1.0e{+}04 * \begin{bmatrix} 2.3223 & 0.2276 & 0.0000 \\ 0.2276 & 2.3223 & 0.0000 \\ 0.0000 & 0.0000 & 0.2900 \end{bmatrix}$$

Plane strain in directions 1 and 2; $[\varepsilon_{123}]$ =

$$\begin{bmatrix} \varepsilon_{11} \\ \varepsilon_{22} \\ \varepsilon_{12} \end{bmatrix} = \begin{bmatrix} \varepsilon_{xy} \\ -\varepsilon_{xy} \\ 0 \end{bmatrix}$$

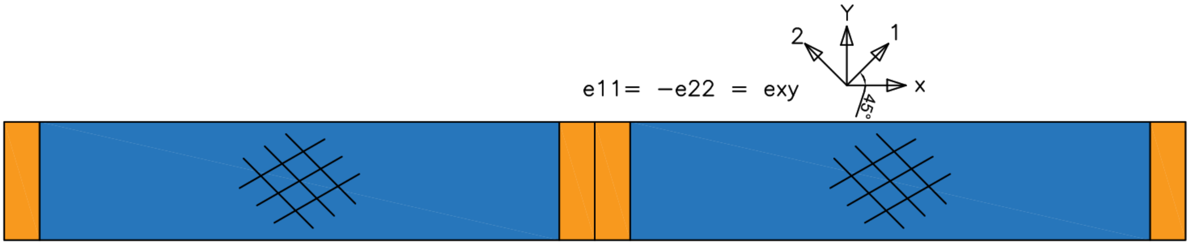

Figure 4.34: Typical specimen coordinates system representation.

Recall that shear skin laminate stacking sequence is symmetric [±45] about its midplane, which makes the $Q_{16} = Q_{26} = Q_{61} = Q_{62} = 0$. Hence, the wrinkling stress can be obtained by:

$$\boldsymbol{\sigma_{11} = \sigma_{22} = Q_{11}.\varepsilon_{11} + Q_{12}.\varepsilon_{22}}$$ **Equation 4.6**

The wrinkling stress on each face based on the shear strain results in Table 4.1 were computed. The wrinkling stress based on Equation 4.6 for specimens which the DIC captured the first wrinkle are bolden for emphasis.

Table 4.4: Wrinkling stress using DIC strain parameters case A.

Specimen ID	Wrinkling stress at the first wrinkle (MPa)				1st Wrinkle side
	Side A	Side B	Side C	Side D	
A1	N/W	106.97*	N/W	N/A	B and D
A2	162.01*	N/W	N/A	N/W	C
A3	N/W	191.41*	N/W	N/A	D
A4	78.95	**57.58**	N/W	N/A	B
A5	**45.87**	46.15	66.17	78.51	A
A6	N/W	**119.14**	N/W	114.98	B and D

* Not first wrinkle stress because first wrinkle developed on the face without DIC camera; N/W – No wrinkle developed; N/A – Wrinkles appear but no DIC data.

Case B

For this case it is proposed that the stiffness of the skin is directly its elastic modulus E_l in Table 3.1. On the basis that the shear strain acts at 45° which corresponds to the skin angle of rotation during installation. The wrinkling stress on each face based on the shear strain results in Table 4.1 were computed. The wrinkling stress for specimens which the DIC captured the first wrinkle are bolden for emphasis.

Table 4.5: Wrinkling stress using DIC strain parameters case B.

Specimen ID	Wrinkling stress at the first wrinkle (MPa)				1st Wrinkle side
	Side A	Side B	Side C	Side D	
A1	N/W	117.46*	N/W	N/A	B and D
A2	177.88*	N/W	N/A	N/W	C
A3	N/W	210.17*	N/W	N/A	D
A4	86.69	**63.23**	N/W	N/A	B
A5	**50.37**	50.67	72.66	86.20	A
A6	N/W	**130.82**	N/W	126.25	B and D

* Not first wrinkle stress because first wrinkle developed on the face without DIC camera; N/W – No wrinkle developed; N/A – Wrinkles appear but no DIC data.

Two cases, Case A and case B were considered for this analysis due to their different perspectives on the skin stiffness in the shear stress direction. In Case A, the skin directions were resolved to be transformed from at x and y directions to 1 and 2 directions, respectively, using the plane stress constitutive approach. The stress was determined based on the stiffness matrix parameters in the fabric direction. On the other hand, Case B assumed the stiffness to be the elastic modulus since the fabric was installed at 45^{o}, which aligns with the direction of the shear force. Comparing the stress results for the first wrinkle in Case A and Case B, they appear to be close but different from the results of the theoretical models presented in Table 4.2.

4.4.4. General discussion

The results derived from the analytical models consistently indicate significantly higher estimations, often exceeding the experimental results up to a multiple of 5. This disparity in values can be attributed to a range of factors, including variations in boundary conditions, assumptions made during derivations, manufacturing imperfections, and other sources of uncertainty. These results emphasize the nonconservative nature of the models and highlight the substantial discrepancies reported in various scientific literature [6], [34], [56].

THIS PAGE WAS INTENTIONALLY LEFT BLANK

5. Chapter 5. Conclusions and Further Development

5.1.1. Conclusions

The methodology employed in this research serves as a valuable benchmark for future investigations into wrinkling in sandwich structures. It was observed that the analytical models consistently yielded significantly higher estimations of wrinkling stress compared to the experimental results at first wrinkle, often up to a factor of 5. This corroborates the consensus in existing literature that analytical models tend to be nonconservative. Also, the wave length was experimentally observed to be relatively $0.1t_{core}$ irrespective of the force that initiated the wrinkle wave.

Furthermore, this study emphasizes the susceptibility of sandwich manufacturing techniques to surface imperfections, which act as vulnerable points for the development of wrinkling in sandwich structures. The research also demonstrates based on assumption that the proportion of resin has an influence on both the global structural stiffness and the wrinkling stress in sandwich structures.

5.1.2. Further development

a. The large deviation observed between the experimental findings and the analytical models could be validated by developing an appropriate Finite Element (FE) model that closely simulates the experimental setup. Unfortunately, the time constraints of this study prevented the exploration of this concept.
b. An influential factor contributing to the observed disparity is the manufacturing process. Critical parameters like resin thickness and distribution, resin absorption by the foam cells, and fibre waviness are challenging to control during manufacturing. Therefore, future research endeavours could explore alternative sandwich construction techniques that mitigate the impact of these parameters.
c. To address economic considerations, many industries employ ply-drops in their parts to reduce costs and overall structural weight. The inclusion of ply-drops on the skin naturally introduces surface imperfections that can trigger wrinkling. Consequently, it would be a pertinent area of investigation to conduct tests on specimens featuring ply-drops in the skin.

REFERENCES

[1] F. C. Campbell, *Manufacturing Technology for Aerospace Structural Materials*. London, UK: Elsevier Ltd., 2006.

[2] J. P. Nunes and J. F. Silva, “Sandwiched composites in aerospace engineering,” *Advanced Composite Materials for Aerospace Engineering*, pp. 129–174, Jan. 2016, doi: 10.1016/B978-0-08-100037-3.00005-5.

[3] L. Fagerberg and D. Zenkert, “Imperfection-induced wrinkling material failure in sandwich panels,” *Journal of Sandwich Structures and Materials*, vol. 7, no. 3, pp. 195–219, May 2005, doi: 10.1177/1099636205048526.

[4] D. Zenkert, *An Introduction to Sandwich Structures*. 1995.

[5] M. Ginot, M. D’Ottavio, O. Polit, C. Bouvet, and B. Castanié, “Benchmark of wrinkling formulae and methods for pre-sizing of aircraft lightweight sandwich structures,” *Compos Struct*, vol. 273, Oct. 2021, doi: 10.1016/j.compstruct.2021.114387.

[6] M. Ginot, C. Bouvet, B. Castanié, J. Serra, and N. Mahuet, “Local buckling on large sandwich panels used in light aviation: Experimental setup and failure scenarios,” *Compos Struct*, vol. 304, Jan. 2023, doi: 10.1016/j.compstruct.2022.116439.

[7] A. Kausar, I. Ahmad, S. A. Rakha, M. H. Eisa, and A. Diallo, “State-Of-The-Art of Sandwich Composite Structures: Manufacturing—to—High Performance Applications,” *Journal of Composites Science*, vol. 7, no. 3. MDPI, Mar. 01, 2023. doi: 10.3390/jcs7030102.

[8] R. P. Ley, W. Lin, and U. Mbanefo, “Facesheet Wrinkling in Sandwich Structures,” 1999. [Online]. Available: www.sti.nasa.gov

[9] D. Zenkert, *The Handbook of Sandwich Construction*. 1997.

[10] N. J. Hoff and S. E. Mautner, “The Buckling of Sandwich-Type Panels,” *Journal of the Aeronautical Sciences*, vol. 12, no. 3, pp. 285–297, Jul. 1945, doi: 10.2514/8.11246.

[11] A. Shipsha, “Failure of Sandwich Structures with Sub-Interface Damage,” Academic dissertation, Royal Institute of Technology, Sweden, 2001.

[12] B. Castanié, C. Bouvet, and M. Ginot, “Review of composite sandwich structure in aeronautic applications,” *Composites Part C: Open Access*, vol. 1, Aug. 2020, doi: 10.1016/j.jcomc.2020.100004.

[13] J. Sena-Cruz, “FRP++4: Design of Structures with FRP Materials Lesson 5: Sandwich Structures-Part I,” Guimaraes, Jan. 2023.

[14] A. Krzyzak, M. Mazur, M. Gajewski, K. Drozd, A. Komorek, and P. Przybyłek, "Sandwich Structured Composites for Aeronautics: Methods of Manufacturing Affecting Some Mechanical Properties," *International Journal of Aerospace Engineering*, vol. 2016, 2016, doi: 10.1155/2016/7816912.

[15] L. A. Carlsson and G. A. Kardomateas, *Structural and Failure Mechanics of Sandwich Composites*, vol. 121. in Solid Mechanics and Its Applications, vol. 121. Dordrecht: Springer Netherlands, 2011. doi: 10.1007/978-1-4020-3225-7.

[16] E. Gdoutos and I. Daniel, "Failure modes of composite sandwich beams," 2008.

[17] I. M. Daniel, E. E. Gdoutos, K. A. Wang, and J. L. Abot, "Failure modes of composite sandwich beams," *International Journal of Damage Mechanics*, vol. 11, no. 4, pp. 309–334, 2002, doi: 10.1106/105678902027247.

[18] E. E. Gdoutos, I. M. Daniel, and K.-A. Wang, "Compression facing wrinkling of composite sandwich structures," *Mechanics of Materials*, vol. 35, pp. 511–522, 2003.

[19] C. Kassapoglou, *Design and Analysis of Composite Structures: with Applications to Aerospace Structures*, 1st ed. John Wiley and Sons Ltd., 2010.

[20] G. Belingardi, M. P. Cavatorta, and R. Duella, "Material characterization of a composite–foam sandwich for the front structure of a high-speed train," *Compos Struct*, vol. 61, no. 1–2, pp. 13–25, Jul. 2003, doi: 10.1016/S0263-8223(03)00028-X.

[21] C. Aparecida Diniz, D. Brighenti Bortoluzzi, J. Luiz Junho Pereira, S. Simões da Cunha Junior, and G. Ferreira Gomes, "On the influence of manufacturing parameters on buckling and modal properties of sandwich composite structures," *Structures*, vol. 46, pp. 664–680, Dec. 2022, doi: 10.1016/J.ISTRUC.2022.10.059.

[22] W. Ji and A. M. Waas, "2D elastic analysis of the sandwich panel buckling problem: Benchmark solutions and accurate finite element formulations," *Zeitschrift fur Angewandte Mathematik und Physik*, vol. 61, no. 5, pp. 897–917, 2010, doi: 10.1007/s00033-009-0041-z.

[23] V. Birman and J. Lee, "Wrinkling in sandwich panels with bi-modular core," *ZAMM Zeitschrift fur Angewandte Mathematik und Mechanik*, vol. 100, no. 1. Wiley-VCH Verlag, Jan. 01, 2020. doi: 10.1002/zamm.201900137.

[24] G. S. Gough, C. F. Elam, G. H. Tipper, and N. A. De Bruyne, "The Stabilisation of a Thin Sheet by a Continuous Supporting Medium," *The Journal of the Royal Aeronautical Society*, vol. 44, no. 349, pp. 12–43, Jan. 1940, doi: 10.1017/s036839310010495x.

[25] W. Vocke, “F. J. Plantema, Sandwich Construction. XX + 246 S. m. Fig. New York/London/Sydney 1966. John Wiley & Sons, Inc. Preis geb. 115 s,” *ZAMM - Zeitschrift für Angewandte Mathematik und Mechanik*, vol. 47, no. 2, pp. 138–138, 1967, doi: 10.1002/zamm.19670470212.

[26] H. G. Allen, “Wrinkling and Other Forms of Local Instability,” in *Analysis and Design of Structural Sandwich Panels*, Elsevier, 1969, pp. 156–189. doi: 10.1016/B978-0-08-012870-2.50012-2.

[27] S. Yusuff, “Theory of Wrinkling in Sandwich Construction,” *The Journal of the Royal Aeronautical Society*, vol. 59, no. 529, pp. 30–36, Jan. 1955, doi: 10.1017/s0368393100131761.

[28] V. Birman and C. W. Bert, “Wrinkling of composite-facing sandwich panels under biaxial loading,” *Journal of Sandwich Structures and Materials*, vol. 6, no. 3, pp. 217–237, May 2004, doi: 10.1177/1099636204033643.

[29] W. Su and S. Liu, “A couple-stress model to predict the wrinkling stress of sandwich panels with foam cores,” *Compos Struct*, vol. 268, Jul. 2021, doi: 10.1016/j.compstruct.2021.113978.

[30] L. Léotoing, S. Drapier, and A. Vautrin, “First applications of a novel unified model for global and local buckling of sandwich columns,” *European Journal of Mechanics - A/Solids*, vol. 21, no. 4, pp. 683–701, Jan. 2002, doi: 10.1016/S0997-7538(02)01229-9.

[31] K. Niu and R. Talreja, “Modeling of Wrinkling in Sandwich Panels Under Compression,” *J Eng Mech*, vol. 125, no. 8, pp. 875–883, Aug. 1999.

[32] M.-A. Douville and P. Le Grognec, “Exact analytical solutions for the local and global buckling of sandwich beam-columns under various loadings,” *Int J Solids Struct*, vol. 50, no. 16–17, pp. 2597–2609, Aug. 2013, doi: 10.1016/j.ijsolstr.2013.04.013.

[33] M. A. Stiftinger and F. G. Rammerstorfer, “Face Layer Wrinkling in Sandwich Shells - Theoretical and Experimental Investigations,” *Thin-Walled Structures*, vol. 29, no. 4, pp. 113–127, 1997.

[34] H. Tuwair, J. Volz, M. A. ElGawady, K. Chandrashekhara, and V. Birman, “Modeling and Analysis of GFRP Bridge Deck Panels Filled with Polyurethane Foam,” *Journal of Bridge Engineering*, vol. 21, no. 5, May 2016, doi: 10.1061/(asce)be.1943-5592.0000849.

[35] B. Castanié, Barrau J. J., Jaouen J. P., and S. Rivallant, “Combined Shear/Compression Structural Testing of Asymmetric Sandwich Structures,” *Exp Mech*, vol. 44, no. 5, pp. 461–472, Oct. 2004, doi: 10.1177/0014485104047607.

[36] F. Neveu, B. Castanié, and P. Olivier, "The GAP methodology: A new way to design composite structures," *Mater Des*, vol. 172, p. 107755, Jun. 2019, doi: 10.1016/j.matdes.2019.107755.

[37] M. Wang, X. Yu, J. Zhang, and Q. Qin, "Three-point bending of physically asymmetric metal sandwich beams with aluminum foam core: Failure behavior and optimal design," *Compos Struct*, vol. 280, p. 114873, Jan. 2022, doi: 10.1016/j.compstruct.2021.114873.

[38] W. Zhang, J. Li, Z. Wang, K. Li, C. Bai, and Q. Qin, "The influence of asymmetric faces on low-velocity impact failure of CFRP/aluminum foam composite sandwich beams," *Eng Struct*, vol. 292, p. 116574, Oct. 2023, doi: 10.1016/j.engstruct.2023.116574.

[39] B. Castanié, J. J. Barrau, and J. P. Jaouen, "Theoretical and experimental analysis of asymmetric sandwich structures," *Compos Struct*, vol. 55, no. 3, pp. 295–306, Feb. 2002, doi: 10.1016/S0263-8223(01)00156-8.

[40] B. Li, Y. P. Cao, X. Q. Feng, and H. Gao, "Mechanics of morphological instabilities and surface wrinkling in soft materials: A review," *Soft Matter*, vol. 8, no. 21. pp. 5728–5745, Jun. 07, 2012. doi: 10.1039/c2sm00011c.

[41] "Properties of ROHACELL WF," *Evonik Rohm GmbH*. https://pronatindustries.com/wp-content/uploads/2014/12/ROHACELL-WF-Product-Information-datasheet.pdf (accessed Aug. 05, 2023).

[42] S. K. Mazumdar, *Composites manufacturing: materials, product, and process engineering*. CRC Press, 2002.

[43] J. Sena-Cruz and J. Renart, "FRP++4: Design of Structures with FRP Materials Lesson 7: Adhesive joints and connections on composite structures Materials," Guimaraes and Girona, Jan. 2023.

[44] J. Galos, R. Das, M. P. Sutcliffe, and A. P. Mouritz, "Review of balsa core sandwich composite structures," *Mater Des*, vol. 221, p. 111013, Sep. 2022, doi: 10.1016/j.matdes.2022.111013.

[45] B. Castanié, "FRP++1: Composite Materials in the Industry Lesson 3: Laminate and sandwiches," Toulouse, Oct. 2022.

[46] A. Memarzadeh, B. Safaei, A. Tabak, S. Sahmani, and C. Kizilors, "Advancements in additive manufacturing of polymer matrix composites: A systematic review of techniques and properties," *Mater Today Commun*, vol. 36, p. 106449, Aug. 2023, doi: 10.1016/j.mtcomm.2023.106449.

[47] A. Yousefi Kanani and A. Kennedy, "Experimental and numerical analysis of additively manufactured foamed sandwich beams," *Compos Struct*, vol. 312, p. 116866, May 2023, doi: 10.1016/j.compstruct.2023.116866.

[48] K. Makarian, M. Taghvaei, J. Tu, N. J. Alvarez, and G. R. Palmese, "Design, manufacturing, and elastic analysis of digital light processing 3D printed fiber reinforced sandwich beams with thermosetting polymer matrix," *Compos Struct*, vol. 318, p. 117108, Aug. 2023, doi: 10.1016/j.compstruct.2023.117108.

[49] Y. Aminanda, B. Castanié, J. J. Barrau, and P. Thevenet, "Experimental analysis and modeling of the crushing of honeycomb cores," in *Applied Composite Materials*, May 2005, pp. 213–227. doi: 10.1007/s10443-005-1125-3.

[50] C. Kassapoglou, S. C. Fantle, and J. C. Chou, "Wrinkling of composite sandwich structures under compression," *Journal of Composites Technology and Research*, vol. 17, no. 4, pp. 308–316, 1995, doi: 10.1520/ctr10451j.

[51] K. S. Sonu Shravan, "Buckling and Wrinkling Analysis of Composite Sandwich Plates using Finite Element Methods," Master of Science in Aerospace Engineering, California State University, 2018.

[52] W. Ji and A. M. Waas, "Global and Local Buckling of a Sandwich Beam," *J Eng Mech*, vol. Vol. 133, no. No. 2, pp. 230–237, Feb. 2007, doi: 10.1061/ASCE0733-93992007133:2230.

[53] W. Ji and A. M. Waas, "Wrinkling and Edge Buckling in Orthotropic Sandwich Beams," *J Eng Mech*, vol. Vol. 134, no. No. 6, pp. 455–461, Jun. 2008, doi: 10.1061/ASCE0733-93992008134:6455.

[54] R. Vescovini, M. D'Ottavio, L. Dozio, and O. Polit, "Buckling and wrinkling of anisotropic sandwich plates," *Int J Eng Sci*, vol. 130, pp. 136–156, Sep. 2018, doi: 10.1016/j.ijengsci.2018.05.010.

[55] E. Carrera and S. Brischetto, "A Survey with Numerical Assessment of Classical and Refined Theories for the Analysis of Sandwich Plates," *Appl Mech Rev*, vol. 62, no. 1, Jan. 2009, doi: 10.1115/1.3013824.

[56] B. K. Hadi and F. L. Matthews, "Development of Benson-Mayers theory on the wrinkling of anisotropic sandwich panels," *Compos Struct*, vol. 29, pp. 425–434, 2000, [Online]. Available: www.elsevier.com/locate/compstruct

[57] D. Yakine, L. B. Jonas, and M. Mélanie, "Development of a new wrinkling test for aeronautic sandwich structures," INSA Toulouse, 2022.

[58] Correlated Solutions, "VIC-3D Software Manual Version 9.4."

[59] M. Bowkett and K. Thanapalan, "Comparative analysis of failure detection methods of composites materials' systems," *Systems Science and Control Engineering*, vol. 5, no. 1. Taylor and Francis Ltd., pp. 168–177, Jan. 01, 2017. doi: 10.1080/21642583.2017.1311240.

[60] R. Bigger *et al.*, "A Good Practices Guide for Digital Image Correlation," Oct. 2018. doi: 10.32720/idics/gpg.ed1.

[61] I. M. Daniel, E. E. Gdoutos, I. M. Daniel, R. R. Mccormick, and E. E. Gdoutos, "Failure Modes of Composite Sandwich Beams," *Springer Science and Business Media B.V.*, pp. 197–227, 2009.